

2020-09

Protracted Shearing at Midcrustal Conditions During LargeScale Thrusting in the Scandinavian Caledonides

Giuntoli, F

<http://hdl.handle.net/10026.1/16206>

10.1029/2020tc006267

Tectonics

American Geophysical Union (AGU)

All content in PEARL is protected by copyright law. Author manuscripts are made available in accordance with publisher policies. Please cite only the published version using the details provided on the item record or document. In the absence of an open licence (e.g. Creative Commons), permissions for further reuse of content should be sought from the publisher or author.

Protracted shearing at mid-crustal conditions during large-scale thrusting in the Scandinavian Caledonides

Francesco Giuntoli^{1,2}, Luca Menegon^{3,1}, Clare J. Warren⁴, James Darling⁵, Mark Anderson¹

¹School of Geography, Earth and Environmental Sciences, Plymouth University, Plymouth PL4 8AA, UK

²Department of Biological, Geological and Environmental Sciences, Università degli Studi di Bologna, Bologna, Italy

³The Njord Centre, Department of Geoscience, University of Oslo, P.O. Box 1048 Blindern, Norway

⁴Department of Environment, Earth and Ecosystems, Centre for Earth, Planetary, Space and Astronomical Research (CEPSAR), The Open University, Walton Hall, Milton Keynes, MK7 6AA, UK

⁵School of the Environment, Geography and Geosciences, University of Portsmouth, Portsmouth PO1 3QL, UK

Corresponding author: Francesco Giuntoli (francesco.giuntoli@gmail.com)

Key Points:

- In the Lower Seve Nappe 1 km thick mylonitic foliation formed at amphibolite facies conditions between ~460 to ~417 Ma
- Toward the base of the nappe the foliation is overprinted by a brittle-to-ductile fabric of greenschist facies conditions (~417 to 400 Ma)
- These fabrics formed due to protracted and long-lasting shearing during the exhumation and assembly of the Seve Nappe Complex

Abstract

During continental collision, large tracts of crust are mobilised along major shear zones. The metamorphic conditions at which these zones operate, the duration of thrusting, and the deformation processes that facilitated hundreds of km of tectonic transport are still unclear. In the Scandinavian Caledonides, the Lower Seve Nappe displays a main mylonitic foliation with thickness of ~1 km. This foliation is overprinted by a brittle-to-ductile deformation pattern localized in C and C'-type shear bands proximal to the tectonic contact with the underlying Särvi Nappe. Thermobarometry of amphibolites and micaschists suggest a first high-pressure stage at 400-500°C and 1-1.3 GPa recorded in mineral relics. The main mylonitic foliation developed under epidote amphibolite facies conditions along the retrograde path from 600°C and 1 GPa to 500°C and 0.5 GPa. Age dating of synkinematic titanite grains in the amphibolites indicates that this mylonitic fabric formed at around 417 ± 9 Ma, but older ages spanning 460-430 Ma could represent earlier stages of mylonitization. The shear bands developed at lower metamorphic conditions of 300-400°C and ~0.3 GPa. In the micaschists, the recrystallized grain size of quartz decreases towards the shear bands. Monomineralic quartz layers are eventually dismembered to form polyphase aggregates deforming by dominant grain size sensitive creep accompanied by slip in muscovite and chlorite. Plagioclase zoning truncations suggest that the shear bands originated by fracturing followed by ductile deformation. The results suggest protracted and long-lasting shearing under amphibolite to greenschist facies conditions during the juxtaposition, stacking and exhumation of the Lower Seve Nappe.

Keywords

Caledonides, deformation mechanisms, electron backscatter diffraction, petrochronology, U–Pb dating, thrusting.

1. Introduction

Thrusts in mountain belts localize much of the tectonic transport associated with crustal shortening during mountain building. They may be responsible for the juxtaposition of units characterized by remarkably contrasting tectonometamorphic histories (Bender et al., 2018; Gee, 1975; Giuntoli & Engi, 2016; Jolivet et al., 1998; Searle et al., 2008; Zwart, 1975). As they frequently form via several stages of deformation, shear zones often preserve multiple generations of overprinting

mineral fabrics and relics, reflecting the evolution from higher to lower metamorphic grades (e.g. Papapavlou et al., 2018). Moreover, some fabrics display evidence of early stages of brittle deformation that has been later overprinted by crystal plastic deformation (e.g. Austrheim, 1987; Fusseis et al., 2006; Giuntoli, Menegon, et al., 2018; Mancktelow & Pennacchioni, 2005). In many cases cycles of brittle and ductile deformation appear to alternate due to the effect of different parameters, such as strain rate and stress variations, pore fluid pressure, mineral reactions and associated weakening or hardening of the rock (Brander et al., 2012; Bukovská et al., 2016; Gerald & Stünitz, 1993; Giuntoli et al., 2020; Kjøl et al., 2015; Menegon et al., 2013; Putnis & Putnis, 2007; Stünitz & Gerald, 1993). A robust constrain on the metamorphic conditions, deformation mechanisms and timescale of shear zones activity is needed to better understand their role during orogenesis.

The Scandinavian Caledonides provide some of the best localities for investigating the relative roles and effects of these different inputs and controls on shearing, as they consist of a large-scale nappe stack of several tectonometamorphic units separated by thrusts that accommodated several hundreds of km of SE-directed tectonic transport during continental collision (e.g. Gee et al., 2013; Roberts, 2003). Peak metamorphic conditions and related ages are well documented in several of the tectonometamorphic units (e.g. Brueckner & Van Roermund, 2007; Janák et al., 2013; Ladenberger et al., 2013; Majka et al., 2014; Root & Corfu, 2012). However, fewer studies address the lower metamorphic grade evolution of such units, associated with their exhumation, juxtaposition and the ESE-directed tectonic transport over the Baltoscandian margin (e.g. Andersen, 1998; M. W. Anderson et al., 1992; Bender et al., 2018, 2019; Fossen & Rykkelid, 1992; Gilotti, 1989). Several open questions remain related to the pressure and temperature conditions of the low-grade metamorphism along the thrusts, the associated duration of thrusting, and the deformation processes that facilitated hundreds of km of tectonic transport.

In this study, we describe the evolution of metamorphic fabrics in a 1 km long crustal section provided by the “Collisional Orogeny in the Scandinavian Caledonides (COSC-1; IGSN ICDP5054EHW1001)” drill core (Lorenz et al., 2015; see section 2). We reconstruct the first pressure-temperature-time-deformation (P-T-t-d) path for the Lower Seve Nappe. We constrain the metamorphic conditions, deformation mechanisms and mineralogical changes related to these ductile and brittle fabrics using petrographic and microstructural analyses, thermodynamic modelling, electron backscattered diffraction analyses, and U-Pb geochronology on syn-kinematic

titanite. Our results suggest that the nappe experienced protracted and long-lasting shearing from epidote amphibolite facies conditions to greenschist facies conditions, with strain localization toward the tectonic contact with the underlying Särvi Nappe. Our study provides detailed insight into the role of a major thrust in the exhumation and stacking of orogenic tectonometamorphic units.

2. Geological setting

The Scandinavian Caledonides developed due to the Ordovician closure of the Iapetus Ocean and the subsequent Silurian to early Devonian subduction and continent collision of the Baltica plate below the Laurentian plate (e.g. Gee et al., 2008; Roberts, 2003; Roberts & Gee, 1985; Stephens, 1988). In the Scandinavian Caledonides, tectonic units were transported up to 400 km to the east during the collision, eventually creating a nappe stack of several allochthonous units on top of Autochthonous Baltic Shield (Figure 1a-b; (Gayer et al., 1987; Gee, 1975; Gee et al., 2010; Rice & Anderson, 2016)). After emplacement, the nappe stack was folded into north-trending synforms and antiforms, possibly related to either crustal extension and normal faulting or basement shortening occurring during the latest orogenic phases (Bergman & Sjöström, 1997; Rice & Anderson, 2016).

The Middle Allochthon, the target of this study, includes several basement units and associated metasediments representing the outermost Baltica margin, and possibly includes units derived from an ocean-continent transition zone (e.g. Andréasson, 1994; Gee et al., 2008; Janák et al., 2006; Roberts, 2003; Stephens, 1988). The upper tectonic unit of the Middle Allochthon, the Seve Nappe Complex (SNC; e.g. Sjöström, 1983), crops out over a N-S distance of ~1000 km and an W-E distance of ~200 km in the central part of the orogen (Figure 1; Andréasson, 1994).

In the Jämtland region, the SNC can be further subdivided into Lower, Middle and Upper Seve nappes by the presence of internal thrust sheets (Zachrisson & Sjöstrand, 1990). The Lower Seve Nappe is mainly composed of micaschists, quartzites and metapsammites with gneisses, metabasics and with minor peridotites and serpentinites (Figure 1c). The Middle Seve Nappe is composed of similar lithologies, but is overprinted by pervasive migmatization. Several parts of the Lower- and Middle Seve preserve evidence of high pressure (HP) to ultrahigh pressure (UHP) metamorphism (summary in Figure 4 of Klonowska et al., 2016 and Figure 6 and Table 2 of Bender et al., 2018) spanning from ~1.1 GPa and 600°C up to 4 GPa and 800°C, within the stability field

of coesite and diamond (Brueckner & van Roermund, 2004; Gilio et al., 2015; Janák et al., 2013; Klonowska et al., 2016, 2017; Majka et al., 2014; Van Roermund, 1985, 1989). The HP-UHP metamorphism is the manifestation of the Ordovician subduction of the SNC (Brueckner & Van Roermund, 2007; Ladenberger et al., 2013; Root & Corfu, 2012). To date, no evidence of (U)HP metamorphism has been recorded in the Lower Seve Nappe in central Jämtland.

In the Middle Seve Nappe, granulite and amphibolite facies metamorphism produced partial melting at 442–436 Ma (Ladenberger et al., 2013) and appear to postdate the HP-UHP stage, constrained around 472 ± 3 Ma (Petrík et al., 2019). In the Lower Seve Nappe, a pervasive amphibolite facies foliation overprints the (U)HP fabric, where present, and represents the main metamorphic fabric. The (U)HP fabrics are composed of garnet, omphacite, phengite, rutile and coesite (retrogressed in quartz) in the eclogites and quartz, phengite, garnet, jadeite, rutile in the gneiss (Klonowska et al., 2016 and Fassmer et al., 2017, respectively). In the Åreskutan area, a recent field study identified two foliations: a main foliation of epidote amphibolite to upper-greenschist facies conditions partially overprinted by a lower grade foliation subparallel to it; both have dip direction toward E-NE and mean dip value of 30° (Bender et al., 2018). Both foliations develop stretching lineations that plunge shallowly and have mean azimuths of 88° and 103° for the higher and lower grade, respectively, and associated sense of shear top-to-the-ESE (Bender et al., 2018). The epidote amphibolite facies metamorphic stage was constrained at $\sim 600^\circ\text{C}$ and 0.8–1 GPa in amphibolite (Giuntoli, Menegon, et al., 2018) and at 550°C and 0.2–0.5 GPa in micaschist (Arnbom, 1980) around ~ 430 Ma (Bender et al., 2019).

The COSC-1 borehole is located in the central Jämtland region, near Åre in Sweden (Lorenz et al., 2015; see location in Figure 1b-c). The drill core provides an almost complete section (recovery rate higher than 99%) through the Lower Seve Nappe. In detail, the core comprises alternating layers of felsic gneiss, calc-silicate and amphibolite displaying narrow (mm-cm) and localized shear zones from the surface down to 1700 m. Micaschist is more common below 1700 m. The rocks show strongly deformed mylonitic fabrics from 1700 m to the end of the core at 2500 m depth (Giuntoli, Menegon, et al., 2018; Hedin et al., 2016). Below 2350 m the core is composed of strongly deformed metasediments, interpreted as representing the basal shear zone juxtaposing the Lower Seve Nappe with the Särvi Nappe (Hedin et al., 2016; Lorenz et al., 2015). Acoustic televiewer data suggest that the regional foliation in the core is generally subhorizontal, with localised exceptions related to recumbent folds and boudinage (Wenning et al., 2017). The

vergence of the lower-grade folds indicates that folding was in part coeval with top-to-the-ESE shearing at greenschist facies conditions, as highlighted by field-based studies (Bender et al., 2018). Both in the field and in the core, lineations are oriented from E-W to SE-NW, with a mean trend/plunge 100°/20°, in agreement with the Caledonian transport direction (Merz et al., 2019).

3. Materials and Methods

3.1. Sample preparation and scanning electron microscopy

The drill core samples were oriented only with respect to the top of the borehole. The core declination reorientation allows to reorient the core with respect to the geographic north. This correction requires the identification of distinctive structures (e.g. folds), in both core scans and image logs (see Merz et al., 2019 for further details). This correction was not applied to the studied samples, as those were selected for their mylonitic fabrics that did not display distinctive structures essential for reorientation. Therefore, as core rotation around the vertical axis might have occurred during extraction, any reference to “dextral” sense of shear in the following sections is solely descriptive and does not carry information of actual direction of tectonic transport (see section 5.3 for discussion).

All scanning electron microscopy (SEM) analyses were performed on carbon-coated polished thin sections cut perpendicular to the foliation and parallel to the sample stretching lineation. Cathodoluminescence (CL) analyses were performed at the Open University (UK), using a FEI Quanta 200 three-dimensional SEM equipped with a Centaurus Deben panchromatic CL detector with a photo multiplier tube (Hamamatsu R316) characterized by sensitivity in the range of 400-1200 nm. Analyses were conducted under high vacuum, using an accelerating voltage of 10 kV, a beam current of 3.3 nA, a working distance of 13 mm, and an electron source provided by a tungsten filament.

Backscattered electron (BSE) and Electron backscattered diffraction (EBSD) analyses were conducted with a Jeol-7001FEG SEM at the Electron Microscopy Centre, Plymouth University (UK). EBSD patterns were acquired with a 70° tilted sample geometry, 20 kV accelerating voltage, a beam current of ~12.5 nA, 18-23 mm working distance and 1.3-1.7 µm step size. Diffraction patterns were automatically indexed using AZtec (Oxford Instruments). Raw maps were processed with HKL Channel 5 software (Oxford Instruments), following the procedure illustrated in Prior

et al., 1999, 2002, 2009. Crystallographic directions were plotted on pole figures (lower hemisphere of the stereographic projection), with X parallel to the stretching lineation and Z parallel to the pole of the mylonitic foliation, if not otherwise specified. Misorientation angle distributions were calculated for correlated pairs (with a shared boundary) and uncorrelated pairs, and were compared with the theoretical random distribution. Misorientation axes were plotted in crystal coordinates (lower hemisphere of the stereographic projection) for misorientations of 2°–10° measured across boundaries between neighbouring pairs (e.g. Prior et al., 2002; Wheeler et al., 2001). This misorientation range was chosen to investigate the nature of low-angle boundaries (e.g. Neumann, 2000). EBSD maps include phase maps, grain size maps (where the grain size is defined as the diameter of the equivalent circle) and grain orientation spread (GOS) maps. GOS is a measure of the internal strain of a grain defined as the average misorientation angle between each pixel in a grain and that grain's mean orientation (Wright et al., 2011).

3.2. Electron probe microanalyzer

EPMA analyses were conducted at the Open University (UK), using a five-spectrometer Cameca SX100. Wavelength dispersive spectrometers (WDS) provided data for both spot analyses and X-ray maps. Spot analyses were first acquired for each mineral phase, before X-ray maps were acquired from the same area. Spot analyses were performed with 20 KeV accelerating voltage, 20 nA specimen current and 2 µm beam diameter. Ten oxide compositions were measured, using natural standards: K-feldspar (SiO₂, Al₂O₃, K₂O), bustamite (CaO, MnO), hematite (FeO), forsterite (MgO), jadeite (Na₂O), rutile (TiO₂), apatite (P₂O₅). A ZAF matrix correction routine was applied; uncertainty on major element concentrations was <1%. X-ray maps were acquired with 15 KeV accelerating voltage, 100 nA specimen current, dwell times of 70-100 ms and step size of 5 µm. Ten elements (Si, Ti, Al, Fe, Mn, Mg, Na, Ca, K and P) were measured at the specific wavelength in two series. Intensity X-ray maps were standardized to concentration maps of oxide weight percentage using spot analyses as internal standard. X-ray maps were processed using XMapTools 2.6.4 (Lanari et al., 2014). Quantitative X-ray maps were used as input for isochemical phase diagram computation, following the strategy of Lanari & Engi (2017; see the following section).

3.3. Geothermobarometry

3.3.1. Isochemical phase diagrams (pseudosections)

Isochemical equilibrium phase diagrams were computed using the Gibbs free energy minimization algorithm Theriak–Domino (De Capitani & Brown, 1987; de Capitani & Petrakakis, 2010). The thermodynamic database of Berman (1988) with subsequent updates collected in JUN92.bs was used, together with the following solution models: Berman (1990) for garnet, Nagel et al. (2002) for staurolite, Fuhrman & Lindsley (1988) for feldspar, Keller et al. (2005) for white mica, and ideal mixing models for amphibole (Mäder & Berman, 1992; Mäder et al., 1994) and chlorite (Hunziker, 2003). Fe^{3+} was ignored because of the lack of analytical data and suitable ferric endmembers in solid solution models. Local bulk compositions were obtained using standardized X-ray maps (section 3.2) following the procedure described in Lanari & Engi (2017). As indicated by those authors, the chosen areas should be representative of the equilibrium volumes that were examined. Thus, it is important to evaluate if the results of thermodynamic modelling match the observed parageneses in term of modal amount of the mineral phases and their chemical compositions. The amounts of H_2O component used in the computations were estimated from the H_2O contents needed to stabilise the amount of hydrous minerals extracted from the local bulk composition. These values were in line with the measured loss of ignition values (1.4 – 4 wt %) of the present-day samples. Each garnet growth zone was sampled from the standardized X-ray maps. Successively, the program GrtMod (Lanari et al., 2017) was used to find the best analytical solution between measured and modelled composition of garnet. This computer program used an iterative approach that refined the P–T conditions for successive garnet growth zones. The program interacts with Theriak and uses the same thermodynamic database as the isochemical equilibrium phase diagrams (for further details see Giuntoli, Lanari, et al., 2018).

3.3.2. Amphibole-plagioclase thermobarometry

Temperature was estimated using Holland & Blundy (1994) geothermometer, which uses the equilibrium element exchange between amphibole and plagioclase pairs, constrained for silica-saturated and silica-rich igneous and metamorphic rocks in the range of 0.1–1.5 GPa and 400–1,000°C. Pressure was estimated using Bhadra & Bhattacharya (2007) and Anderson & Smith (1995) geobarometers. The first geobarometer is based on element distribution between amphibole and plagioclase pairs in equilibrium. Experimental data were acquired on silica-saturated

assemblages in the P–T range of 0.1–1.5 GPa and 650–950°C. The second geobarometer is based on the increase of Al in hornblende with increasing pressure and is calibrated on experimental data at 675 and 760°C.

3.3.3. Chlorite and white mica multi-equilibrium

To constrain the P–T conditions of retrograde stages, multi-equilibrium computations of the high-variance assemblages involving chlorite and white mica were performed, using the standard state properties and solid solution models of Vidal et al. (2005, 2006) for chlorite, Dubacq et al. (2010) for phengite, and the program ChlMicaEqui (Lanari, 2012; Lanari et al., 2012). The activity of H₂O was set to unity. In detail, the thermobarometry was based on the chlorite+white mica+quartz+H₂O equilibrium. The P and T of formation for each chlorite and white mica couple, as well as their respective XFe³⁺ values, were estimated by minimizing the square root of the sum of ($\Delta G_{\text{reaction}}$)² for the following six equilibria:

(1) - 4 Clinocllore + 4 Daphnite - 5 Fe-Amesite + 5 Mg-Amesite

(2) 14 alpha-Quartz - 4 Daphnite + 5 Fe-Amesite + 3 Mg-Amesite - 6 Sudoite + 8 WATER

(3) - 10 Mg-Celadonite + 15 alpha-Quartz - 2 Daphnite + 10 Fe-Celadonite + 2 Mg-Amesite - 4 Pyrophyllite + Sudoite

(4) 75 alpha-Quartz - 2 Clinocllore + 2 Daphnite - 10 Fe-Celadonite + 10 Muscovite - 20 Pyrophyllite + 5 Sudoite

(5) - 5 Mg-Celadonite + Clinocllore + 4 Daphnite - 5 Fe-Amesite + 5 Muscovite

(6) 2 Fe-Amesite - 8 Fe-Celadonite + 13 Mg-Amesite + 8 Muscovite + 14 Pyrophyllite - 26 Sudoite + 30 WATER

3.4. U-Pb geochronology by laser ablation-inductively coupled plasma-mass spectrometry (LA-ICP-MS)

Titanite grains were analysed for U-Pb isotopes using an ASI RESolution 193 nm ArF excimer laser coupled to a quadrupole Agilent 7500cs ICP-MS at the University of Portsmouth, following the procedure described in Papapavlou et al. (2017). The spot size was 30 µm, the laser fluence was approximately 3 J/cm² and the frequency 2 or 3 Hz. A sample-standard bracketing method was used to correct for mass fractionation, using Khan titanite as the primary standard (ID-TIMS

age of 522.2 ± 2.2 Ma, Heaman, 2009). Downhole U-Pb elemental fractionation was corrected using an exponential downhole correction fit to the time-resolved data for each analysis. A ^{207}Pb -based correction scheme was applied to the variably common lead-bearing primary standard using the Vizuage_UcomPbine add-in for Iolite (Chew et al., 2014). MKED-1 titanite was analysed as a secondary standards to evaluate accuracy of the method, and the resulting weighted mean $^{206}\text{Pb}/^{238}\text{U}$ age (1523.1 ± 4.0 Ma) and concordia age (1523.7 ± 5.5 Ma) are within uncertainty of reference values (ID-TIMS $^{206}\text{Pb}/^{238}\text{U}$ age of 1521.02 ± 0.55 Ma, Spandler et al., 2016). The $^{238}\text{U}/^{206}\text{Pb}$ and $^{207}\text{Pb}/^{206}\text{Pb}$ isotopic ratios for each analysis are presented uncorrected for common lead in Tera-Wasserburg concordia diagram using IsoplotR (Vermeesch, 2018).

4. Results

4.1. Petrography and microstructures

The micaschists and amphibolites from the lower part of the drill core (1500-2500 m; Figure 2) display a subhorizontal to moderately-dipping main fabric (S).

4.1.1. Micaschists

The three micaschist samples were collected at ~1700 m (sample 561), 2170 m (640), 2500 m (695; Table S1, Figures 2 and 3) depths, allowing the variation of fabrics through different levels of the nappe to be observed. The main S foliation consists of muscovite, biotite, quartz, plagioclase and epidote. Isolated porphyroclasts of plagioclase and biotite and muscovite mica fish grains are wrapped by the foliation (Figure 3). The foliation is mylonitic and a stretching lineation is observable in the hand specimens and is marked by rods of plagioclase and quartz and by elongated trails of muscovite and biotite. Both generations of micas (i.e. the mica fish and the grains along the foliation) display undulose extinction and bending (Figure 4). Millimetre-sized garnet and staurolite are present in sample 561. Dextral sense of shear is observed (Figure 3; note that the sense of shear is solely descriptive as explained in section 3.1). Accessory phases include pyrite, ilmenite, magnetite, apatite, calcite and zircon. In sample 695, plagioclase displays dark porphyroclastic core and bright rim in CL images (Figure 4g,h). The rims form asymmetric tails around the core, compatible with a dextral sense of shear, kinematic consistent with the main foliation. Microfractures are frequent in the cores and are sealed by plagioclase with a similar luminescence as the rim, as described in Giuntoli, Menegon, et al., 2018 (Figure 4g,h). Chlorite

crystallizes in the garnet asymmetric pressure shadows in sample 695, defining a dextral sense of shear.

The mylonitic S foliation is deformed by discrete 1 mm-spaced C'-type shear bands defined by chlorite and white mica (sample 640; Figures 3 and 4) which deform into sigmoidal-shaped white mica and biotite grains and quartz ribbons. These in turn define the main foliation. Towards the bottom of the drill core (e.g. sample 695), C and C'-type shear bands are more discrete and pervasive. Their spacing of some hundreds of μm produces a composite S-C-C' fabric (Figure 3c). Locally, these C and C' planes are extremely sharp and cut the surrounding minerals: for example, in plagioclase grains these planes truncate both growth zones (Figure 4 g). The C and C'-type shear bands display sense of shear identical to the main foliation. Note that even if the shear zone boundaries were not observed, the thickness of the mylonitic foliation (~ 1 km) and the high degree of transposition throughout the drill core suggest that the shear zone margins are likely parallel to the mylonitic foliation itself.

4.1.2. Amphibolites

Three mafic amphibolite samples were collected at depths of ~ 1625 m (sample 531), 1660 m (543), 1700 m (557; Table S1, Figures 2 and 5) and were compared with the results from amphibolite sample 648 collected at a depth of ~ 2200 m described in Giuntoli, Menegon, et al. (2018).

In the amphibolites the mylonitic S foliation is defined by amphibole, plagioclase, chlorite, quartz, epidote and ilmenite wrapping around bigger plagioclase porphyroclasts, with a dextral sense of shear (samples 531 and 543; Figures 5-7). Like in the micaschists, a stretching lineation is present on the hand specimen and is marked by the mineral defining the foliation. Rare zircon and apatite are present. Quartz and calcite veins occur subparallel to the mylonitic foliation. Amphibole displays a less pleochroic core, that varies from light green to light brown absorption colours, and a more pleochroic rim, that varies from dark green to dark brown (Figures 6a and 7a). The core is darker than the rim in BSE images (Figure 6c). Plagioclase cores are brighter in CL than the rims and display polysynthetic twinning (Figures 6b and 7b) The rims form asymmetric tails around the core, compatible with a dextral sense of shear, kinematic consistent with the main foliation. Like in the micaschists, a main shear plane is not visible in thin section, as the deformation is more diffuse.

Opaque minerals include ilmenite, up to 1 mm in size, and minor magnetite and pyrite, the latter cored by chalcopyrite. In sample 543 ilmenite and pyrite form layers parallel to the mylonitic foliation (Figure 5b). In all the samples, ilmenite grains are elongate and lie parallel to the mylonitic foliation. Ilmenite is rimmed by titanite, which also grows in the ilmenite boudin necks (Figures 7f and 8a). Titanite displays intergrowths with amphibole and plagioclase rims. A few titanite grains occur as elongate grains parallel to the main foliation, are up to some hundreds of μm in size and do not have ilmenite cores (Figure 8b). BSE images of titanite grains display homogeneous brightness (Figures 7g,h and 8f), with minor patchy areas (bottom part of Figure 8h). Standardized X-ray maps for titanite show some patchy variation <2 weight percentage in the oxides of the major elements (TiO_2 , CaO , SiO_2 in Figure 6g-i, respectively). These data do not highlight concentric zoning reflecting a core to rim growth.

4.2. Geothermobarometry

4.2.1. Isochemical phase diagrams on micaschists

Local bulk compositions used for isochemical phase diagrams computation are available in Table S2. The chosen areas match with the standardized X-ray maps of Figures 9, 10 and 11. In all the micaschist samples, standardized X-ray maps for garnet highlight concentric zoning, with a core richer in X_{Sps} than the rim (Figures 9, 10 and 11; Table 2). Muscovite is characterized by some relic phengitic cores that are richer in Si than the rims, the latter describing the main foliation. Plagioclase shows cores that are poorer in X_{Ab} than the rims in sample 561 (Figure 9f); this zoning is inverse in sample 695 (Figure 11d, o; Table 3).

In sample 561 GrtMod results predict the garnet core to be stable at ~ 0.4 GPa and 410°C (Figure 12a, the error bars departing from filled ellipses show the P–T uncertainty related to the analytical error of the garnet composition; see Lanari et al., 2017). The modelled composition is $\text{Alm}_{0.71}$, $\text{Prp}_{0.09}$, $\text{Grs}_{0.06}$, $\text{Sps}_{0.14}$, the measured composition is available in Table 2. The garnet rim is predicted stable at ~ 0.6 GPa and 430°C (modelled composition: $\text{Alm}_{0.71}$, $\text{Prp}_{0.12}$, $\text{Grs}_{0.09}$, $\text{Sps}_{0.09}$), but this result overlaps the garnet core within uncertainty. Thermodynamic modelling predicts a total of 8 volume % of garnet stable (estimated mineral assemblages in thin section available in Table S2). P–T conditions of garnet rim match with Si apfu isopleths of muscovite rim, X_{Ab} isopleths of plagioclase rims and X_{Mg} isopleths of staurolite and biotite (the latter within error). In summary, based on the intersections of the previous data, the most likely conditions computed for

the development of the foliation are ~0.55 GPa and 500°C (red dashed ellipsis in Figure 12a representing the P-T conditions of the metamorphic stages best fitting with the observed paragenesis and the computed isopleths). The predicted assemblage conforms to the minerals observed in thin section, except that kyanite was not detected in thin section (1.9 vol% predicted) and epidote is not predicted stable but is observed in thin section (~2 vol%; Table S2). Si apfu isopleths of phengitic muscovite cores would suggest a higher-pressure stage at ~1.1 GPa (red dashed ellipsis in Figure 12a), similarly to the other samples (see the next paragraphs). Plagioclase core X_{Ab} isopleths could indicate a higher-temperature stage of ~650°, although no other evidence is present for such higher temperature stage in the studied micaschist samples (see discussion section 5.1).

In sample 640 the garnet core and rim are modelled to be stable at similar pressure and temperature conditions of ~0.58 GPa and 520°C and 0.6 GPa and 530°C (Figure 12b, modelled composition: Alm_{0.69}, Prp_{0.06}, Grs_{0.18}, Sps_{0.07} and Alm_{0.70}, Prp_{0.06}, Grs_{0.19}, Sps_{0.05}). A total of ~2 vol% of garnet is predicted to crystallize. These P-T conditions match, within error, the Si apfu isopleths of muscovite marking the foliation, X_{Ab} isopleths of plagioclase and X_{Mg} isopleths of biotite (red dashed ellipsis in Figure 12b). The Si apfu isopleths of the rare phengitic muscovite cores suggest a higher-pressure stage. The predicted assemblage matches the minerals observed (Table S2).

In sample 695 the garnet core and rim are found to be stable at the same P-T conditions of ~1.2 GPa and 510°C (Figure 12c, modelled compositions: Alm_{0.63}, Prp_{0.04}, Grs_{0.18}, Sps_{0.15} and Alm_{0.65}, Prp_{0.04}, Grs_{0.18}, Sps_{0.13}). A total of ~9 vol% of garnet is predicted to crystallize. These conditions match with Si apfu isopleths of phengitic muscovite cores and with X_{Ab} isopleths of plagioclase core. Si apfu isopleths of muscovite marking the foliation intersect the X_{Mg} isopleths of biotite around 0.6 GPa and 500°C. At these metamorphic conditions the predicted assemblage is consistent with the minerals observed in thin section. For the three micaschist samples inferred P-T paths are indicated with the purple dashed line in Figure 12. These trajectories are drawn linking the red dashed ellipses and the chlorite and white mica multiequilibrium results (in samples 640 and 695; see section 4.2.3).

4.2.2. Amphibole-plagioclase thermobarometry on amphibolites

In the amphibolite samples, the standardized X-ray maps for plagioclase highlight poorer X_{Ab} porphyroclastic cores (0.64-0.74) and richer X_{Ab} syn-kinematic rims (0.74-0.82, Figures 6e and

7d; Table 3), results that perfectly match with the CL images (Figures 6b and 7b). Some fractures are visible in the core and are sealed by a plagioclase richer in albite content. Amphibole X_{Mg} map highlighting a richer X_{Mg} relic core and a poorer syn-kinematic rim (Figures 6f and 7e). In sample 531 thermometric estimates for the plagioclase rim and amphibole rim pairs yield 610°C ($\pm 50^{\circ}\text{C}$) for 0.77 GPa and 0.87 GPa (± 0.2 GPa; Bhadra & Bhattacharya, 2007 and J. L. Anderson & Smith, 1995 barometers, respectively). In sample 543 plagioclase rim and amphibole rim pairs yield 650°C for 0.40 GPa and 0.84 GPa (Table 1, see Section 5.1 for discussion).

4.2.3. Chlorite and white mica multi-equilibrium

The chlorite and white mica multi-equilibrium technique was used to constrain the equilibrium conditions of chlorite and white mica grains that developed on localized C and C'-type shear bands that deflect the main foliation. Chlorite and white mica couples crystallizing along C' planes (sample 640) and C planes (sample 695) equilibrated at the same pressure conditions of 0.3 ± 0.2 GPa for temperature of $310 \pm 50^{\circ}\text{C}$ and $370 \pm 50^{\circ}\text{C}$, respectively (Figure 13 and red dashed rectangles in Figure 12).

4.2.4. Summary of P-T results

The three micaschist samples record a similar P-T evolution that is characterised by three metamorphic stages. The first HP stage is constrained between 400 and 500°C and 1 - 1.3 GPa by the chemical composition of phengitic muscovite cores in all the samples, plus garnet and albite cores in sample 695 (M_{HP} in Figure 13c). These mineral phases are not associated with any obvious HP foliation, and are wrapped by the main mylonitic S foliation developed during the second stage. The mylonitic foliation is the main fabric throughout the middle and lower portion of the drill core, for a depth of ~ 1 km. It formed between 450 - 550°C and 0.5 - 0.8 GPa as constrained by muscovite rims and biotite, plus garnet and plagioclase in samples 561 and 640 (M_{Amp} in micaschists). In the amphibolite samples 531 and 543, amphibole-plagioclase thermobarometry constrains the development of the mylonitic foliation to 600 - 650°C and 0.8 GPa (M_{Amp} in amphibolites; Table 1; see section 5.1 for discussion). The third stage corresponds to the C and C' planes, which deform the mylonitic foliation. These planes are present only in the deepest samples 640 and 695 and are most pervasive in the latter. Model results based on the chemistry of chlorite and muscovite grains in textural equilibrium growing along such structures suggest P-T conditions of equilibration at ~ 0.3 GPa for temperature conditions of 300° - 350°C (M_{Gr} in Figure 13c).

4.3. EBSD analysis

4.3.1. Micaschists

In sample 640, the EBSD analysis was performed on a domain where the C' planes are well developed, in order to provide insight into the deformation mechanisms responsible for forming these structures. This domain consists of monomineralic quartz layers separated by thin (ca. 10 μm thick) discontinuous bands of muscovite and chlorite (Figure 14). Quartz average grain size is 30 μm , with maximum value of $\sim 150 \mu\text{m}$. Quartz grains display undulose extinction, lobate grain boundaries and several low-angle boundaries. Smaller grains with grain size between 20-40 μm are evident at the boundaries of larger grains (Figure 14c). Grain orientation spread (GOS) values varies from $< 1^\circ$ (generally in the smaller grains) to maximum values of $\sim 7^\circ$ (generally in the larger grains; Figure 14b). Pole figures show a well-defined crystallographic-preferred orientation (CPO) of the c-axis forming a short girdle slightly inclined to the YZ plane (Figure 14e). The misorientation angle distribution of both correlated and uncorrelated pairs show peaks at low angle misorientations (between 2° and 10°) and, for correlated misorientations, at around 60° , related to the Dauphiné twinning (Figure 14d; Lloyd, 2004; Menegon et al., 2011). The plots of misorientation axis in crystal coordinates for misorientations of 2° – 10° display a major cluster around the c-axis (Figure 14e).

In sample 695 the investigated monomineralic quartz layers occur along the mylonitic S foliation and are separated by C planes defined by chlorite and muscovite grains. A bigger muscovite crystal with a sigmoidal shape is dragged into a C plane, defining a dextral sense of shear consistent with the geometry of the S-C fabric. This domain was subdivided into four subsets based on the abrupt decrease of quartz grain size from the S foliation to the C planes. Subsets 1 and 2 were sampled along the S foliation, whereas subsets 3 and 4 were sampled along C planes (Figure 15). In subsets 1 and 2 the quartz average grain size is 36 μm and 10 μm , respectively, with maximum value of 150 μm in the former (Figure 15d). Quartz grains display undulose extinction, lobate grain boundaries and several low-angle boundaries. GOS values varies from $< 1.5^\circ$ (generally in grains smaller than 50 μm) to maximum values of $\sim 7.5^\circ$ (Figure 15c). Subset 1 pole figure shows a strong CPO of the c-axis forming a short girdle along the YZ plane centred on the Y direction (Figure 16a). Subset 2 display a c-axis distribution forming a short girdle at 45° to the YZ plane, synthetically inclined with the dextral sense of shear (Figure 16b). The misorientation angle

distributions of both correlated and uncorrelated pairs of the two subsets show strong peaks at low angle misorientations (between 2° and 10°) and, for correlated misorientations, at around 60° . Minor peaks are evident for values between 22° and 42° for uncorrelated pairs in subset 1. The plots of misorientation axis in crystal coordinates for misorientations of 2° – 10° of subsets 1 and 2 display a major cluster around the c-axis.

Both subsets 3 and 4 display an average grain size of $\sim 5 \mu\text{m}$. In subset 3 a decrease in grain size is visible moving towards the C plane and varies between 1.5 and $6 \mu\text{m}$ (Figure 15d). GOS values are related to the grain size, with values up to 4.5° in the bigger grains and $<1^\circ$ in the smaller grains (Figure 51c). For these two subsets no obvious CPO is evident in the pole figures (Figure 16c,d). The misorientation angle distributions of both correlated and uncorrelated pairs of the two subsets show strong peaks at low angle misorientations (between 2° and 10°), with higher values in subset 3 for correlated pairs, and for correlated misorientations at around 60° . The plots of misorientation axis in crystal coordinates for misorientations of 2° – 10° do not show any obvious cluster, although the limited amount of data points (especially for subset 4) does not allow to draw solid conclusions. Although the number of grains in our dataset is too small to perform solid statistical analysis of grain- and subgrain size, we note that subgrains within subset 1 are generally much bigger than those in subsets 2 and 3.

In both samples, muscovite and chlorite display a strong CPO with the poles of the (001) parallel to Z, and with the poles of (100) and (010) defining girdles lying on the XY plane (Figure S1). In particular, in sample 695 the asymmetry of the (001) maximum of muscovite confirms the dextral sense of shear (Dempsey et al., 2011).

4.3.2. Titanite grains in amphibolites

In sample 531 we investigated a pressure shadow between two sigmoidal plagioclase porphyroclasts composed of ilmenite grains rimmed by titanite, and a single grain of titanite elongated parallel to the mylonitic foliation (Figures 6 and 8, respectively; see section 4.1.2). Titanite is characterized by GOS values lower than 4° , with several grains displaying values lower than 1° (Figure 8c-g). The GOS values are related to the grain size, with the higher values found in larger grains. Titanite displays a weak CPO, with the (100) and [001] subparallel to the foliation and to the stretching lineation, respectively (Figure 8i).

4.4. U-Pb geochronology

Analysed titanite grains in amphibolite samples 531, 543 and 557 contained U concentrations of ~ 3 to 12, ~ 4 to 33 and ~ 1 to 15 ppm respectively (Table S3). Common-Pb-uncorrected data, plotted on Tera-Wasserburg diagrams (Figure 17), yield $^{238}\text{U}/^{206}\text{Pb}$ – $^{207}\text{Pb}/^{206}\text{Pb}$ isochrons with lower intercept dates of 429 ± 20 Ma (95% confidence interval with overdispersion; mean square of weighted deviation MSWD = 2.6), 417 ± 9 Ma (MSWD = 1.2) and 461 ± 21 Ma (MSWD = 1.5) in samples 531, 543 and 557, respectively. The $^{207}\text{Pb}/^{206}\text{Pb}$ ratios of common Pb incorporated into the titanite (taken from y-intercepts on Tera-Wasserburg concordia diagrams) are within uncertainty for samples 531 and 543 (0.816 ± 0.026 and 0.812 ± 0.019 , respectively). Sample 557 shows higher $^{207}\text{Pb}/^{206}\text{Pb}$ ratio of common Pb (0.933 ± 0.020) compared to the two other samples.

5. Discussion

5.1. P-T-t conditions of metamorphism and deformation

The pressure estimates calculated for amphibolite samples 531 and 543 are within error of each other for the two geobarometer calibrations (Table 1). However, the pressure calculated for sample 543 using the Bhadra & Bhattacharya (2007) geobarometer deviates by 0.4 GPa compared to the Anderson & Smith (1995) geobarometer. We suggest that the latter estimate is more reliable, as it lies within error of the results calculated for sample 531. Moreover, sample 531 was collected from a few tens of metres above 543 and it is characterised by the same fabrics and similar mineralogy. These data match the results of an amphibolite sample 648 collected from ~1000 m deeper in the drill-core (Giuntoli, Menegon, et al. 2018), suggesting that the evolution of the mylonitic foliation in the amphibolites is consistent through middle and lower portions of the drill-core. Notably, the amphibolite sample 648 of Giuntoli, Menegon, et al. (2018) recorded higher P conditions, up to 1 GPa, linked to the incipient stage of the mylonitic foliation development. In the same sample, chlorite-rich C' planes yielded T of 350–200°C using the Chlorite+Quartz+H₂O thermometry. These temperature results match with the conditions estimated for the C and C' planes in the micaschist samples (M_{Gr}; Figure 13).

The temperature estimates suggest a difference of 50-100°C between the mylonitic foliation (M_{Amp}) in the micaschists and the amphibolite. This ΔT could be either related to the two different methods used to constrain P and T conditions in the micaschists (isochemical phase diagrams,

section 4.2.1) and in the amphibolites (amphibole-plagioclase thermobarometry, section 4.2.2), or to re-equilibration of the micaschists at decreasing T during the development of the mylonitic foliation. Plagioclase core X_{Ab} isopleths in sample 561 also suggest a higher-temperature ($\sim 650^\circ$) stage (Figure 12 a), although no other evidence for higher temperatures is (now) recorded by the studied micaschist samples. We disregard the possibility that those two lithotypes were juxtaposed only after their temperature peak, thus experiencing different tectonometamorphic histories, as intercalated micaschist and amphibolite samples were collected along the drill core (Figure 2; see section 5.3 for further discussion).

Titanite U-Pb geochronology of amphibolite sample 543 yields a simple isochron that we interpret to reflect formation of the mylonitic foliation at 417 ± 9 Ma (MSWD = 1.2; Figure 17). The titanite U-Pb data from samples 531 and 557 are more complex. Sample 531 yields an isochron with an age that is within uncertainty of both samples (429 ± 20 Ma; MSWD = 2.6), whereas 557 yields an older age of 461 ± 21 Ma (MSWD = 1.5) and higher $^{207}\text{Pb}/^{206}\text{Pb}$ ratio compared to the previous samples. In all the analysed samples, the titanite microstructural data suggest that it formed with the mylonitic S foliation and no evidence of a core to rim growth is present in standardised X-ray maps and BSE images (see section 4.1.2). Therefore, the spread of ages, the large uncertainties and the relatively high MSWD of regressions in 531 and 557 could reflect the duration of the mylonitic foliation development (from higher temperature and pressure conditions to lower ones; Figure 18), with stages of titanite crystallization related to differences in local bulk compositions, fluid availability and mineral reactions (Papapavlou et al., 2017; Spencer et al., 2013). Titanite growing over a protracted time range has recently been documented both from other areas in the Caledonides (e.g. Faber et al., 2019; Gasser et al., 2015; Spencer et al., 2013) and in other similar geological settings (e.g. Walters & Kohn, 2017). We consider it unlikely that the titanites have experienced diffusional Pb loss during cooling, as the maximum temperature estimated in our samples is $600\text{--}650^\circ\text{C}$, lower than the effective closure temperature of titanite (e.g. Hartnady et al., 2019; Kohn, 2017; Spencer et al., 2013). Additionally, titanite was stable during deformation without any evidence of dissolution-precipitation processes (e.g. lobate or peninsular edges, mineral inclusions marking transient porosity; Putnis, 2015) and EBSD data show limited or no evidence of deformation by dislocation-creep. As these two deformation mechanisms could affect titanite age dating results, their absence, determined from microstructural observations, further supports our interpretation (Papapavlou et al., 2017; Walters & Kohn, 2017).

5.2. Progressive strain localization on C'- and C-type shear bands during protracted shearing

Micaschist samples 640 and 695 display a progressive reduction of the recrystallized grain size of quartz in proximity to the C and C' planes (Figure 4). The grain size reduction is more pronounced towards the C planes (sample 695, Figure 15d). In both samples, the strong peaks at low angle misorientations (between 2° and 10°; Figures 14d and 16) in the misorientation angle distribution are consistent with dynamic recrystallization by subgrain rotation, as adjacent grains formed by subgrain rotation recrystallization display low angular relationships due to crystallographic inheritance from the parental grain (Wheeler et al., 2001). The peak around 60° is associated with Dauphiné twinning (Menegon et al., 2011). Clustering of misorientation axes around $\langle c \rangle$ is consistent with prism $\langle a \rangle$ slip during recovery and development of tilt boundaries (Neumann, 2000). Furthermore, in micaschist sample 695 the misorientation angle distribution displays peaks higher than the random distribution up to 30°, compatible with progressive formation of high-angle boundaries due to continuous rotation of subgrains (Neumann, 2000). Quartz c-axis CPO in micaschist sample 640 is consistent with rhomb $\langle a \rangle$ as the dominant active slip system during dextral shear (Figure 14e; Heilbronner & Tullis, 2006; Schmid & Casey, 1986). In summary, microstructures in both samples indicate that quartz deformed by dislocation creep accompanied by dynamic recrystallization.

In sample 695, we interpret the quartz aggregates in the different subsets (Figure 15d) as the result of different stages of the microstructural evolution. The c-axis CPO of subset 1 is consistent with dominant prism $\langle a \rangle$ and rhomb $\langle a \rangle$ slip (Figure 16a). The c-axis CPO of subset 2 is dominated by a single girdle synthetically inclined with the dextral sense of shear of the sample, and consistent with the activity of rhomb $\langle a \rangle$, basal $\langle a \rangle$ and prism $\langle a \rangle$ slip (Figure 16b). The synthetic single girdle is weakened in subset 3, which, although it has been sampled in a dominantly monomineralic aggregate, shows an incipient stage of phase mixing, with the local occurrence of second phases at the quartz-quartz grain boundaries. We note that large grains of subset 3 contain subgrains of similar size to the surrounding recrystallized grains (arrows in Figure 15d). Thus, the high frequency of low angle misorientations in the misorientation angle distribution for subset 3, together with the clustering of misorientation axes around $\langle c \rangle$, indicates that the main deformation mechanism in the largely monomineralic subset 3 was still dislocation creep, and that dynamic recrystallization predominantly occurred by progressive subgrain rotation. The number of recrystallized grains in the subsets of sample 695 is too low to estimate differential stresses with

paleopiezometers (e.g. Cross et al., 2017; Stipp & Tullis, 2003). Our preferred interpretation, based also on the qualitative observation of subgrain size in the different subsets, is that the decrease in recrystallised grain size from subset 1 to subset 3 results from a progressive increase of differential stress and strain rate during strain localization under decreasing T (e.g. Hirth & Tullis, 1992; Stipp et al., 2002). However, a larger EBSD dataset would be necessary to properly validate this interpretation.

Subset 4 does not show an obvious CPO, and various processes could have concurred in the development of its microstructure. The lack of CPO, coupled with the fine grain size and phase mixing could result from dominant grain size sensitive creep deformation in polyphase C-type bands (Figure 16c-d). A similar evolution of quartz c-axis CPO during progressive dismembering of monomineralic aggregates and transition to dominant grain size sensitive creep deformation in polyphase mixtures was described in Kilian et al., (2011), Viegas et al., (2016) and in Gilgannon et al., (2017). However, we note that subsets 3 and 4 are located along C planes and some of the quartz grains are truncated and pinned against chlorite and muscovite grains (Figure 15 b-d; e.g. Song & Ree, 2007). Moreover, both plagioclase core and rims are cut by the C planes, as described in section 4.1 (Figure 4g). This suggests that the C planes formed brittly after the progressive increase of strain rate recorded by the microstructure of quartz, and are the latest microstructure recorded by the rock. Thus, micro-fracturing of quartz grains could also occur during the formation of the C planes and contribute to grain size reduction and phase mixing observed in subset 4. Successively, these quartz grains could have experience healing by strain-induced grain boundary migration (e.g. Lagoeiro & Barbosa, 2010; Trepmann et al., 2007).

In both micaschist samples, muscovite and chlorite grains display undulose extinction, bending and strong CPO compatible with slip on the (001) plane (Figure S1). The presence of chlorite and muscovite crystallizing as neoblasts along C and C' planes, the dragging of the surrounding bigger muscovite grains into these planes forming mica fish, and the quartz grain size decrease by subgrain rotation recrystallization near to these planes suggest that the C planes evolved into ductile planes after a first initial brittle stage. Furthermore, these data imply that fluid influx occurred after fracturing preferentially along these brittle planes and their immediate damage zone, allowing the crystallization of chlorite and muscovite as neoblasts, since at 300°-350°C solid state diffusion is too slow and inefficient to account for the formation of those minerals (e.g. Ferry, 1994; Putnis & Putnis, 2007; Figure 18). Similarly, the main mylonitic foliation, which developed

under epidote amphibolite facies conditions, was locally overprinted at lower pressure, as for example highlighted by the presence of chlorite in the asymmetric pressure shadows around garnet (Figure 4d) and by the progressive retrogression of biotite into chlorite in proximity of the C and C' planes (Figure 10g). However, biotite is still preserved along most of the main mylonitic foliation (Figure 10h), thus suggesting that retrogression is mostly localised. This observation further confirms that the main infiltration of fluid occurred along the C and C' planes (e.g. Bukovská et al., 2016; Leclère et al., 2016; Wassmann & Stöckhert, 2013).

The presence of these discrete muscovite- and chlorite-rich planes promoted connectivity between weak phyllosilicate grains that strongly localised deformation and weakened the rock (Bukovská et al., 2016; Ceccato et al., 2018; Hunter et al., 2016; Mariani et al., 2006; Menegon et al., 2008; Shea & Kronenberg, 1993; Wintsch et al., 1995). Finally, the presence of such phyllosilicate-rich planes can accommodate large amount of strain, through the new mechanism of ripplocation motion (i.e. the motion of a new type of crystal defect – ripplocation – that involves a ripple of the basal layer and a basal dislocation, where the ripple enables c-axis parallel deformation in phyllosilicates; Kushima et al., 2015) rather than dislocation glide, as recently suggested by Aslin et al. (2019).

5.3. Evolution of the Lower Seve Nappe and implications for the Scandinavian Caledonides

As presented in section 2, mylonitic fabrics are dominant from 1700 m to the end of the core at 2500 m depths. Additionally, the lowermost portion of the core is composed of strongly deformed metasediments, interpreted as representing the basal shear zone juxtaposing the Lower Seve Nappe with the Särvi Nappe (Giuntoli, Menegon, et al., 2018; Hedin et al., 2016; Lorenz et al., 2015). The data presented in this study quantify the metamorphic conditions and characterise the deformation mechanisms of the Lower Seve Nappe and represent the first P-T-t-d path for this unit (Figure 18). Our data suggest that the Lower Seve Nappe attained peak metamorphic conditions of 400-500 °C and 1-1.3 GPa (M_{HP} in Figure 18). No fabrics are preserved for this metamorphic stage.

The older titanite dates found in this study (460-430 Ma; Figure 18) could be related to titanite growth during decompression from the peak metamorphic conditions to the incipient stages of development of the mylonitic foliation at amphibolite facies conditions (600-650°C and 0.8-1 GPa; M_{amp} in amphibolites). A similar age range of 470-445 Ma was found to reflect the eclogite facies metamorphism in the Middle Seve Nappe and other portions of the Lower Seve Nappe (Brueckner

& Van Roermund, 2007; Fassmer et al., 2017; Petřík et al., 2019; Root & Corfu, 2012). In the Middle Seve successive exhumation, decompression melting and granulite facies metamorphism were constrained at 440-445 Ma and crystallization of felsic segregation and pegmatites, crosscutting the previous HT fabrics, occurred at ~435-428 Ma (Grimmer et al., 2015; Klonowska et al., 2017; Ladenberger et al., 2013; Majka et al., 2012). The tectonic contact between the Middle and Lower Seve Nappes was considered active between 434-426 Ma in several studies (Bender et al., 2019; Dallmeyer, 1990; Dallmeyer et al., 1985; Grimmer et al., 2015; Hacker & Gans, 2005). U–Pb titanite TIMS data from a metapsammite of the Lower Seve Nappe directly beneath the tectonic contact suggested crystallisation between 437–427 Ma (Gromet et al., 1996). Moreover, a date of 426.0 ± 6.0 Ma was obtained by in-situ U–Th–Pb on monazite from a sheared migmatite at the base of the Middle Seve Nappe (Åreskutan basal shear zone; Majka et al., 2012). No P-T estimates are available for this fabric, but the minerals stable (and possibly growing) during this intense deformation period include garnet, biotite, sillimanite (fibrolite), kyanite, muscovite, and plagioclase (Arnbom, 1980) and suggest upper amphibolite facies conditions (e.g. Spear et al., 1999). Thus, the mylonitic foliation developed at the base of the Middle Seve Nappe records a similar P-T-t evolution to that proposed in this study for the Lower Seve Nappe, but at slightly higher temperature. It is worth noting that that no evidence was found for metamorphism at UHP eclogite or granulite facies conditions in the Lower Seve Nappe in central Jämtland, supporting the idea that this nappe was juxtaposed with the Middle Seve Nappe as the latter was exhumed.

Successively, the Lower Seve Nappe experienced further decompression to 0.8-0.5 GPa and 600-500°C at 417 ± 9 Ma (data from this study; M_{amp} in amphibolites and micaschists), the expression of which is the mylonitic foliation of epidote amphibolite facies conditions throughout middle and lower portion of the drill core (>1000 m of thickness). Similar conditions of 480-600° C and 1-1.1 GPa were described for the Lower Seve Nappe westward from the study area (Bergman, 1992). Regionally, this foliation is associated with a stretching lineation with a E-W trend and a top-to-the-east sense of shear (Bender et al., 2018). Northward from the study area, this foliation was dated to 432 ± 8 Ma by Rb–Sr multi-mineral isochron techniques (Gäddede area, Bender et al., 2019). This date corresponds, within uncertainty, with our study, although we cannot exclude that these dates captured two successive stages of the mylonitic foliation development, or that minor age differences exist between different areas of the Lower Seve Nappe.

The retrograde evolution continued with the development of brittle to ductile C and C' planes of greenschist facies between 400 and 300°C and ~0.3 GPa (M_{gr} in Figure 18). This fabric is visible in the lower part of the drill core (~500 m of thickness) and is more pervasive towards the bottom. It is believed to represent the thrust responsible for the juxtaposition of the Lower Seve Nappe above the Särvi Nappe (Hedin et al., 2016; Lorenz et al., 2015). These fabrics are also described from surrounding areas and correspond to the greenschist facies mylonitic zone that divides the Lower Seve Nappe from the lower Särvi Nappe (Arnbom, 1980), with a top-to-the-E-SE sense of shear (Bender et al., 2018). In particular, the latter authors did not observe any opposite sense of shear for both fabrics. Therefore, we suggest that the asymmetric fabrics recorded by our samples are compatible with a top-to-the-E-SE sense of shear.

No age data is available for the younger fabric, but it could be coeval with cooling of the Seve Nappe Complex below 350°C at ~415 Ma (Hacker & Gans, 2005) and with the younger date of 414 ± 4 Ma related to the development of the greenschist facies foliation in several nappes of the central Scandinavian Caledonides (Middle Köli Nappe, Upper Seve Nappe and Lower Allochthon; Figure 7 of Bender et al., 2019). The youngest age constraint is provided by the date of ~400 Ma, marking the onset of normal faulting cross-cutting the tectonic contacts between the pre-structured Nappes ($^{40}\text{Ar}/^{39}\text{Ar}$ cooling ages on white mica; Andersen, 1998; Fossen, 2000).

In summary, we suggest that the fabrics described in this paper formed due to protracted and long-lasting shearing from epidote amphibolite to greenschist facies conditions during exhumation and stacking of the Lower Seve Nappe with the Middle Seve Nappe (above) and the Särvi Nappe (below). We agree with previous interpretations that the emplacement and juxtapositions of the different tectonometamorphic units occurred by a series of in- and out-of-sequence thrusts, together with syn-thrusting exhumation, starting at granulite facies conditions in the Middle Seve Nappe and at amphibolite and greenschist facies conditions in all the other nappes (Bender et al. (2018, 2019). Moreover, this study highlights that (1) late (presumably out-of-sequence) Caledonian thrusting appears to be facilitated by fracturing and fluid infiltration along discrete, localised shear bands, and (2) exhumation of the Lower Seve Nappe from ca. 1 GPa to ca. 0.3 GPa was coeval with crustal shortening, similar to what observed in the hinterland of other mountain belts (e.g. Le Bayon & Balleve, 2006).

6. Conclusions

A multi-analysis approach including petrographic and microstructural analyses, thermodynamic modeling, EBSD analyses and age dating has allowed the reconstruction of the first pressure-temperature-time-deformation path for the COSC-1 drill core (Lower Seve Nappe) in the Scandinavian Caledonides. The data suggest that the ~1 km thick main mylonitic foliation formed at epidote amphibolite facies conditions during the retrograde path from 600 °C - 1 GPa to 500° - 0.5 GPa at around 417 ± 9 Ma. The older ages found in the amphibolites (460-430 Ma) may be related to incipient stages of development of the mylonitic amphibolite facies foliation. Mineral relics in micaschists highlight an older high-pressure stage between 400-500 °C and 1-1.3 GPa.

Towards the bottom of the drill core the mylonitic foliation is overprinted by a discrete, brittle-to-ductile C and C' shear bands, developed at lower metamorphic conditions of 300-400 °C and ~0.3 GPa. An initial brittle failure allowed preferential fluid influx along these planes and facilitated the neo-crystallization of chlorite and white mica. Strain localized proximal to those planes, as reflected by grain size reduction due to subgrain rotation recrystallization in the quartz rich layers. Incipient to progressive dismembering of monomineralic aggregates occurred, with transition to dominant grain size sensitive creep deformation in polyphase mixtures that further weakened the rock. We interpret this fabric as the expression of the thrust at the base of the Seve Nappe Complex, responsible for the exhumation and juxtaposition of this nappe with the lower Särvi Nappe. The age range for this younger fabric is comprised between 417 (the youngest age of the main mylonitic foliation) and 400 Ma, the latter age marking the onset of normal faulting in the Scandinavian Caledonides.

The results suggest that these fabrics formed due to protracted and long-lasting shearing from epidote amphibolite to greenschist facies conditions and facilitated the exhumation and juxtaposition of the Seve Nappe Complex against the Särvi Nappe in the Caledonian nappe stack.

Acknowledgments

The data presented in the manuscript are available in the main text, tables, figures, supporting information, in the references and in the Mendeley Data repository <http://dx.doi.org/10.17632/2v6rj69mzv.2>. A. Ceccato, I. Klonowska and J. Majka are acknowledged for fruitful discussions. S. Hammond and D. Johnson are warmly thanked for the

help with EPMA and SEM analyses, respectively. The staff at Plymouth University Electron Microscopy Centre is acknowledged for the support during EBSD analysis. Lucy Campbell is thanked for her help with Channel 5. B. Almqvist and N. Roberts are acknowledged for their support in acquiring the samples. This work was funded by an Early Postdoc.Mobility grant (project number: P2BEP2_168722) by the Swiss National Science Foundation to FG, and by a FP7 Marie Curie Career Integration Grant to LM (grant agreement PCIG13-GA-2013-618289). The COSC-1 drilling operations were supported by the International Continental Scientific Drilling Program (ICDP) and the Swedish Research Council (Vetenskapsrådet), and the Swedish national research infrastructure for scientific drilling “Riksrigger”. We thank Elisabetta Mariani, Zoe Braden, Richard D. Law and Calvin Mako for their very thorough reviews and Laurent Jolivet for editorial handling.

References

- Andersen, T. B. (1998). Extensional tectonics in the Caledonides of southern Norway, an overview. *Tectonophysics*, 285(3), 333–351.
- Anderson, J. L., & Smith, D. R. (1995). The effects of temperature and fO_2 on the Al-in-hornblende barometer. *American Mineralogist*, 80(5–6), 549–559.
- Anderson, M. W., Barker, A. J., Bennett, D. G., & Dallmeyer, R. D. (1992). A tectonic model for Scandian terrane accretion in the northern Scandinavian Caledonides. *Journal of the Geological Society*, 149(5), 727–741.
- Andréasson, P. G. (1994). The Baltoscandian margin in Neoproterozoic-early Palaeozoic times. Some constraints on terrane derivation and accretion in the Arctic Scandinavian Caledonides. *Tectonophysics*, 231(1–3), 1–32.
- Arnbom, J.-O. (1980). Metamorphism of the Seve Nappes at Åreskutan, Swedish Caledonides. *Geologiska Föreningen i Stockholm Förhandlingar*, 102, 359–371. <https://doi.org/10.1080/11035898009454493>
- Aslin, J., Mariani, E., Dawson, K., & Barsoum, M. W. (2019). Ripplations provide a new mechanism for the deformation of phyllosilicates in the lithosphere. *Nature Communications*, 10(1), 686. <https://doi.org/10.1038/s41467-019-08587-2>
- Austrheim, H. (1987). Eclogitization of lower crustal granulites by fluid migration through shear

737 zones. *Earth and Planetary Science Letters*, 81, 221–232. <https://doi.org/10.1016/0012->
738 821X(87)90158-0

739 Le Bayon, B., & Ballevre, M. (2006). Deformation history of a subducted continental crust (Gran
740 Paradiso, Western Alps): continuing crustal shortening during exhumation. *Journal of*
741 *Structural Geology*, 28(5), 793–815.

742 Bender, H., Ring, U., Almqvist, B. S. G., Grasemann, B., & Stephens, M. B. (2018). Metamorphic
743 zonation by out-of-sequence thrusting at back-stepping subduction zones: Sequential
744 accretion of the Caledonian internides, central Sweden. *Tectonics*.

745 Bender, H., Glodny, J., & Ring, U. (2019). Absolute timing of Caledonian orogenic wedge
746 assembly, Central Sweden, constrained by Rb–Sr multi-mineral isochron data. *Lithos*, 344–
747 345, 339–359. <https://doi.org/https://doi.org/10.1016/j.lithos.2019.06.033>

748 Bergman, S. (1992). P–T paths in the Handöl area, central Scandinavia: record of Caledonian
749 accretion of outboard rocks to the Baltoscandian margin. *Journal of Metamorphic Geology*,
750 10(2), 265–281. <https://doi.org/10.1111/j.1525-1314.1992.tb00082.x>

751 Bergman, S., & Sjöström, H. (1997). Accretion and lateral extension in an orogenic wedge:
752 evidence from a segment of the Seve-Ko“li terrane boundary, central Scandinavian
753 Caledonides. *Journal of Structural Geology*, 19(8), 1073–1091.
754 [https://doi.org/http://dx.doi.org/10.1016/S0191-8141\(97\)00028-X](https://doi.org/http://dx.doi.org/10.1016/S0191-8141(97)00028-X)

755 Berman, R. G. (1988). Internally consistent thermodynamic data for minerals in the system Na₂O–
756 K₂O–CaO–MgO–FeO–Fe₂O₃–Al₂O₃–SiO₂–TiO₂–H₂O–CO₂. *Journal of Petrology*, 29(2),
757 445–522.

758 Berman, R. G. (1990). Mixing properties of Ca–Mg–Fe–Mn garnets. *American Mineralogist*, 75,
759 328–344.

760 Bhadra, S., & Bhattacharya, A. (2007). The barometer tremolite+ tschermakite+ 2 albite= 2
761 pargasite+ 8 quartz: Constraints from experimental data at unit silica activity, with application
762 to garnet-free natural assemblages. *American Mineralogist*, 92(4), 491–502.

763 Brander, L., Svahnberg, H., & Piazzolo, S. (2012). Brittle-plastic deformation in initially dry rocks
764 at fluid-present conditions: transient behaviour of feldspar at mid-crustal levels.
765 *Contributions to Mineralogy and Petrology*, 163(3), 403–425.

766 Brueckner, H. K., & van Roermund, H. L. M. (2004). Dunk tectonics: a multiple
 767 subduction/eduction model for the evolution of the Scandinavian Caledonides. *Tectonics*,
 768 23(2).

769 Brueckner, H. K., & Van Roermund, H. L. M. (2007). Concurrent HP metamorphism on both
 770 margins of Iapetus: Ordovician ages for eclogites and garnet pyroxenites from the Seve Nappe
 771 Complex, Swedish Caledonides. *Journal of the Geological Society*, 164(1), 117–128.

772 Bukovská, Z., Jeřábek, P., & Morales, L. F. G. (2016). Major softening at brittle-ductile transition
 773 due to interplay between chemical and deformation processes: An insight from evolution of
 774 shear bands in the South Armorican Shear Zone. *Journal of Geophysical Research: Solid*
 775 *Earth*, 121(2), 1158–1182. <https://doi.org/10.1002/2015JB012319>

776 de Capitani, C., & Petrakakis, K. (2010). The computation of equilibrium assemblage diagrams
 777 with Theriak/Domino software. *American Mineralogist*, 95(7), 1006–1016.
 778 <https://doi.org/10.2138/am.2010.3354>

779 De Capitani, C., & Brown, T. H. (1987). The computation of chemical equilibrium in complex
 780 systems containing non-ideal solutions. *Geochimica et Cosmochimica Acta*, 51, 2639–2652.

781 Ceccato, A., Menegon, L., Pennacchioni, G., & Morales, L. F. G. (2018). Myrmekite and strain
 782 weakening in granitoid mylonites. *Solid Earth*, 9(6), 1399–1419. [https://doi.org/10.5194/se-](https://doi.org/10.5194/se-9-1399-2018)
 783 [9-1399-2018](https://doi.org/10.5194/se-9-1399-2018)

784 Chew, D. M., Petrus, J. A., & Kamber, B. S. (2014). U–Pb LA–ICPMS dating using accessory
 785 mineral standards with variable common Pb. *Chemical Geology*, 363, 185–199.
 786 <https://doi.org/https://doi.org/10.1016/j.chemgeo.2013.11.006>

787 Cross, A. J., Prior, D. J., Stipp, M., & Kidder, S. (2017). The recrystallized grain size piezometer
 788 for quartz: An EBSD-based calibration. *Geophysical Research Letters*, 44(13), 6667–6674.

789 Dallmeyer, R. D. (1990). ⁴⁰Ar/³⁹Ar mineral age record of a polyorogenic evolution within the
 790 Seve and Köli nappes, Trøndelag, Norway. *Tectonophysics*, 179(3–4), 199–226.

791 Dallmeyer, R. D., Gee, D. G., & Beckholmen, M. (1985). ⁴⁰Ar/³⁹Ar mineral age record of early
 792 Caledonian tectonothermal activity in the Baltoscandian Miogeocline, central Scandinavia.
 793 *American Journal of Science*, 285(6), 532–568.

794 Dempsey, E. D., Prior, D. J., Mariani, E., Toy, V. G., & Tatham, D. J. (2011). Mica-controlled
795 anisotropy within mid-to-upper crustal mylonites: an EBSD study of mica fabrics in the
796 Alpine Fault Zone, New Zealand. *Geological Society, London, Special Publications*, 360(1),
797 33–47.

798 Dubacq, B., Vidal, O., & De Andrade, V. (2010). Dehydration of dioctahedral aluminous
799 phyllosilicates: thermodynamic modelling and implications for thermobarometric estimates.
800 *Contributions to Mineralogy and Petrology*, 159(2), 159.

801 Faber, C., Stünitz, H., Gasser, D., Jeřábek, P., Kraus, K., Corfu, F., et al. (2019). Anticlockwise
802 metamorphic pressure–temperature paths and nappe stacking in the Reisa Nappe Complex in
803 the Scandinavian Caledonides, northern Norway: evidence for weakening of lower
804 continental crust before and during continental collision. *Solid Earth*, 10(1), 117–148.
805 <https://doi.org/10.5194/se-10-117-2019>

806 Fassmer, K., Klonowska, I., Walczak, K., Andersson, B., Froitzheim, N., Majka, J., et al. (2017).
807 Middle Ordovician subduction of continental crust in the Scandinavian Caledonides: an
808 example from Tjeliken, Seve Nappe Complex, Sweden. *Contributions to Mineralogy and*
809 *Petrology*, 172(11–12), 103.

810 Ferry, J. M. (1994). A historical review of metamorphic fluid flow. *Journal of Geophysical*
811 *Research*, 99(B8), 15,415–487,498.

812 Fossen, H. (2000). Extensional tectonics in the Caledonides: Synorogenic or postorogenic?
813 *Tectonics*, 19(2), 213–224.

814 Fossen, H., & Rykkelid, E. (1992). Postcollisional extension of the Caledonide orogen in
815 Scandinavia: Structural expressions and tectonic significance. *Geology*, 20(8), 737–740.

816 Fuhrman, M. L., & Lindsley, D. H. (1988). Ternary-feldspar modeling and thermometry. *American*
817 *Mineralogist*, 73, 201–216.

818 Fusseis, F., Handy, M. R., & Schrank, C. (2006). Networking of shear zones at the brittle-to-
819 viscous transition (Cap de Creus, NE Spain). *Journal of Structural Geology*, 28(7), 1228–
820 1243.

821 Gasser, D., Jeřábek, P., Faber, C., Stünitz, H., Menegon, L., Corfu, F., et al. (2015). Behaviour of
822 geochronometers and timing of metamorphic reactions during deformation at lower crustal

823 conditions: phase equilibrium modelling and U–Pb dating of zircon, monazite, rutile and
824 titanite from the Kalak Nappe Complex, northern Norway. *Journal of Metamorphic Geology*,
825 33(5), 513–534.

826 Gayer, R. A., Rice, A. H. N., Roberts, D., Townsend, C., & Welbon, A. (1987). Restoration of the
827 Caledonian Baltoscandian margin from balanced cross-sections: the problem of excess
828 continental crust. *Transactions of the Royal Society of Edinburgh: Earth Sciences*, 78(03),
829 197–217.

830 Gee, D. G. (1975). A tectonic model for the central part of the Scandinavian Caledonides.
831 *American Journal of Science*, 275(A), 468–515.

832 Gee, D. G., Fossen, H., Henriksen, N., & Higgins, A. K. (2008). From the early Paleozoic
833 platforms of Baltica and Laurentia to the Caledonide Orogen of Scandinavia and Greenland.
834 *Episodes*, 31(1), 44–51.

835 Gee, D. G., Juhlin, C., Pascal, C., & Robinson, P. (2010). Collisional orogeny in the Scandinavian
836 Caledonides (COSC). *Gff*, 132(1), 29–44.

837 Gee, D. G., Janák, M., Majka, J., Robinson, P., & van Roermund, H. (2013). Subduction along
838 and within the Baltoscandian margin during closing of the Iapetus Ocean and Baltica-
839 Laurentia collision. *Lithosphere*, 5(2), 169–178.

840 Gerald, J. D. F., & Stünitz, H. (1993). Deformation of granitoids at low metamorphic grade. I:
841 Reactions and grain size reduction. *Tectonophysics*, 221(3), 269–297.

842 Gilgannon, J., Fousseis, F., Menegon, L., Regenauer-Lieb, K., & Buckman, J. (2017). Hierarchical
843 creep cavity formation in an ultramylonite and implications for phase mixing. *Solid Earth*,
844 8(6), 1193–1209. <https://doi.org/10.5194/se-8-1193-2017>

845 Gilio, M., Clos, F., & van Roermund, H. L. M. (2015). The Friningen Garnet Peridotite (central
846 Swedish Caledonides). A good example of the characteristic PTt path of a cold mantle wedge
847 garnet peridotite. *Lithos*, 230, 1–16.

848 Gilotti, J. A. (1989). Reaction progress during mylonitization of basaltic dikes along the Särsv
849 thrust, Swedish Caledonides. *Contributions to Mineralogy and Petrology*, 101(1), 30–45.

850 Giuntoli, F., & Engi, M. (2016). Internal geometry of the central Sesia Zone (Aosta Valley, Italy):

851 HP tectonic assembly of continental slices. *Swiss Journal of Geosciences*, 109(3), 445–471.

852 Giuntoli, F., Lanari, P., Burn, M., Eva Kunz, B., & Engi, M. (2018). Deeply subducted continental
853 fragments - Part 2: Insight from petrochronology in the central Sesia Zone (western Italian
854 Alps). *Solid Earth*, 9(1). <https://doi.org/10.5194/se-9-191-2018>

855 Giuntoli, F., Menegon, L., & Warren, C. J. (2018). Replacement reactions and deformation by
856 dissolution and precipitation processes in amphibolites. *Journal of Metamorphic Geology*,
857 36(9), 1263–1286. [https://doi.org/https://doi.org/10.1111/jmg.12445](https://doi.org/10.1111/jmg.12445)

858 Giuntoli, F., Vitale Brovarone, A., & Menegon, L. (2020). Feedback between high-pressure
859 genesis of abiogenic methane and strain localization in subducted carbonate rocks. *Scientific*
860 *Reports*, 10(1), 9848. <https://doi.org/10.1038/s41598-020-66640-3>

861 Grimmer, J. C., Glodny, J., Drüppel, K., Greiling, R. O., & Kontny, A. (2015). Early-to mid-
862 Silurian extrusion wedge tectonics in the central Scandinavian Caledonides. *Geology*, 43(4),
863 347–350.

864 Gromet, L. P., Sjöström, H., Bergman, S., Claesson, S., Essex, R. M., Andréasson, P. G., &
865 Albrecht, L. (1996). Contrasting ages of metamorphism in the Seve nappes: U-Pb results from
866 the central and northern Swedish Caledonides. *GFF*, 118(sup004), 36–37.
867 <https://doi.org/10.1080/11035899609546308>

868 Hacker, B. R., & Gans, P. B. (2005). Continental collisions and the creation of ultrahigh-pressure
869 terranes: Petrology and thermochronology of nappes in the central Scandinavian Caledonides.
870 *Geological Society of America Bulletin*, 117(1–2), 117–134.

871 Hartnady, M. I. H., Kirkland, C. L., Clark, C., Spaggiari, C. V., Smithies, R. H., Evans, N. J., &
872 McDonald, B. J. (2019). Titanite dates crystallisation; slow Pb diffusion during super-solidus
873 re-equilibration. *Journal of Metamorphic Geology*, 0(ja). <https://doi.org/10.1111/jmg.12489>

874 Heaman, L. M. (2009). The application of U–Pb geochronology to mafic, ultramafic and alkaline
875 rocks: An evaluation of three mineral standards. *Chemical Geology*, 261(1), 43–52.
876 <https://doi.org/https://doi.org/10.1016/j.chemgeo.2008.10.021>

877 Hedin, P., Almqvist, B., Berthet, T., Juhlin, C., Buske, S., Simon, H., et al. (2016). 3D reflection
878 seismic imaging at the 2.5 km deep COSC-1 scientific borehole, central Scandinavian
879 Caledonides. *Tectonophysics*, 689, 40–55.

880 Heilbronner, R., & Tullis, J. (2006). Evolution of c axis pole figures and grain size during dynamic
881 recrystallization: results from experimentally sheared quartzite. *Journal of Geophysical*
882 *Research: Solid Earth*, 111.

883 Hirth, G., & Tullis, J. A. N. (1992). Dislocation creep regimes in quartz aggregates. *Journal of*
884 *Structural Geology*, 14(2), 145–159.

885 Holland, T., & Blundy, J. (1994). Non-ideal interactions in calcic amphiboles and their bearing on
886 amphibole-plagioclase thermometry. *Contributions to Mineralogy and Petrology*, 116(4),
887 433–447.

888 Hunter, N. J. R., Hasalová, P., Weinberg, R. F., & Wilson, C. J. L. (2016). Fabric controls on strain
889 accommodation in naturally deformed mylonites: The influence of interconnected micaceous
890 layers. *Journal of Structural Geology*, 83, 180–193.

891 Hunziker, P. (2003). *The stability of tri-octahedral Fe²⁺-Mg-Al chlorite: A combined*
892 *experimental and theoretical study*. Mineralogisch-Petrographisches Institut der Universität.

893 Janák, M., Froitzheim, N., Vrabec, M., Ravna, E. J. K., & deHoog, C.-J. (2006). Ultrahigh-pressure
894 metamorphism and exhumation of garnet peridotite in Pohorje, Eastern Alps. *Journal of*
895 *Metamorphic Geology*, 24, 19–31.

896 Janák, M., van Roermund, H., Majka, J., & Gee, D. (2013). UHP metamorphism recorded by
897 kyanite-bearing eclogite in the Seve Nappe Complex of northern Jämtland, Swedish
898 Caledonides. *Gondwana Research*, 23(3), 865–879.

899 Jolivet, L., Faccenna, C., Goffé, B., Mattei, M., Rossetti, F., Brunet, C., et al. (1998). Midcrustal
900 shear zones in postorogenic extension: example from the northern Tyrrhenian Sea. *Journal*
901 *of Geophysical Research: Solid Earth*, 103(B6), 12123–12160.

902 Keller, L. M., De Capitani, C., & Abart, R. (2005). A quaternary solution model for white micas
903 based on natural coexisting phengite-paragonite pairs . *Journal of Petrology*, 46.
904 <https://doi.org/doi:10.1093/petrology/egi050>

905 Kilian, R., Heilbronner, R., & Stünitz, H. (2011). Quartz grain size reduction in a granitoid rock
906 and the transition from dislocation to diffusion creep. *Journal of Structural Geology*, 33(8),
907 1265–1284. <https://doi.org/https://doi.org/10.1016/j.jsg.2011.05.004>

908 Kjøll, H. J., Viola, G., Menegon, L., & Sørensen, B. E. (2015). Brittle-viscous deformation of vein
909 quartz under fluid-rich lower greenschist facies conditions. *Solid Earth*, 6(2), 681.

910 Klonowska, I., Janák, M., Majka, J., Froitzheim, N., & Kościńska, K. (2016). Eclogite and garnet
911 pyroxenite from Stor Jougdan, Seve Nappe Complex, Sweden: implications for UHP
912 metamorphism of allochthons in the Scandinavian Caledonides. *Journal of Metamorphic
913 Geology*, 34(2), 103–119.

914 Klonowska, I., Janák, M., Majka, J., Petrik, I., Froitzheim, N., Gee, D. G., & Sasinková, V. (2017).
915 Microdiamond on Åreskutan confirms regional UHP metamorphism in the Seve Nappe
916 Complex of the Scandinavian Caledonides. *Journal of Metamorphic Geology*.

917 Kohn, M. J. (2017). Titanite petrochronology. *Reviews in Mineralogy and Geochemistry*, 83(1),
918 419–441.

919 Kushima, A., Qian, X., Zhao, P., Zhang, S., & Li, J. (2015). Ripplations in van der Waals layers.
920 *Nano Letters*, 15(2), 1302–1308.

921 Ladenberger, A., Be'eri-Shlevin, Y., Claesson, S., Gee, D. G., Majka, J., & Romanova, I. V.
922 (2013). Tectonometamorphic evolution of the Åreskutan Nappe–Caledonian history revealed
923 by SIMS U–Pb zircon geochronology. *Geological Society, London, Special Publications*,
924 390, SP390. 10.

925 Lagoeiro, L., & Barbosa, P. (2010). Nucleation and growth of new grains in recrystallized quartz
926 vein: An example from banded iron formation in Iron Quadrangle, Brazil. *Journal of
927 Structural Geology*, 32(4), 595–604. <https://doi.org/https://doi.org/10.1016/j.jsg.2010.03.007>

928 Lanari, P. (2012). *Micro-cartographie P-T-e dans les roches métamorphiques. Applications aux
929 Alpes et à l'Himalaya. Université de Grenoble. Grenoble.*

930 Lanari, P., & Engi, M. (2017). Local Bulk Composition Effects on Metamorphic Mineral
931 Assemblages. *Reviews in Mineralogy & Geochemistry*, 83, 55–102.
932 <https://doi.org/http://dx.doi.org/10.2138/rmg.2017.83.1>

933 Lanari, P., Guillot, S., Schwartz, S., Vidal, O., Tricart, P., Riel, N., & Beyssac, O. (2012).
934 Diachronous evolution of the alpine continental subduction wedge: evidence from P-T
935 estimates in the Briançonnais Zone houillere (France – Western Alps). *Journal of
936 Geodynamics*, 56–57, 39–54.

937 Lanari, P., Vidal, O., Lewin, E., Dubacq, B., De Andrade, V., & Schwartz, S. (2014). XMapTools
938 a Matlab©-based graphic user interface for microprobe quantified image processing.
939 *Computers and Geosciences*, 62, 227–240. <https://doi.org/10.1016/j.cageo.2013.08.010>

940 Lanari, P., Giuntoli, F., Loury, C., Burn, M., & Engi, M. (2017). An inverse modeling approach to
941 obtain P-T conditions of metamorphic stages involving garnet growth and resorption.
942 *European Journal of Mineralogy*, 29(2), 181–199. [https://doi.org/10.1127/ejm/2017/0029-](https://doi.org/10.1127/ejm/2017/0029-2597)
943 2597

944 Leclère, H., Faulkner, D., Wheeler, J., & Mariani, E. (2016). Permeability control on transient slip
945 weakening during gypsum dehydration: Implications for earthquakes in subduction zones.
946 *Earth and Planetary Science Letters*, 442, 1–12.

947 Lloyd, G. E. (2004). Microstructural evolution in a mylonitic quartz simple shear zone: the
948 significant roles of dauphine twinning and misorientation. *Geological Society, London,*
949 *Special Publications*, 224(1), 39–61.

950 Lorenz, H., Rosberg, J.-E., Juhlin, C., Bjelm, L., Almqvist, B. S. G., Berthet, T., et al. (2015).
951 COSC-1-drilling of a subduction-related allochthon in the Palaeozoic Caledonide orogen of
952 Scandinavia. *Scientific Drilling*, 19, 1.

953 Mäder, U K, & Berman, R. G. (1992). *Amphibole thermobarometry: a thermodynamic approach*.
954 Ottawa: Geological Survey of Canada.

955 Mäder, Urs K, Percival, J. A., & Berman, R. G. (1994). Thermobarometry of garnet–
956 clinopyroxene–hornblende granulites from the Kapuskasing structural zone. *Canadian*
957 *Journal of Earth Sciences*, 31(7), 1134–1145.

958 Majka, J., Be’eri-Shlevin, Y., Gee, D. G., Ladenberger, A., Claesson, S., Konecny, P., &
959 Klonowska, I. (2012). Multiple monazite growth in the Åreskutan migmatite: evidence for a
960 polymetamorphic Late Ordovician to Late Silurian evolution in the Seve Nappe Complex of
961 west-central Jamtland, Sweden. *Journal of Geosciences*, 57(1), 3–23.

962 Majka, J., Rosén, Å., Janák, M., Froitzheim, N., Klonowska, I., Manecki, M., et al. (2014).
963 Microdiamond discovered in the Seve Nappe (Scandinavian Caledonides) and its exhumation
964 by the “vacuum-cleaner” mechanism. *Geology*, 42(12), 1107–1110.

965 Mancktelow, N. S., & Pennacchioni, G. (2005). The control of precursor brittle fracture and fluid–

966 rock interaction on the development of single and paired ductile shear zones. *Journal of*
967 *Structural Geology*, 27(4), 645–661.

968 Mariani, E., Brodie, K. H., & Rutter, E. H. (2006). Experimental deformation of muscovite shear
969 zones at high temperatures under hydrothermal conditions and the strength of phyllosilicate-
970 bearing faults in nature. *Journal of Structural Geology*, 28(9), 1569–1587.

971 Menegon, L., Pennacchioni, G., Heilbronner, R., & Pittarello, L. (2008). Evolution of quartz
972 microstructure and c-axis crystallographic preferred orientation within ductilely deformed
973 granitoids (Arolla unit, Western Alps). *Journal of Structural Geology*, 30(11), 1332–1347.

974 Menegon, L., Piazzolo, S., & Pennacchioni, G. (2011). The effect of Dauphiné twinning on plastic
975 strain in quartz. *Contributions to Mineralogy and Petrology*, 161(4), 635–652.
976 <https://doi.org/10.1007/s00410-010-0554-7>

977 Menegon, L., Stünitz, H., Nasipuri, P., Heilbronner, R., & Svahnberg, H. (2013). Transition from
978 fracturing to viscous flow in granulite facies perthitic feldspar (Lofoten, Norway). *Journal of*
979 *Structural Geology*, 48, 95–112.

980 Merz, L., Almqvist, B. S. G., Grimmer, J. C., & Kontny, A. (2019). Magnetic fabric development
981 in the Lower Seve thrust from the COSC-1 drilling, Swedish Caledonides. *Tectonophysics*,
982 751, 212–228. [https://doi.org/https://doi.org/10.1016/j.tecto.2018.12.018](https://doi.org/10.1016/j.tecto.2018.12.018)

983 Nagel, T., de Capitani, C., & Frey, M. (2002). Isograd and P-T evolution in the eastern Lepontine
984 Alps (Graubünden, Switzerland). *J. Metam. Geol.*, 20, 309–324.

985 Neumann, B. (2000). Texture development of recrystallised quartz polycrystals unravelled by
986 orientation and misorientation characteristics. *Journal of Structural Geology*, 22(11–12),
987 1695–1711.

988 Papapavlou, K., Darling, J. R., Storey, C. D., Lightfoot, P. C., Moser, D. E., & Lasalle, S. (2017).
989 Dating shear zones with plastically deformed titanite: New insights into the orogenic
990 evolution and ore remobilization history of the Sudbury impact structure (Ontario, Canada).
991 *Precambrian Research*, 291, 220–235.

992 Papapavlou, K., Darling, J. R., Lightfoot, P. C., Lasalle, S., Gibson, L., Storey, C. D., & Moser,
993 D. (2018). Polyorogenic reworking of ore-controlling shear zones at the South Range of the
994 Sudbury impact structure: A telltale story from in situ U–Pb titanite geochronology. *Terra*

- 995 *Nova*, 30(3), 254–261. <https://doi.org/10.1111/ter.12332>
- 996 Petřík, I., Janák, M., Klonowska, I., Majka, J., Froitzheim, N., Yoshida, K., et al. (2019). Monazite
 997 behaviour during metamorphic evolution of a diamond-bearing gneiss: a case study from the
 998 Seve Nappe Complex, Scandinavian Caledonides. *Journal of Petrology*, 60(9), 1773–1796.
- 999 Prior, D. J., Boyle, A. P., Brenker, F., Cheadle, M. C., Day, A., Lopez, G., et al. (1999). The
 1000 application of electron backscatter diffraction and orientation contrast imaging in the SEM to
 1001 textural problems in rocks. *American Mineralogist*, 84(11–12), 1741–1759.
- 1002 Prior, D. J., Wheeler, J., Peruzzo, L., Spiess, R., & Storey, C. (2002). Some garnet microstructures:
 1003 an illustration of the potential of orientation maps and misorientation analysis in
 1004 microstructural studies. *Journal of Structural Geology*, 24(6), 999–1011.
- 1005 Prior, D. J., Mariani, E., & Wheeler, J. (2009). EBSD in the earth sciences: applications, common
 1006 practice, and challenges. In *Electron backscatter diffraction in materials science* (pp. 345–
 1007 360). Springer.
- 1008 Putnis, A. (2015). Transient porosity resulting from fluid–mineral interaction and its
 1009 consequences. *Reviews in Mineralogy and Geochemistry*, 80, 1–23.
- 1010 Putnis, A., & Putnis, C. V. (2007). The mechanism of reequilibration of solids in the presence of
 1011 a fluid phase. *Journal of Solid State Chemistry*, 180(5), 1783–1786.
- 1012 Rice, A. H. N., & Anderson, M. W. (2016). Restoration of the external Scandinavian Caledonides.
 1013 *Geological Magazine*, 1–30.
- 1014 Roberts, D. (2003). The Scandinavian Caledonides: event chronology, palaeogeographic settings
 1015 and likely modern analogues. *Tectonophysics*, 365(1), 283–299.
- 1016 Roberts, D., & Gee, D. G. (1985). An introduction to the structure of the Scandinavian
 1017 Caledonides. *The Caledonide Orogen–Scandinavia and Related Areas*, 1, 55–68.
- 1018 Van Roermund, H. L. M. (1985). Eclogites of the Seve nappe, central Scandinavian Caledonides.
 1019 *The Caledonide Orogen—Scandinavia and Related Areas*, 873–886.
- 1020 Van Roermund, H. L. M. (1989). High-pressure ultramafic rocks from the allochthonous nappes
 1021 of the Swedish Caledonides. *The Caledonide Geology of Scandinavia*, 205–219.
- 1022 Root, D., & Corfu, F. (2012). U–Pb geochronology of two discrete Ordovician high-pressure

1023 metamorphic events in the Seve Nappe Complex, Scandinavian Caledonides. *Contributions*
 1024 *to Mineralogy and Petrology*, 163(5), 769–788.

1025 Schmid, S. M., & Casey, M. (1986). Complete fabric analysis of some commonly observed quartz
 1026 c-axis patterns. *Mineral and Rock Deformation*, 263–286.

1027 Searle, M. P., Law, R. D., Godin, L., Larson, K. P., Streule, M. J., Cottle, J. M., & Jessup, M. J.
 1028 (2008). Defining the Himalayan main central thrust in Nepal. *Journal of the Geological*
 1029 *Society*, 165(2), 523–534.

1030 Shea, W. T., & Kronenberg, A. K. (1993). Strength and anisotropy of foliated rocks with varied
 1031 mica contents. *Journal of Structural Geology*, 15(9–10), 1097–1121.

1032 Sjöström, H. (1983). The Seve—Köli Nappe Complex of the Handöl—Storlien—Essandsjøen
 1033 area, Scandinavian Caledonides. *Geologiska Föreningen i Stockholm Förhandlingar*, 105(2),
 1034 93–117.

1035 Song, W. J., & Ree, J.-H. (2007). Effect of mica on the grain size of dynamically recrystallized
 1036 quartz in a quartz–muscovite mylonite. *Journal of Structural Geology*, 29(12), 1872–1881.
 1037 <https://doi.org/https://doi.org/10.1016/j.jsg.2007.09.011>

1038 Spandler, C., Hammerli, J., Sha, P., Hilbert-Wolf, H., Hu, Y., Roberts, E., & Schmitz, M. (2016).
 1039 MKED1: A new titanite standard for in situ analysis of Sm–Nd isotopes and U–Pb
 1040 geochronology. *Chemical Geology*, 425, 110–126.
 1041 <https://doi.org/https://doi.org/10.1016/j.chemgeo.2016.01.002>

1042 Spear, F. S., Kohn, M. J., & Cheney, J. T. (1999). P–T paths from anatectic pelites. *Contributions*
 1043 *to Mineralogy and Petrology*, 134(1), 17–32.

1044 Spencer, K. J., Hacker, B. R., Kylander-Clark, A. R. C., Andersen, T. B., Cottle, J. M., Stearns,
 1045 M. A., et al. (2013). Campaign-style titanite U–Pb dating by laser-ablation ICP: Implications
 1046 for crustal flow, phase transformations and titanite closure. *Chemical Geology*, 341, 84–101.

1047 Stephens, M. B. (1988). The Scandinavian Caledonides: a complexity of collisions. *Geology*
 1048 *Today*, 4(1), 20–26.

1049 Stipp, M., & Tullis, J. (2003). The recrystallized grain size piezometer for quartz. *Geophysical*
 1050 *Research Letters*, 30(21).

- 1051 Stipp, M., Stünitz, H., Heilbronner, R., & Schmid, S. M. (2002). Dynamic recrystallization of
1052 quartz: correlation between natural and experimental conditions. *Geological Society, London,*
1053 *Special Publications*, 200(1), 171–190.
- 1054 Strömberg, A., Karis, L., Zachrisson, E., Sjöstrand, T., Skoglund, R., Lundegårdh, P. H., et al.
1055 (1984). Berggrundskarta över Jämtlands län utom förutvarande Fjällsjö kommun, scale 1: 200
1056 000. *Geological Survey of Sweden, Ca*, 53.
- 1057 Stünitz, H., & Gerald, J. D. F. (1993). Deformation of granitoids at low metamorphic grade. II:
1058 Granular flow in albite-rich mylonites. *Tectonophysics*, 221(3–4), 299–324.
- 1059 Trepmann, C. A., Stöckhert, B., Dorner, D., Moghadam, R. H., Küster, M., & Röller, K. (2007).
1060 Simulating coseismic deformation of quartz in the middle crust and fabric evolution during
1061 postseismic stress relaxation—an experimental study. *Tectonophysics*, 442(1–4), 83–104.
- 1062 Vermeesch, P. (2018). IsoplotR: A free and open toolbox for geochronology. *Geoscience*
1063 *Frontiers*, 9(5), 1479–1493. <https://doi.org/https://doi.org/10.1016/j.gsf.2018.04.001>
- 1064 Vidal, O., Parra, T., & Vieillard, P. (2005). Thermodynamic properties of the Tschermak solid
1065 solution in Fe-chlorite: Application to natural examples and possible role of oxidation.
1066 *American Mineralogist*, 90(2–3), 347–358.
- 1067 Vidal, O., De Andrade, V., Lewin, E., Munoz, M., Parra, T., & Pascarelli, S. (2006). P–T-
1068 deformation-Fe³⁺/Fe²⁺ mapping at the thin section scale and comparison with XANES
1069 mapping: application to a garnet-bearing metapelite from the Sambagawa metamorphic belt
1070 (Japan). *Journal of Metamorphic Geology*, 24(7), 669–683.
- 1071 Viegas, G., Menegon, L., & Archanjo, C. (2016). Brittle grain-size reduction of feldspar, phase
1072 mixing and strain localization in granitoids at mid-crustal conditions (Pernambuco shear
1073 zone, NE Brazil). *Solid Earth*, 7(2), 375–396.
- 1074 Walters, J. B., & Kohn, M. J. (2017). Protracted thrusting followed by late rapid cooling of the
1075 Greater Himalayan Sequence, Annapurna Himalaya, Central Nepal: Insights from titanite
1076 petrochronology. *Journal of Metamorphic Geology*, 35(8), 897–917.
- 1077 Wassmann, S., & Stöckhert, B. (2013). Rheology of the plate interface—dissolution precipitation
1078 creep in high pressure metamorphic rocks. *Tectonophysics*, 608, 1–29.

1079 Wenning, Q. C., Berthet, T., Ask, M., Zappone, A., Rosberg, J., & Almqvist, B. S. G. (2017).
1080 Image log analysis of in situ stress orientation, breakout growth, and natural geologic
1081 structures to 2.5 km depth in central Scandinavian Caledonides: Results from the COSC-1
1082 borehole. *Journal of Geophysical Research: Solid Earth*.

1083 Wheeler, J., Prior, D., Jiang, Z., Spiess, R., & Trimby, P. (2001). The petrological significance of
1084 misorientations between grains. *Contributions to Mineralogy and Petrology*, 141(1), 109–
1085 124.

1086 Wintsch, R. P., Christoffersen, R., & Kronenberg, A. K. (1995). Fluid-rock reaction weakening of
1087 fault zones. *Journal of Geophysical Research: Solid Earth*, 100(B7), 13021–13032.

1088 Wright, S. I., Nowell, M. M., & Field, D. P. (2011). A Review of Strain Analysis Using Electron
1089 Backscatter Diffraction. *Microscopy and Microanalysis*, 17(3), 316–329. [https://doi.org/DOI:](https://doi.org/DOI:10.1017/S1431927611000055)
1090 10.1017/S1431927611000055

1091 Zachrisson, E., & Sjöstrand, T. (1990). Bedrock Map 22E Frostviken. *Sveriges Geologiska*
1092 *Undersökning (SGU) Ai 44, Scale 1: 50,000*.

1093 Zwart, H. J. (1975). Structure and metamorphism in the Seve-Köli Nappe Complex (Scandinavian
1094 Caledonides) and its implications concerning the formation of metamorphic nappes. *Annales*
1095 *de La Société Géologique de Belgique*, 129–144.

1096

1097

1098 **Figure 1.** Geological setting of the Scandinavian Caledonides. (a) Tectonic map with inferred
1099 paleogeography of the nappes (modified after Gee et al., 2010). WGR: Western Gneiss Region.
1100 (b) Cross section marked in (a) with vertical exaggeration of 5 x and approximate location of the
1101 COSC-1 borehole (modified after Gee et al., 2010). (c) Detail of the study area with location of
1102 the COSC-1 drilling site (modified after Strömberg et al., 1984).

1103

1104 **Figure 2.** Location of the studied samples along the drill core and summary of the P-T-t data for
1105 the Lower Seve Nappe (this study, see text for details and discussion). The inferred contact with
1106 the underlying Särvi Nappe is marked by the dashed line. Depth values are referred to metres from
1107 the surface.

1108

1109 **Figure 3.** Thin section scans of micaschist samples (plane-polarized light). In the microstructural
1110 sketches and in the following figures the red lines indicate the mylonitic S fabric of epidote
1111 amphibolite facies conditions, the green and light blue lines indicate the C-type and C'-type shear
1112 bands and the arrows the sense of shear. (a-c) Sample 561, 640 and 695, respectively. The black
1113 rectangles indicate the location of the following figures.

1114

1115 **Figure 4.** (a-f) Main mylonitic foliation of epidote amphibolite facies condition (red lines)
1116 overprinted by C and C'-type shear bands of greenschist facies conditions (green and light blue
1117 lines, respectively) in garnet micaschists. (a-b) Quartz monomineralic layer displays a decrease in
1118 grain size in correspondence of the C' band, with a dextral sense of shear; plane and crossed-
1119 polarized light photo, respectively (micaschist sample 640). (c) S structure overprinted by C and
1120 C' planes indicating a dextral sense of shear, plane-polarized light photo (micaschist sample 695).
1121 The black rectangle indicates the location of the enlargement on C-type shear bands of Figure 11.
1122 (d) X-ray map showing the mineral phases. (e-f) Detail of the C planes with location of the EBSD
1123 map of Figure 15 (red square; plane and crossed-polarized light photo, respectively). (g-h) CL
1124 images highlighting plagioclase microstructures of micaschist sample 695. The porphyroclastic

core is dark and displays a network of fractures few μm thick and up to several hundreds of μm long, sealed by a plagioclase that has the same brightness as the syn-kinematic rim. The asymmetry of the rims is consistent with a dextral sense of shear. In (g) both core and rim are cut by the C shear band.

Figure 5. Thin section scans of amphibolite samples 531 and 543, respectively (plane-polarized light). The mylonitic S foliation wraps around plagioclase porphyrocrysts highlighting a dextral sense of shear.

Figure 6. Microstructure and chemical data of amphibolite sample 531. The photos and maps were rotated of 90° counterclockwise from the original orientation of the sample in the drill core for acquisition and graphic purposes (see original orientation in Figure 5a). (a) Optical photo showing the pressure shadow between two plagioclase porphyrocrysts. Amphibole has a less pleochroic core (light brown) and a more pleochroic rim (dark green), plane-polarized light. The white square indicates the location of the EBSD map (Figure 8). (b) CL image of bright plagioclase porphyroclastic core with darker fractures and syn-kinematic rims; compare with (e). (c) BSE image with bright ilmenite rimmed by titanite (arrows). (d-i) Standardized X-ray maps. (d) Map of the mineral phases. (e) Plagioclase X_{Ab} map displays low X_{Ab} porphyroclastic cores and high X_{Ab} syn-kinematic rims. Note that the fractures in the core are sealed by a plagioclase richer in albite content and similar to the rim composition. (f) Amphibole X_{Mg} map highlighting a richer X_{Mg} relic core and a poorer syn-kinematic rim. (g-i) Titanite oxide weight percentages of TiO_2 , CaO , SiO_2 , respectively.

Figure 7. Microstructure and chemical data of amphibolite sample 543. (a) Optical photo, plane-polarized light. The red rectangle indicates the location of X-ray maps c-e. (b) CL image of bright plagioclase relic cores and darker syn-kinematic rims; compare with (d). (c-e) Standardized X-ray maps. (c) Map of the mineral phases. (d) Plagioclase X_{Ab} map displays low X_{Ab} relic cores and high X_{Ab} syn-kinematic rims. (e) Amphibole X_{Mg} map highlighting a richer X_{Mg} relic core and a poorer syn-kinematic rim. (f) Titanite rimming ilmenite lengthened as the main foliation; optical

photo, plane-polarized light. (g-h) BSE images highlighting bright ilmenite, with lobate edges, surrounded by darker titanite grains. Note the laser ablation pits.

Figure 8. Microstructural characterization of titanite grains in amphibolite sample 531. (a) Detail of Figure 6 displaying ilmenite boudinated with titanite growing in the boudin necks. (b) Titanite grains intergrown with amphibole and plagioclase lengthened as the mylonitic main foliation. Optical photos, plane-polarized light. (c) EBSD phase map. Note the ilmenite rimmed by titanite. White lines indicate low-angle boundaries ($2\text{-}10^\circ$), black lines high-angle boundaries ($> 10^\circ$) and light blue lines twin boundaries in ilmenite (180° rotation about an axis parallel to $[100]$ axis). (d) Titanite GOS map, suggesting that it has very low internal strain. (e) and (g) Titanite texture component maps and BSE images (f) and (h). (i) Titanite pole figures of map (c). Contouring is 1.

Figure 9. Microstructure and chemical data of micaschist sample 561. (a-b) Optical photo, plane- and crossed-polarized light, respectively. (c) BSE image. (d-n) Standardized X-ray maps. (d) Map of the mineral phases showing the main foliation defined by muscovite, biotite, staurolite and plagioclase. (e) Muscovite Si apfu map highlights relic phengitic cores (high in Si apfu) and syn-kinematic rims. (f) Plagioclase X_{Ab} map displays complex growth zones, with low X_{Ab} cores and high X_{Ab} rims. (g) Biotite X_{Mg} map. (h) Staurolite X_{Mg} map. (i-n) Garnet X_{Grs} , X_{Sps} , X_{Prp} , X_{Alm} maps, respectively, display a concentric zoning except for the X_{Prp} that is more homogeneous.

Figure 10. Microstructure and chemical data of micaschist sample 640. (a-b) Optical photo highlighting the amphibolite facies main foliation overprinted by C' shear bands with a dextral sense of shear, plane-polarized and crossed-polarized light, respectively. (c) BSE image. (d-n) Standardized X-ray maps. (d) Map of the mineral phases showing the main foliation defined by muscovite and biotite with a sigmoidal shape. C' shear bands are defined by chlorite and minor muscovite. (e) Muscovite Si apfu map highlights relic phengitic cores (high in Si apfu) and syn-amphibolite facies foliation rims. (f) Plagioclase X_{Ab} map. (g) Chlorite X_{Mg} map; note its preferential location along the C' shear bands. (h) Biotite X_{Mg} map. (i-n) Garnet X_{Grs} , X_{Sps} , X_{Prp} ,

X_{Alm} maps, respectively, display a concentric zoning except for the X_{Prp} and X_{Alm} that are more homogeneous.

Figure 11. Microstructure and chemical data of micaschist sample 695. (a) Optical photo, crossed-polarized light. (b) BSE image highlighting the main foliation with a dextral sense of shear. (c-i) Standardized X-ray maps. (c) Muscovite Si apfu map highlights relic phengitic cores (high in Si apfu) and syn-kinematic rims. (d) Plagioclase X_{Ab} map displays high X_{Ab} cores and lower X_{Ab} syn-kinematic rims. (e) Biotite X_{Mg} map. (f-i) Garnet X_{Grs} , X_{Sps} , X_{Prp} , X_{Alm} maps, respectively, display a concentric zoning except for the X_{Grs} that is more homogeneous. (l) BSE image of C-type shear bands defined mainly by chlorite and minor muscovite. (m-p) Standardized X-ray maps. (m) Map of the mineral phases. (n) Muscovite Si apfu map. (o) Plagioclase X_{Ab} map. (p) Chlorite X_{Mg} map.

Figure 12. (a-c) Equilibrium phase diagrams of the micaschists samples computed with Theriak–Domino (de Capitani & Petrakakis, 2010) with plotted chlorite and white mica multi-equilibrium results. The error bars departing from filled ellipses show the P–T uncertainties related to the analytical error of the garnet compositions. Red dashed ellipses indicate the P-T conditions of the metamorphic stages best fitting with the observed paragenesis and the computed isopleths. Red dashed rectangles indicate the Chlorite + white mica + quartz + H_2O thermobarometry results. Purple dashed lines represent the inferred P-T paths for each specific sample. See text for discussion.

Figure 13. (a-b) Chlorite + white mica + quartz + H_2O thermobarometry results; the red ellipses represent the P-T uncertainties. (c) P-T summary path of the studied samples with highlighted the three metamorphic stages described in the text (M_{HP} , M_{Amp} , M_{Gr}).

1207

1208 **Figure 14.** EBSD data of the C' shear band domain in the micaschist sample 640. (a) EBSD phase
1209 map. Note the fine-grained chlorite and muscovite growing along the C' planes. White lines
1210 indicate low-angle boundaries ($2-10^\circ$), black lines high-angle boundaries ($> 10^\circ$) and light blue
1211 lines Dauphiné twin boundaries in quartz. (b) Quartz GOS map highlights grains with low GOS
1212 values at the boundaries of grains with higher GOS values. (c) Quartz grain size map. (d)
1213 Misorientation angle distribution of quartz displaying peaks at low angle misorientations and at
1214 60° for correlated pairs. (e) Quartz pole figures of crystallographic axes, and plot of misorientation
1215 axis in crystal coordinates associated with low-angle misorientation ($2-10^\circ$) in quartz. Pole figures
1216 plotted on the lower hemisphere of the stereographic projection. n=number of grains (one-point-
1217 per-grain). Half width 10° and cluster size 5° , maximum value is given. Quartz grains display a
1218 CPO of the c-axis forming a short girdle at 45° of the YZ plane.

1219

1220 **Figure 15.** Domain with C-type shear bands deforming the mylonitic foliation of micaschist 695
1221 investigated by EBSD. (a-b) BSE image and EBSD phase map highlighting the phyllosilicates
1222 crystallizing along the C planes. Note the fine-grained chlorite and muscovite growing along the
1223 C planes. The bigger grains of such minerals are re-oriented parallel to the C planes. (c) Quartz
1224 GOS map highlights that smaller grains have very low internal strain. (d) Quartz grain size map
1225 displays grain size reduction in proximity of the C planes. The arrows indicate subgrains forming
1226 in the bigger grains (see text). Subsets 1 to 4 are highlighted with the dashed lines.

1227

1228 **Figure 16.** Misorientation angle distribution of quartz, pole figures of the crystallographic axes,
1229 and plots of misorientation axis in crystal coordinates for the area of micaschist sample 695 shown
1230 in figure 15. (a-d) Data for quartz from subset 1, 2, 3 and 4, respectively, defined in Figure 15d.
1231 All subsets show peaks at low angle misorientations and at 60° for both correlated and uncorrelated
1232 pairs. Subsets 1 and 2 display CPO and a maximum around $\langle c \rangle$ in the plot of misorientation axis
1233 in crystal coordinates. These features are not present in subsets 3 and 4.

1234

1235

1236 **Figure 17.** Results of in-situ LA-ICP-MS U-Pb age dating of synkinematic titanite grains in the
1237 amphibolites. The results are plotted on Terra Wasserburg concordia diagrams with lower intercept
1238 dates.

1239

1240 **Figure 18.** P-T-t-d summary path of the studied samples with highlighted the three metamorphic
1241 stages described in the text and the deformation mechanisms. The star indicates the youngest age
1242 constraint for the C and C’ type shear bands from Andersen (1998) and Fossen (2000; see text for
1243 further details).

1244

Amp-Pl couples	Thermometer	Barometer	
	HB	BB	AS
531AmpRim-PIRim	610 °C	0.77 GPa	0.87 GPa
543AmpRim-PIRim	651 °C	0.40 GPa	0.84 GPa

1245 **Table 1.** Results of amphibole–plagioclase geothermobarometry Thermometer abbreviation: HB:
1246 Holland and Blundy (1994). Barometer abbreviations: BB: Bhadra and Bhattacharya (2007); AS:
1247 Anderson and Smith (1995). The favoured results are highlighted in bold (see discussion section
1248 for details).

	Grt						Ph-Ms									Bt			St
Sample	561		640A		695		561		640A			695			561	640A	695	561	
Average composition (wt%)	CORE	RIM	CORE	RIM	CORE	RIM	CORE	RIM	CORE	RIM	C' planes	CORE	RIM	C' planes					
SiO ₂	36.23	36.80	36.97	37.09	36.96	36.94	49.17	47.22	50.24	46.16	46.02	51.56	48.16	47.15	36.39	36.58	35.27	28.96	
TiO ₂	0.07	0.07	0.05	0.05	0.11	0.11	0.42	0.47	0.30	0.35	0.30	0.24	0.32	0.39	1.61	2.12	1.80	0.49	
Al ₂ O ₃	21.06	21.33	20.79	20.86	21.20	21.17	32.43	35.20	28.72	31.05	31.93	28.86	33.34	31.33	18.10	17.89	17.22	53.36	
FeO	29.44	31.28	30.80	31.12	28.44	29.26	2.27	1.98	2.84	2.88	2.67	3.93	3.02	4.25	17.09	20.62	24.51	12.54	
MnO	6.85	4.51	3.06	2.56	6.42	5.56	0.01	0.01	0.02	0.02	0.01	0.01	0.01	0.01	0.05	0.01	0.10	0.26	
MgO	3.38	3.27	1.75	1.72	1.09	1.22	1.50	0.73	2.09	1.20	0.96	2.38	1.13	1.64	12.14	8.81	7.72	1.91	
CaO	2.06	3.17	6.31	6.60	6.27	6.28	0.01	0.01	0.03	0.03	0.03	0.01	0.01	0.01	0.01	0.01	0.06	0.01	
Na ₂ O	-	-	-	-	-	-	1.61	2.17	0.75	1.07	1.27	0.65	1.12	0.56	0.39	0.20	0.09	0.04	
K ₂ O	-	-	-	-	-	-	9.21	8.56	10.05	9.91	9.63	10.09	9.77	10.43	9.33	9.56	8.92	0.00	
Total	99.08	100.42	99.72	100.00	100.48	100.53	96.63	96.35	95.04	92.66	92.82	97.72	96.87	95.77	95.09	95.80	95.68	97.56	
Formulae based on 12 O							on 11 O											on 23 O	
Si	2.93	2.94	2.98	2.98	2.97	2.98	3.22	3.10	3.36	3.19	3.16	3.37	3.17	3.17	2.74	2.78	2.74	4.00	
Ti	0.00	0.00	0.00	0.00	0.01	0.01	0.02	0.02	0.01	0.02	0.02	0.01	0.02	0.02	0.09	0.12	0.10	0.05	
Al	2.01	2.01	1.98	1.98	2.01	2.01	2.50	2.72	2.26	2.53	2.59	2.22	2.58	2.48	1.61	1.60	1.58	8.68	
Fe	2.00	2.09	2.08	2.09	1.91	1.97	0.12	0.11	0.16	0.17	0.15	0.21	0.17	0.24	1.08	1.31	1.59	1.45	
Mn	0.47	0.30	0.21	0.17	0.44	0.35	0.00	0.00	0.00	0.00	0.00	0.00	0.00	0.00	0.00	0.00	0.01	0.03	
Mg	0.41	0.39	0.21	0.21	0.13	0.15	0.15	0.07	0.21	0.12	0.10	0.23	0.11	0.16	1.36	1.00	0.89	0.39	
Ca	0.18	0.27	0.54	0.57	0.54	0.54	0.00	0.00	0.00	0.00	0.00	0.00	0.00	0.00	0.00	0.00	0.00	0.00	
Na	-	-	-	-	-	-	0.20	0.28	0.10	0.14	0.17	0.08	0.14	0.07	0.06	0.03	0.01	0.01	
K	-	-	-	-	-	-	0.77	0.72	0.86	0.87	0.84	0.84	0.82	0.90	0.90	0.93	0.88	0.00	
Σ cations	8.01	8.00	8.00	8.00	8.00	8.00	6.99	7.02	6.97	7.04	7.03	6.97	7.01	7.05	7.84	7.77	7.82	14.61	
X _{Mg}	-	-	-	-	-	-	0.54	0.40	0.57	0.43	0.39	0.52	0.40	0.41	0.56	0.43	0.36	0.21	
Molecular proportions of garnet end members																			
Alm	0.65	0.68	0.68	0.69	0.63	0.65													
Prp	0.13	0.13	0.07	0.07	0.04	0.05													
Grs	0.06	0.09	0.18	0.19	0.18	0.18													
Sps	0.15	0.10	0.07	0.06	0.15	0.13													

1249 **Table 2.** Representative average composition analysis (wt%) of garnet, muscovite, biotite and staurolite.
1250

Sample	Pl										Amp				Chl	
	561		640A		695		531		543		531		543		640A	695
	CORE	RIM	CORE	RIM	CORE	RIM	CORE	RIM	CORE	RIM	CORE	RIM	CORE	RIM	Spot analysis	
Average composition (wt%)																
SiO ₂	62.56	64.01	63.73	67.03	69.11	66.28	59.69	62.23	59.68	62.25	52.55	44.55	47.73	42.54	25.19	24.44
TiO ₂	0.01	0.01	0.02	0.02	0.01	0.01	0.02	0.02	0.02	0.02	0.28	0.35	0.50	0.38	0.13	0.21
Al ₂ O ₃	25.28	24.05	22.48	19.68	20.28	22.74	25.75	24.07	25.06	23.33	4.40	13.52	9.57	13.39	21.01	20.95
FeO	0.06	0.06	0.06	0.04	0.05	0.06	0.07	0.10	0.11	0.14	12.56	15.55	13.49	15.94	25.73	30.95
MnO	0.01	0.01	0.01	0.01	0.03	0.03	0.02	0.02	0.01	0.01	0.22	0.22	0.23	0.25	0.06	0.21
MgO	0.00	0.00	0.00	0.00	0.00	0.00	0.01	0.01	0.01	0.01	15.42	10.25	12.62	10.49	12.84	11.35
CaO	5.47	4.06	3.95	0.17	0.01	0.10	7.02	4.10	6.67	4.33	12.07	11.82	11.40	11.70	0.01	0.00
Na ₂ O	9.22	10.09	9.75	12.06	13.09	11.19	8.02	9.74	8.49	9.92	0.70	1.77	1.67	2.15	0.01	0.00
K ₂ O	0.05	0.04	0.09	0.08	0.06	0.18	0.06	0.05	0.04	0.04	0.11	0.30	0.21	0.31	0.55	0.06
Sum	102.64	102.33	100.08	99.09	102.63	100.60	100.65	100.32	100.09	100.04	98.32	98.34	97.43	97.16	85.52	88.17
	Formulae based on 8 O										on 23 anhydrous O				on 14 anhydrous O	
Si	2.71	2.77	2.82	2.97	2.96	2.88	2.65	2.75	2.66	2.76	7.48	6.49	6.92	6.31	2.72	2.65
Ti	-	-	-	-	-	-	-	-	-	-	0.03	0.04	0.05	0.04	-	-
Al	1.29	1.23	1.17	1.03	1.02	1.17	1.35	1.25	1.32	1.22	0.74	2.32	1.64	2.34	2.69	2.67
Fe ³⁺	-	-	-	-	-	-	-	-	-	-	0.25	0.36	0.36	0.55	0.06	0.00
Fe ²⁺	-	-	-	-	-	-	-	-	-	-	1.20	1.53	1.28	1.42	2.27	2.80
Mn	-	-	-	-	-	-	-	-	-	-	0.03	0.03	0.03	0.03	-	-
Mg	-	-	-	-	-	-	-	-	-	-	3.27	2.23	2.73	2.32	2.07	1.83
Ca	0.25	0.19	0.19	0.01	0.00	0.01	0.33	0.19	0.32	0.21	1.84	1.85	1.77	1.86	-	-
Na	0.77	0.85	0.84	1.03	1.09	0.94	0.69	0.83	0.74	0.85	0.20	0.51	0.47	0.63	-	-
K	0.05	0.00	0.01	0.00	0.00	0.02	0.00	0.00	0.00	0.00	0.02	0.06	0.04	0.06	-	-
Sum	5.08	5.04	5.01	5.04	5.07	5.01	5.02	5.04	5.04	5.05	15.06	15.41	15.28	15.54	9.81	9.95
X _{Mg}	-	-	-	-	-	-	-	-	-	-	0.69	0.54	0.63	0.54	0.47	0.40
X _{Ab}	0.75	0.82	0.81	0.99	1.00	0.98	0.67	0.81	0.70	0.80	-	-	-	-	-	-
X _{An}	0.25	0.18	0.18	0.01	0.00	0.01	0.33	0.19	0.30	0.19	-	-	-	-	-	-

1251 **Table 3.** Representative average composition and spot analysis (wt%) of plagioclase, amphibole and chlorite.

1252

1253

1254

Figure 1.

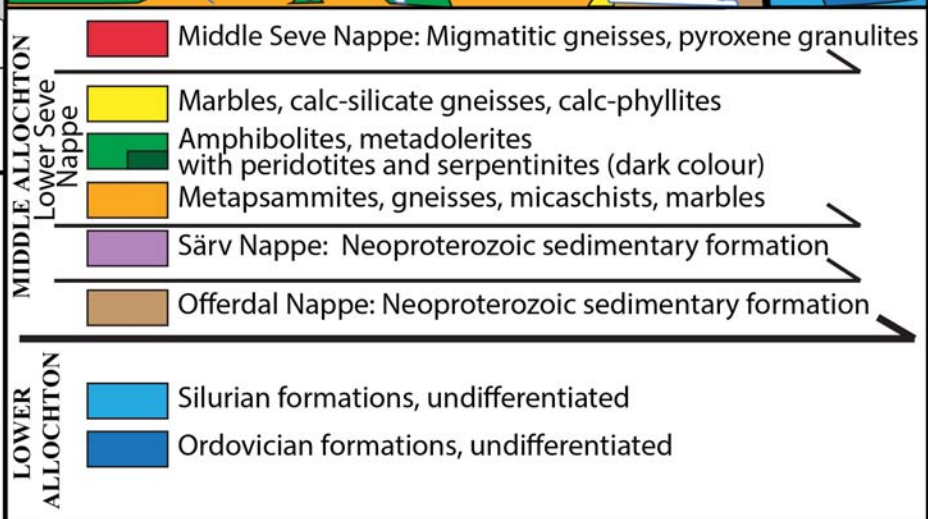
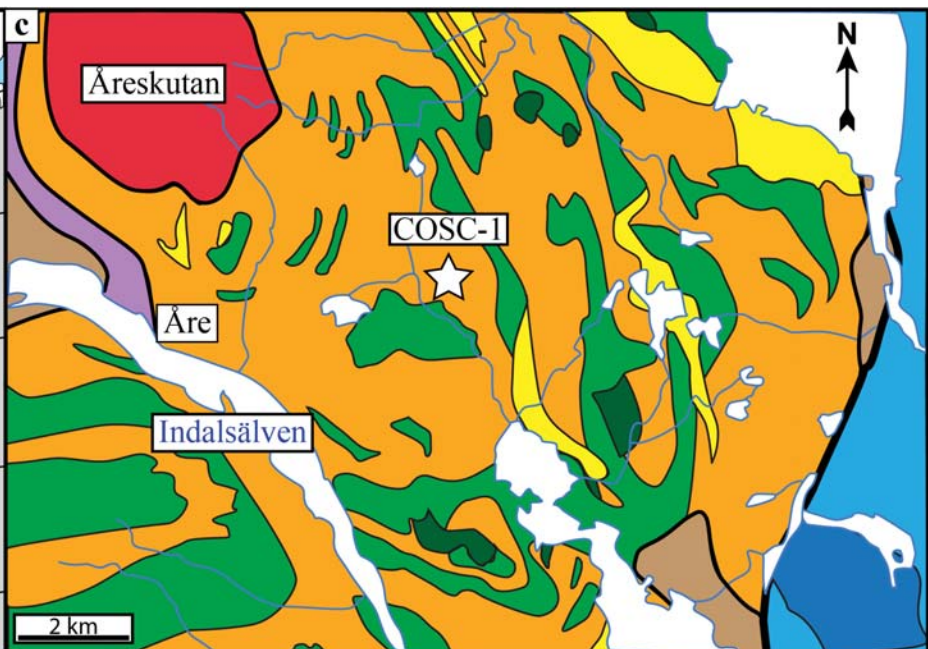
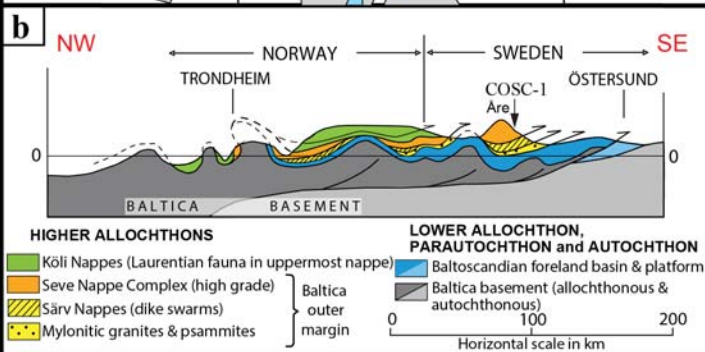
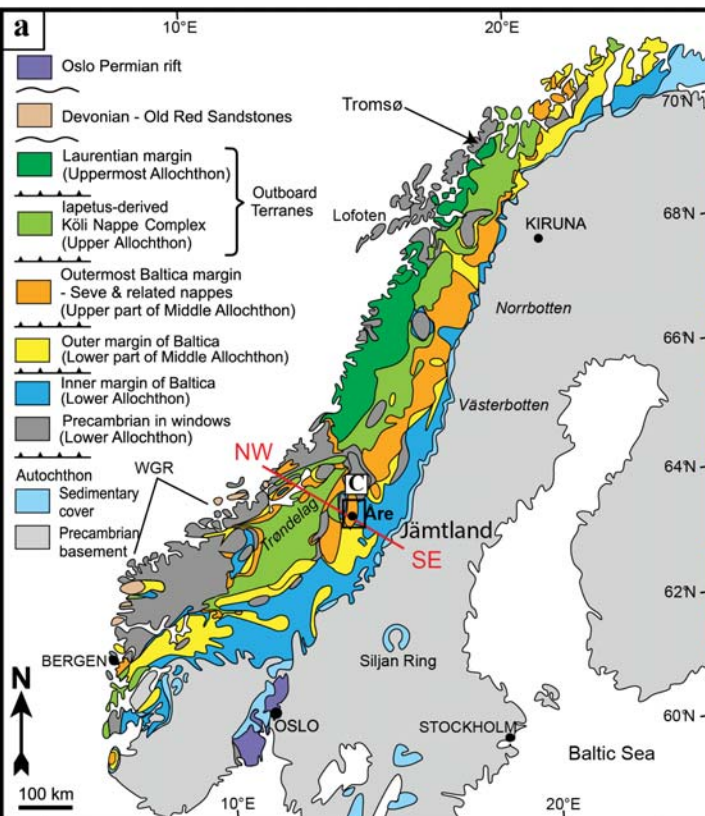


Figure 2.

Lower Seve Nappe

Minor mylonites occur

Increasing deformation:
mylonitic fabrics dominate



1000 m

531 Amphibolite



P-T-t: Amp-Plag ~600°C–0.8GPa
@ 429±20 Ma

543 Amphibolite
with opaque bands



P-T-t: Amp-Plag ~650°C–0.8GPa
@ 417±9 Ma

1500 m

557 Amphibolite



t: Foliation @ 461 ± 21 Ma

561 Micaschist with
garnet and staurolite



P-T: Foliation ~500°C–0.55GPa

2000 m

640 Micaschist
with garnet



P-T: Foliation~520°C–0.6GPa
Wm-Chl C' planes: ~300°C–0.3GPa

648 Amphibolite



P-T: Amp-Plag ~600°C–0.8–1GPa
Chl C' planes: 350–200°C
(Giuntoli, Menegon, et al., 2018)

2500 m

695 Micaschist
with garnet



P-T: Grt, Wm core, Ab core ~500°C–1.1–1.3GPa
Foliation ~500°C–0.6GPa
Wm-Chl C planes: ~370°C–0.3GPa

Särv Nappe

Figure 3.

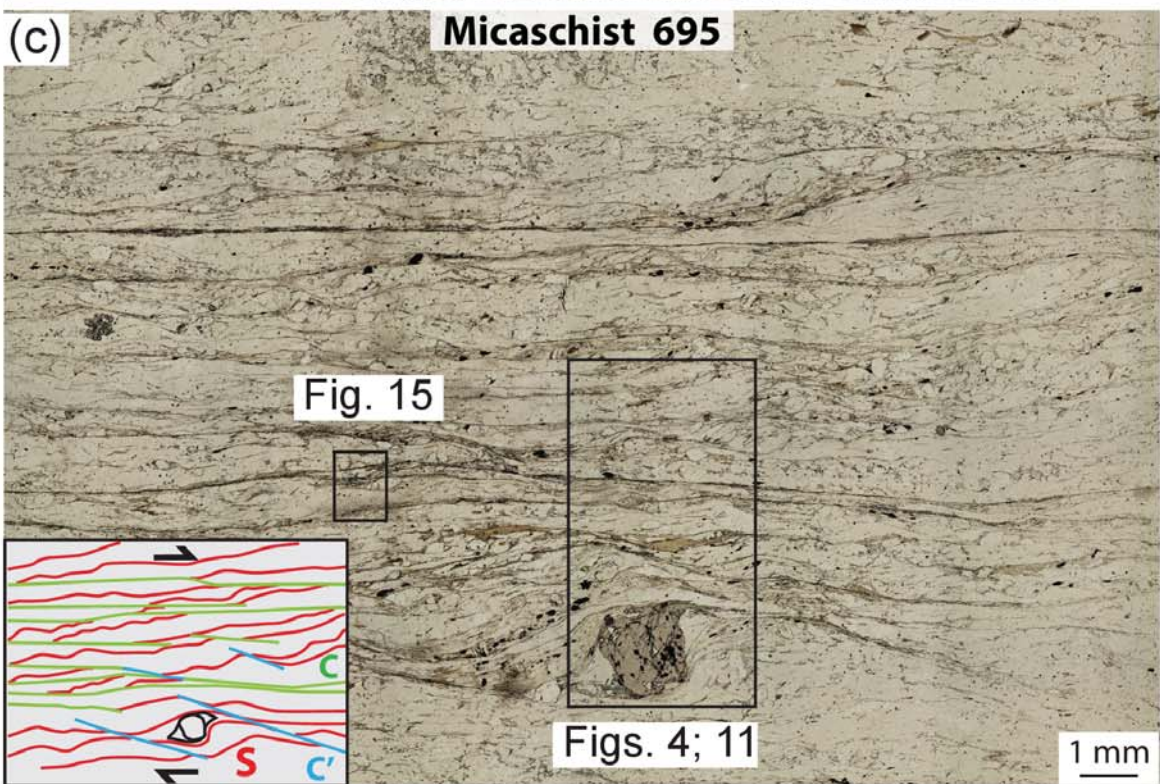
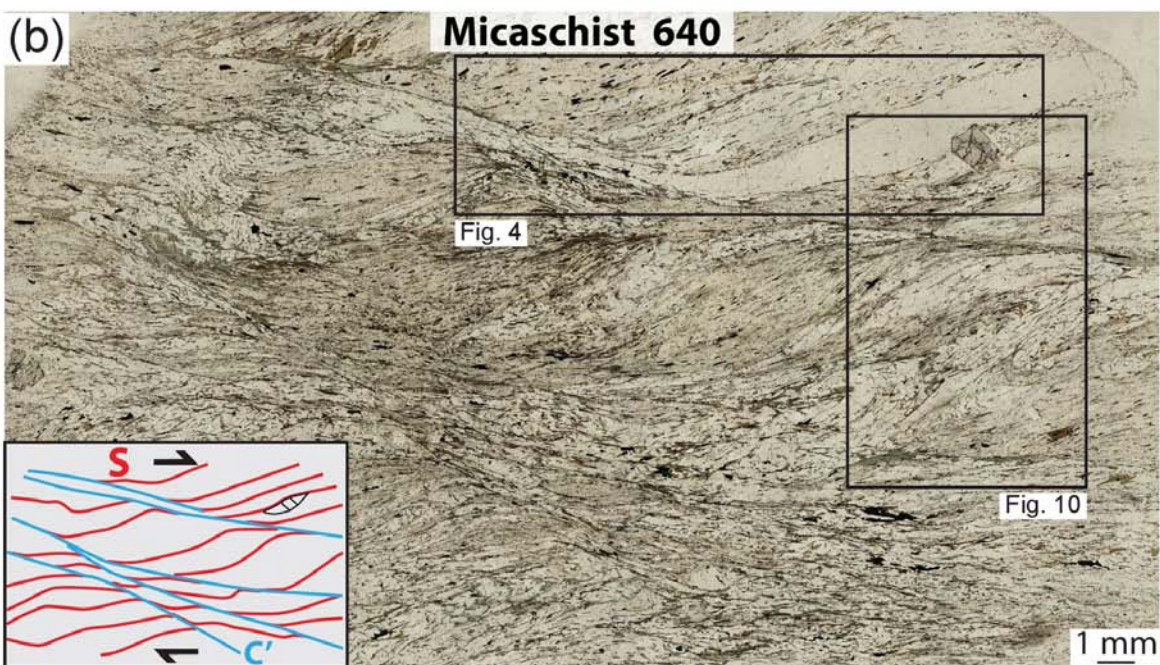
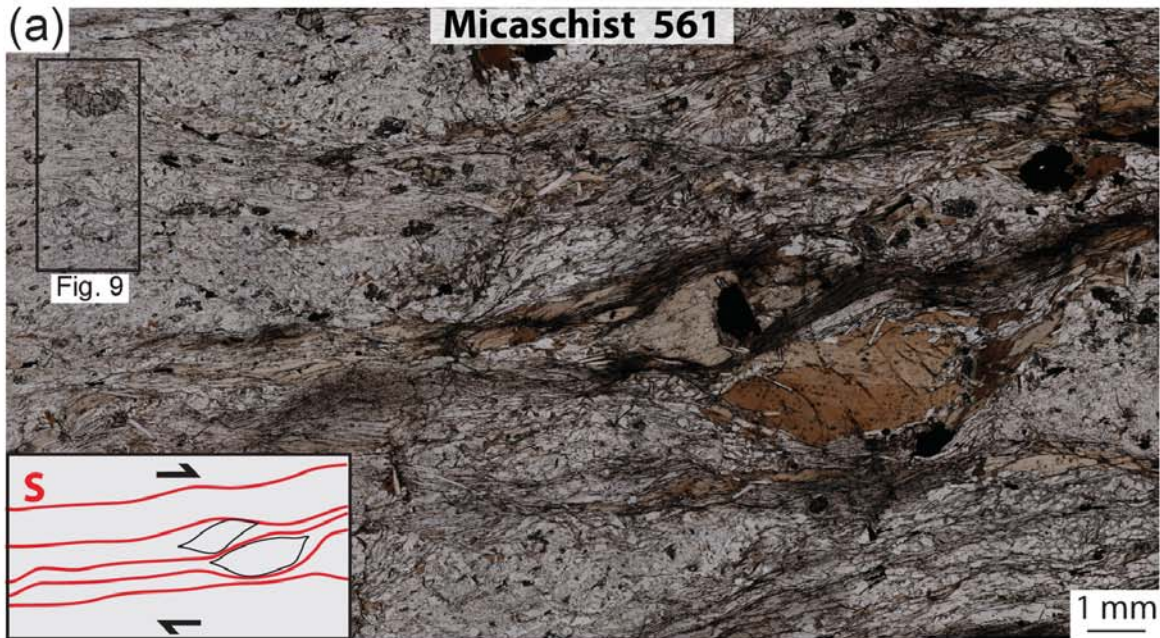


Figure 4.

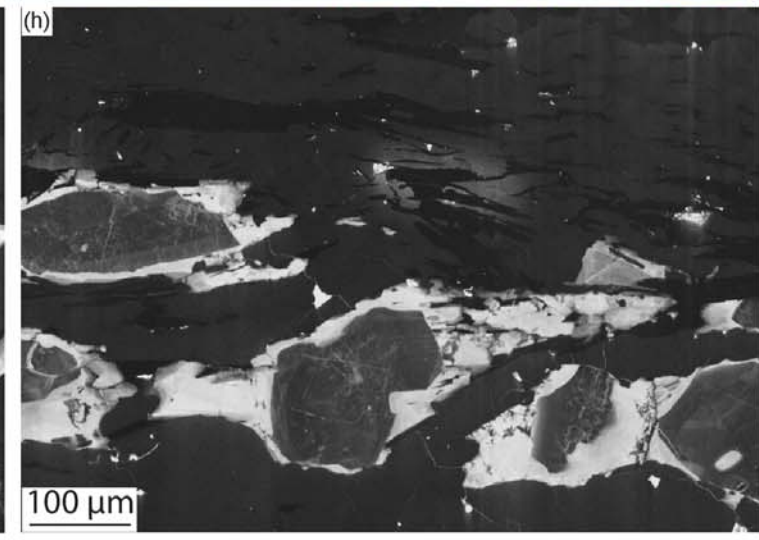
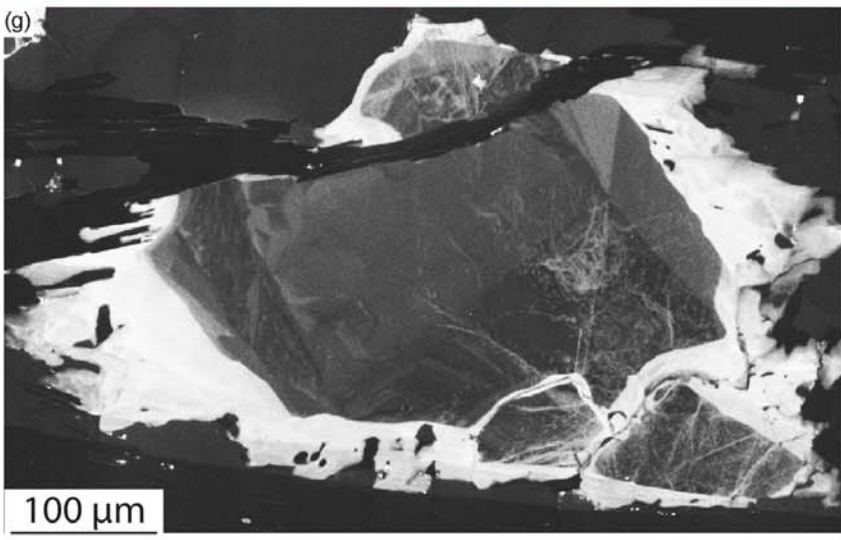
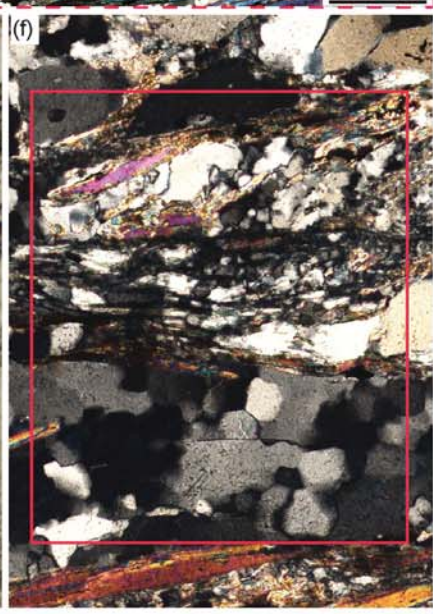
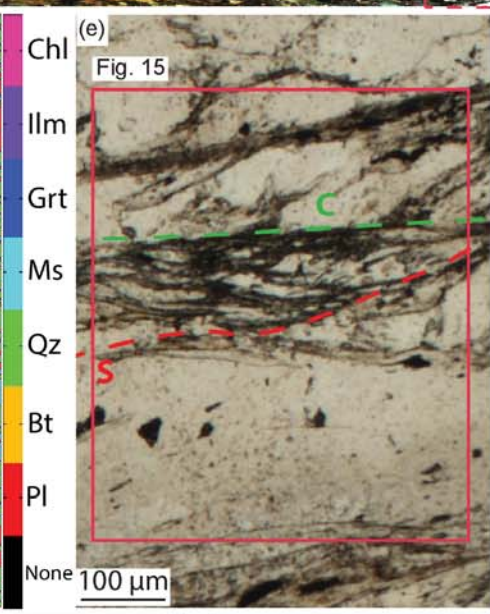
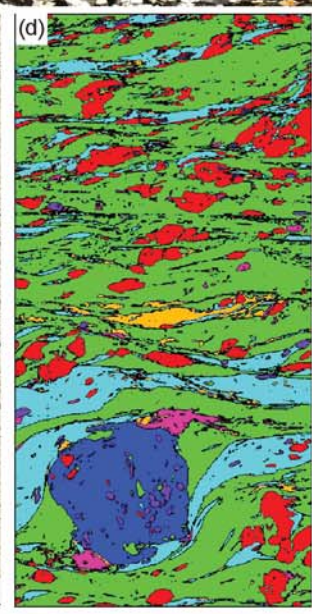
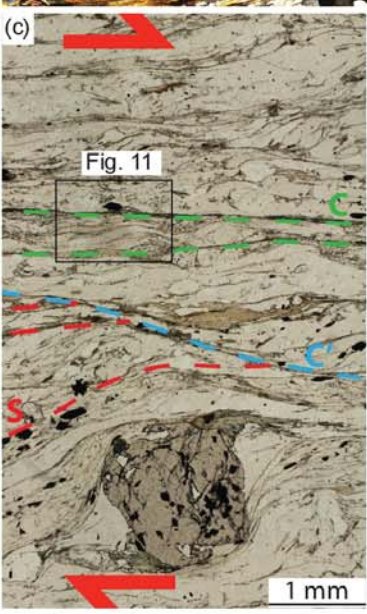
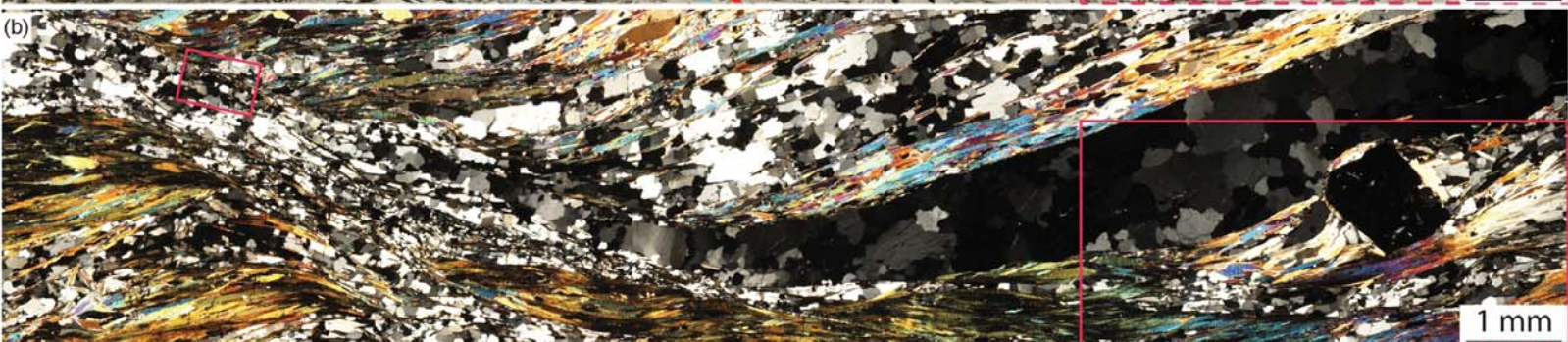
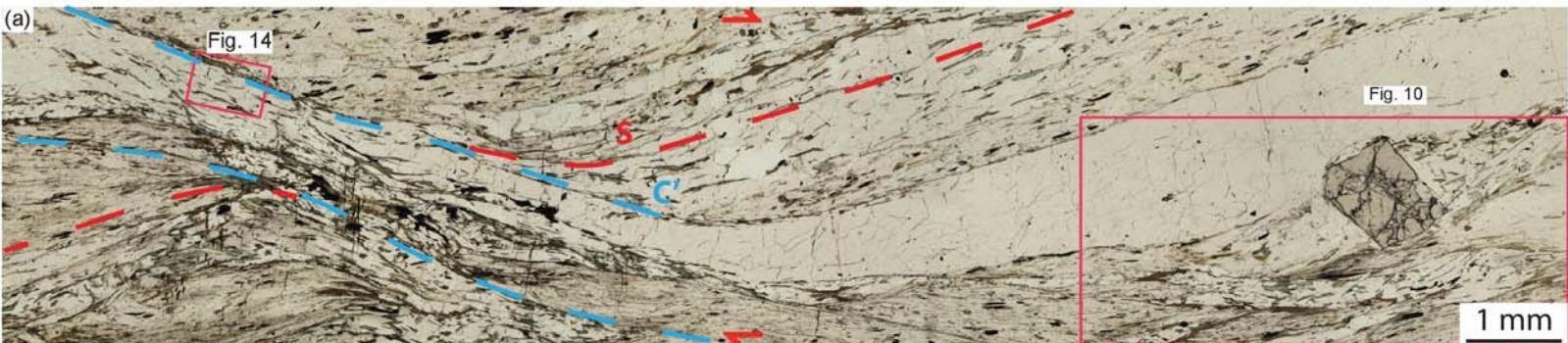


Figure 5.

(a)

Amphibolite 531



Fig. 6



1 mm

(b)

Amphibolite 543

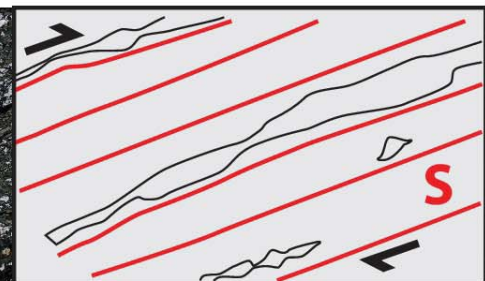


Fig. 7



Fig. 7



1 mm

Figure 6.

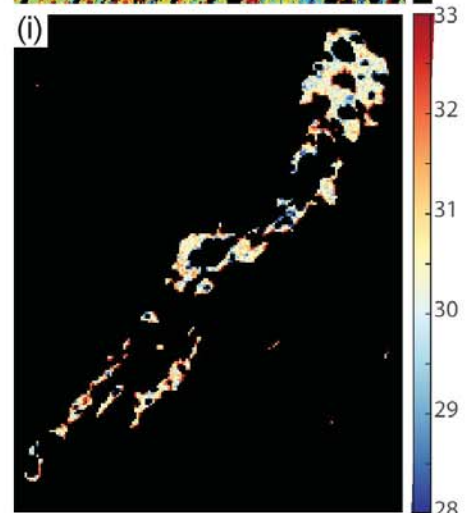
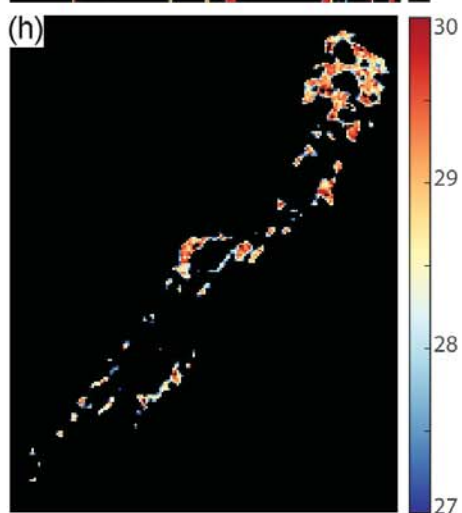
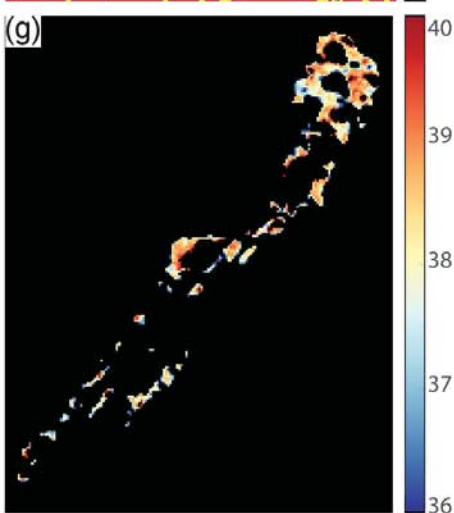
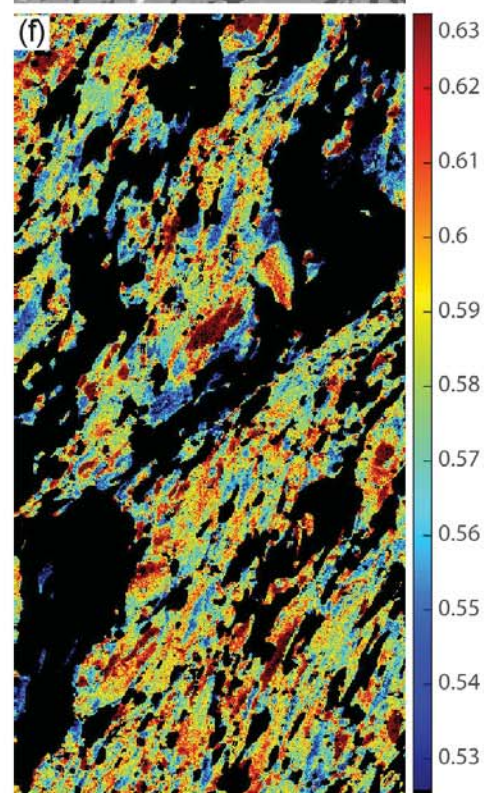
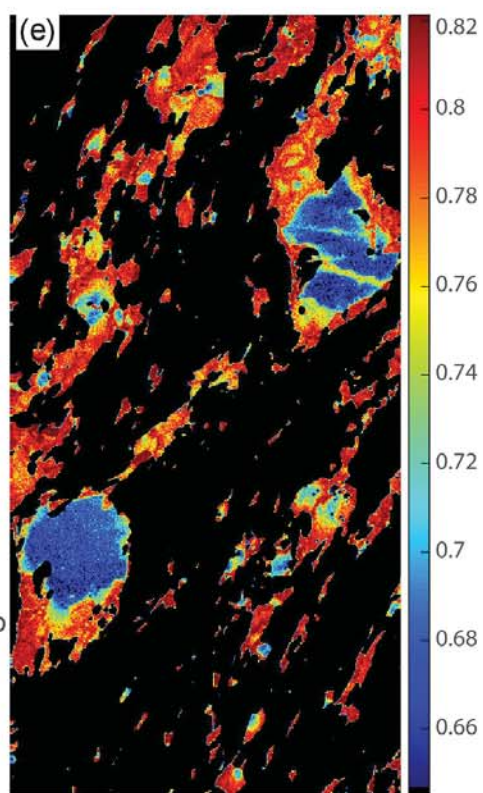
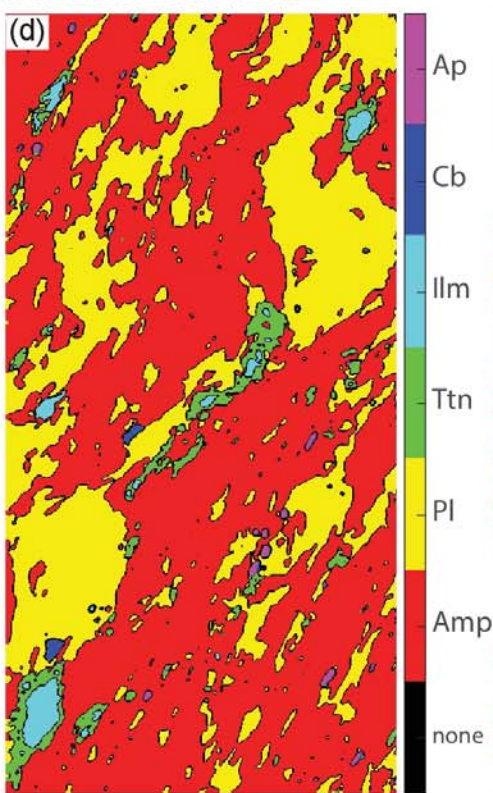
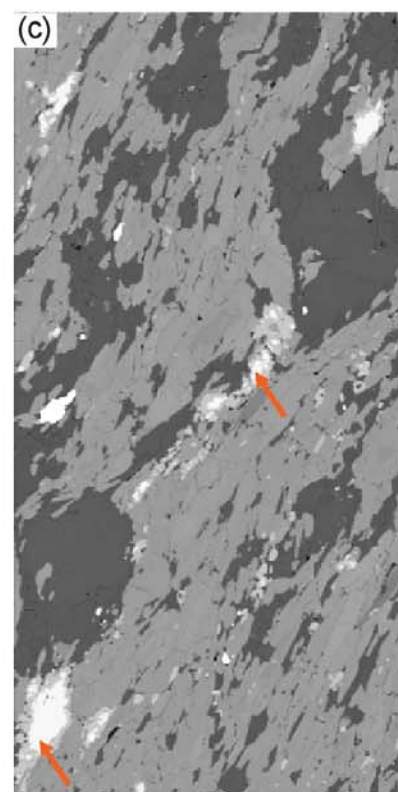
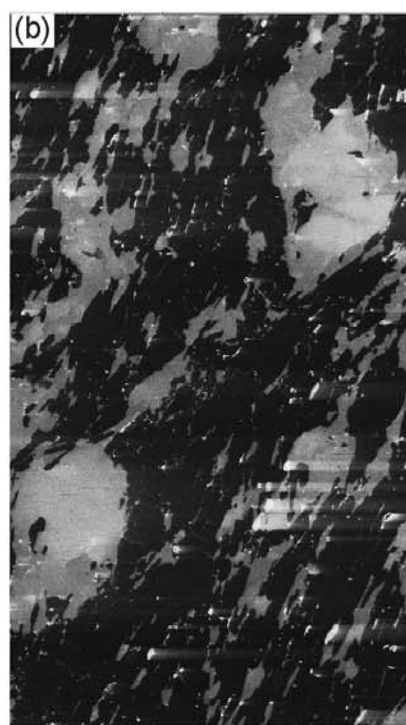
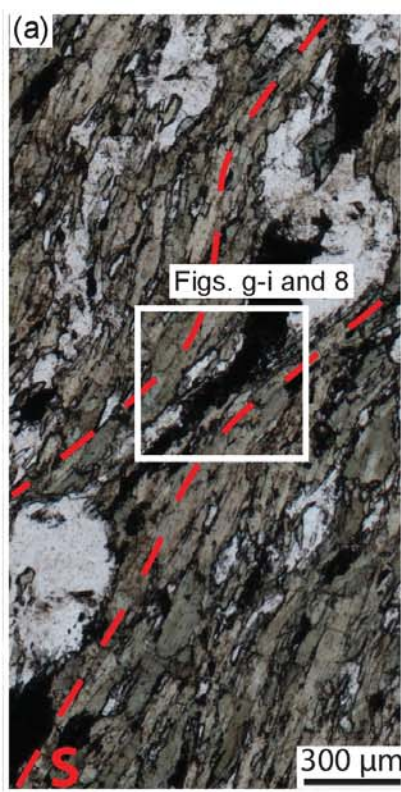


Figure 7.

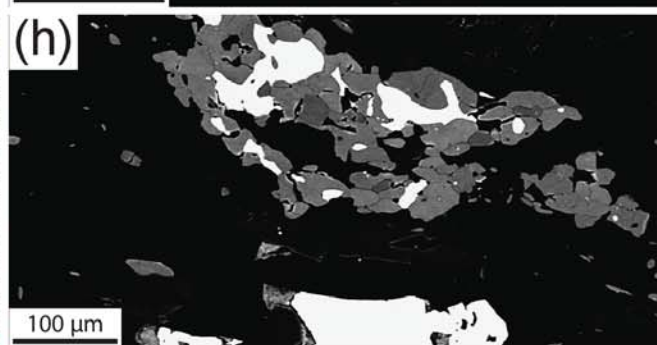
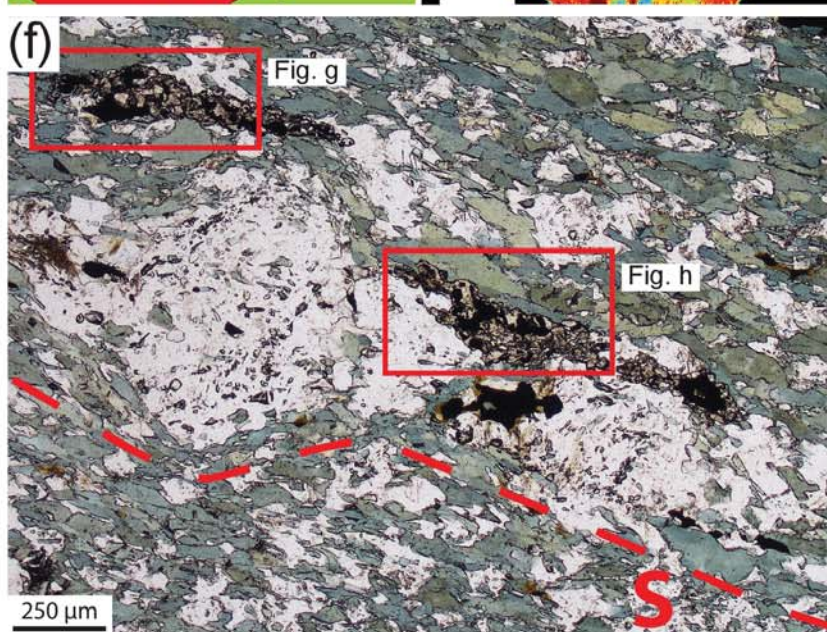
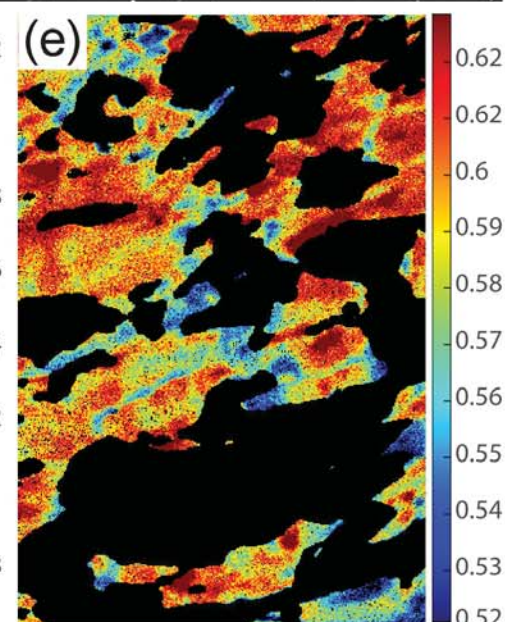
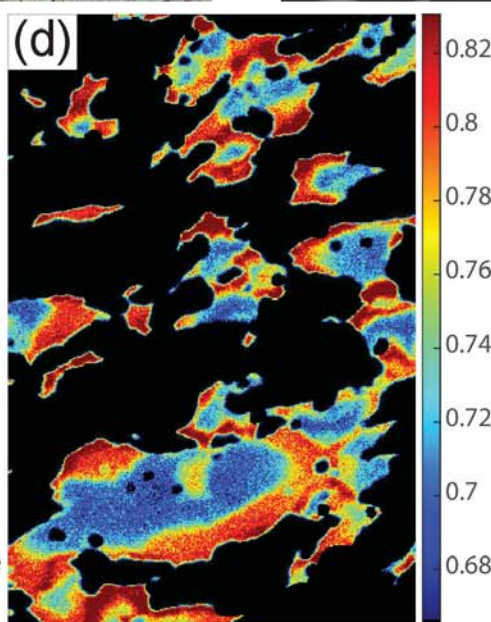
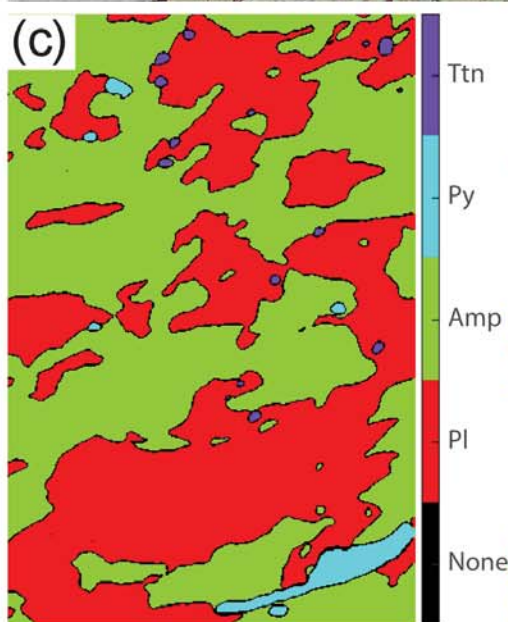
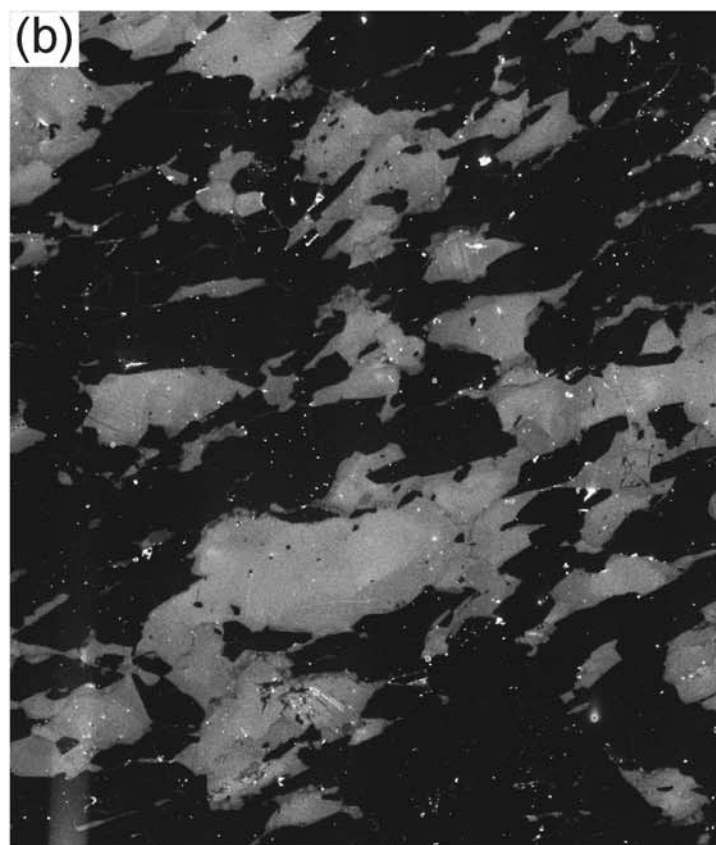
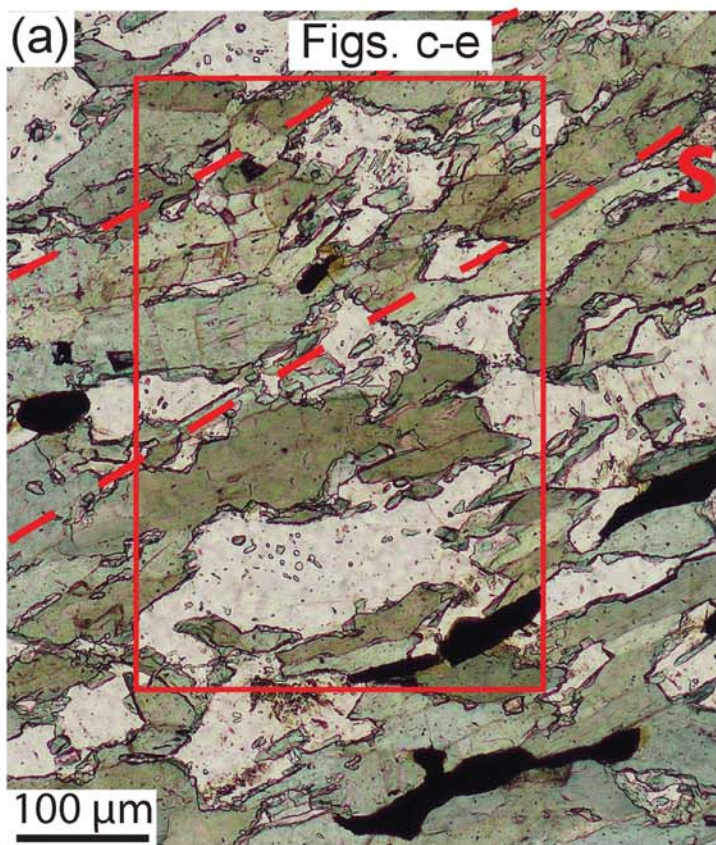


Figure 8.

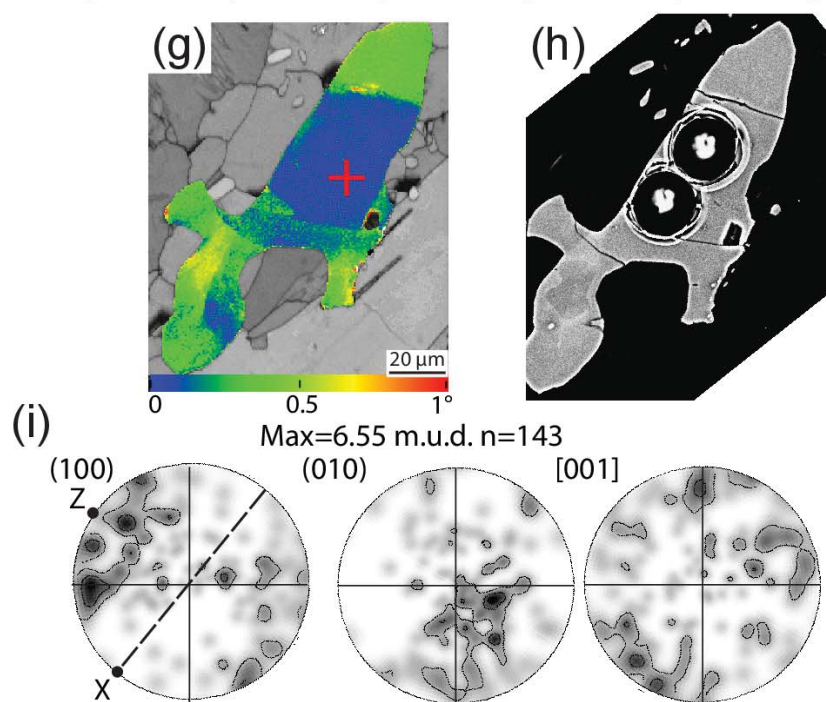
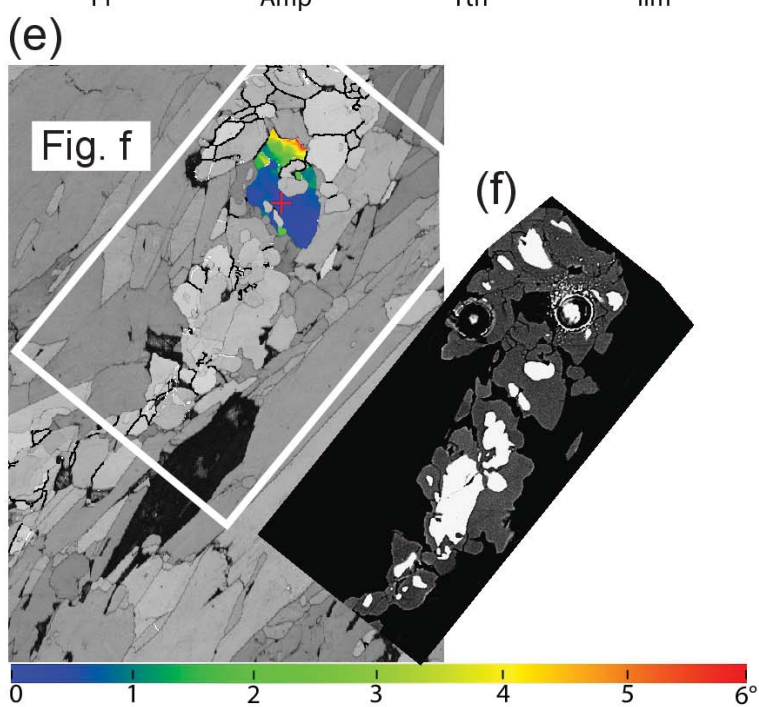
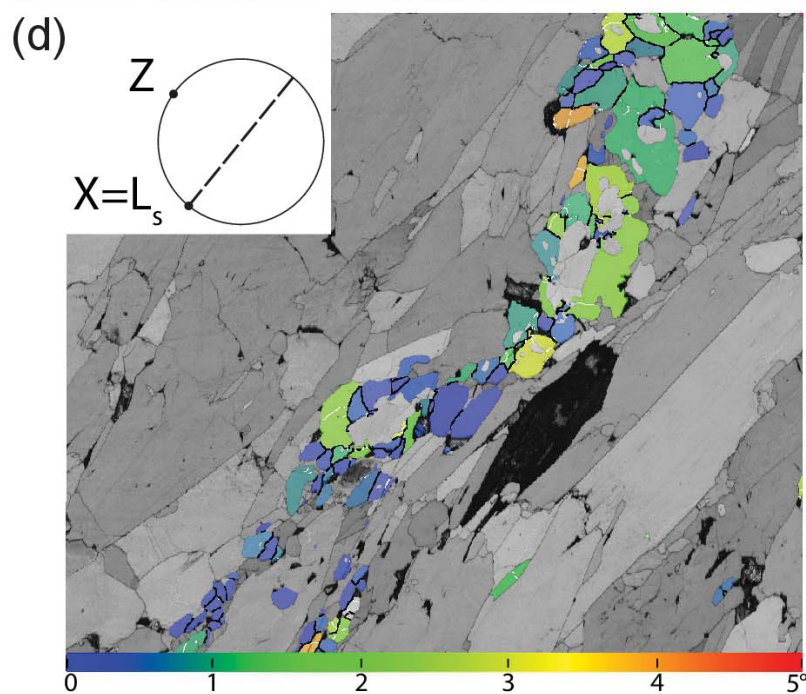
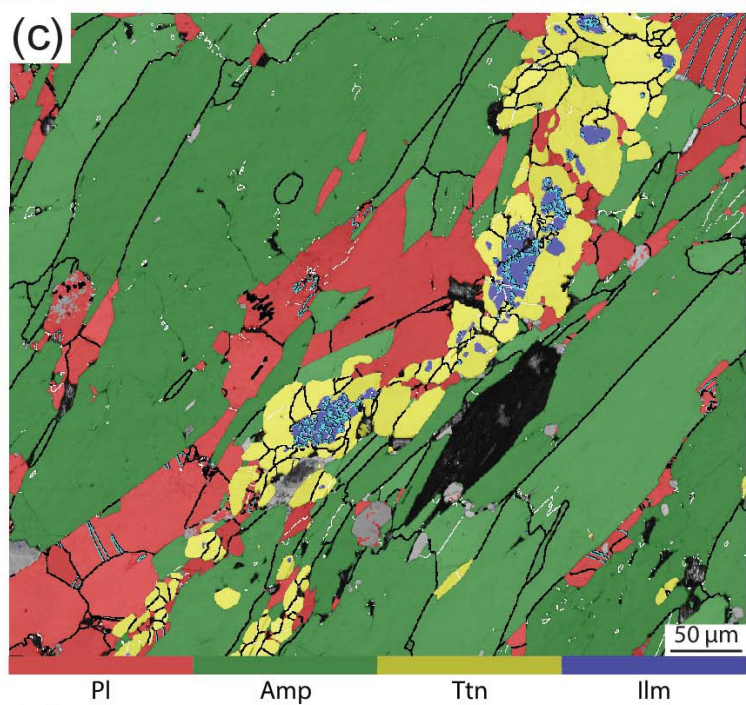
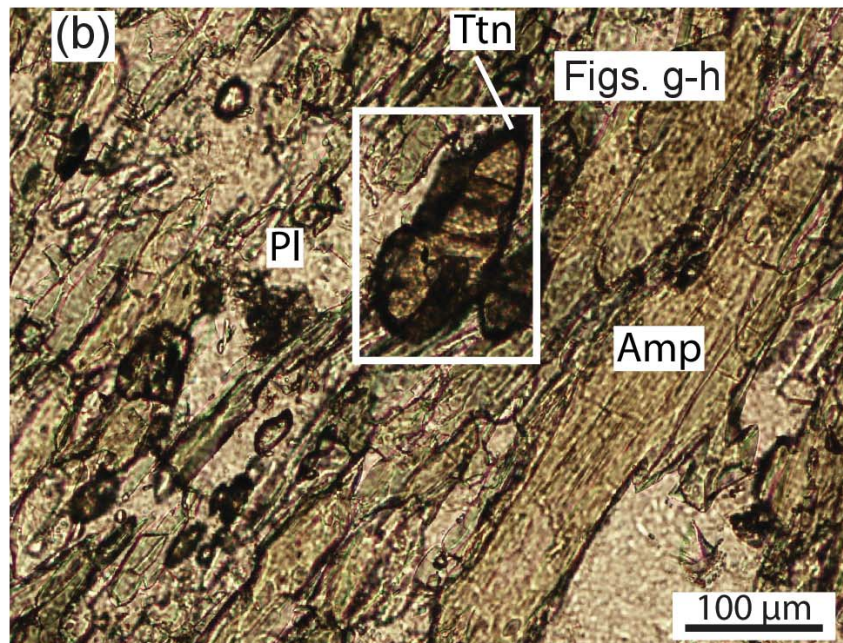
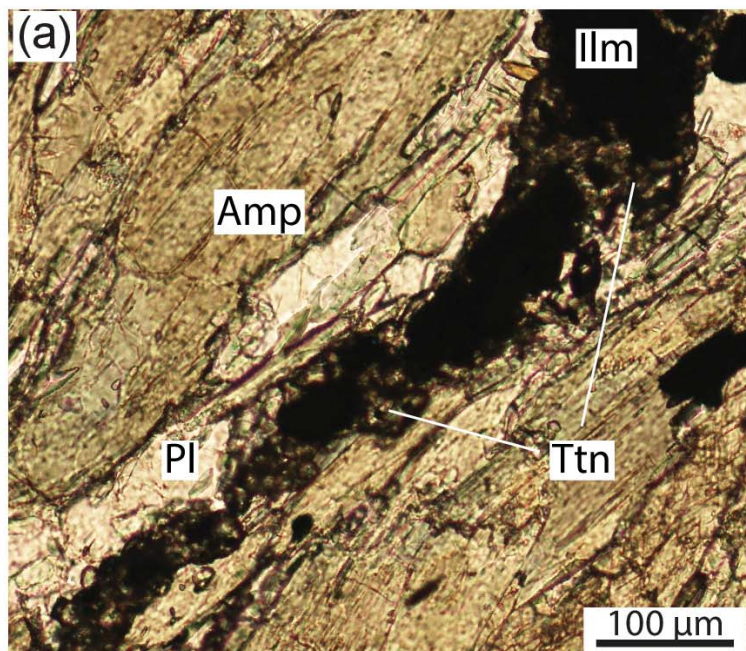


Figure 9.

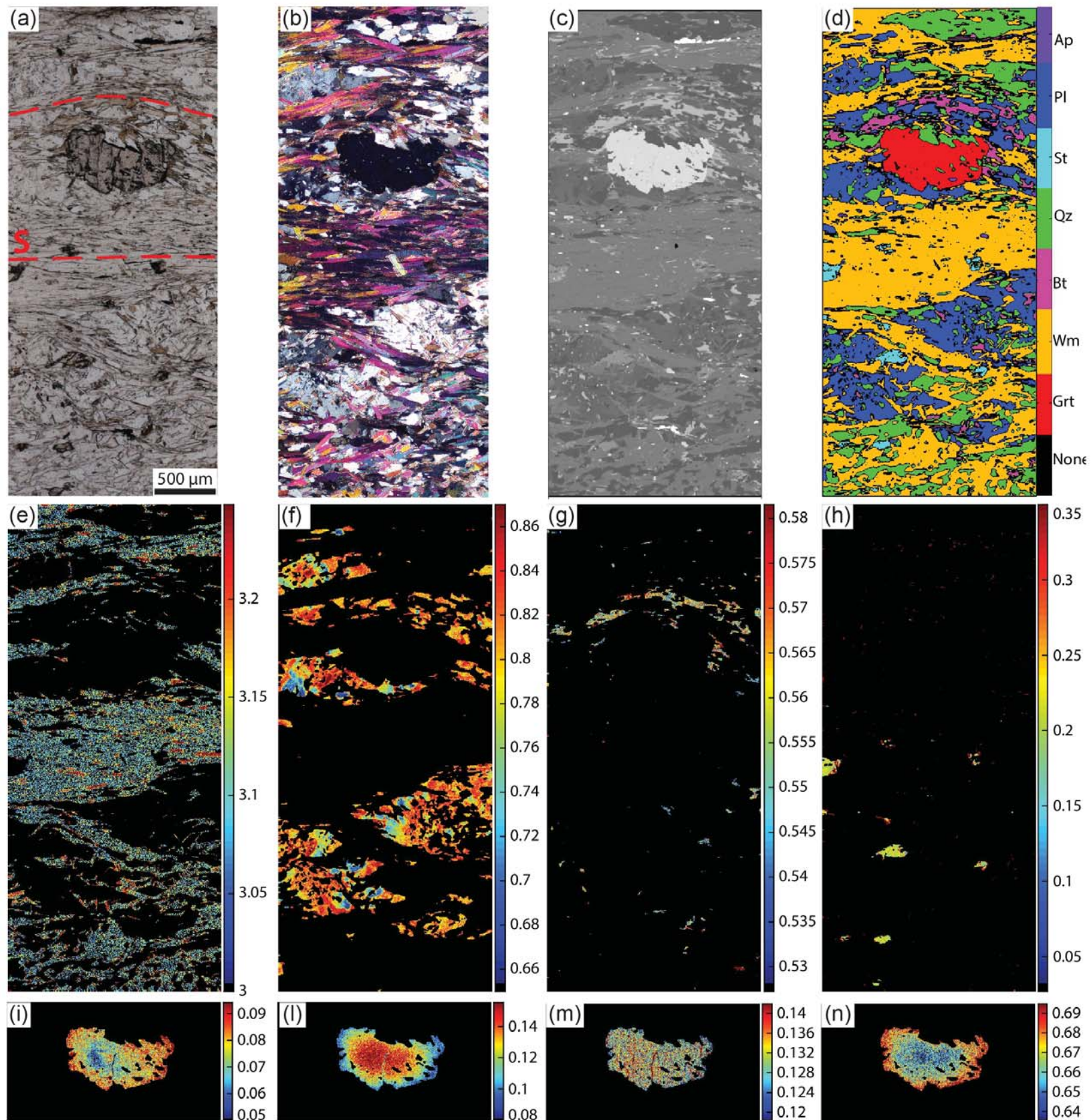


Figure 10.

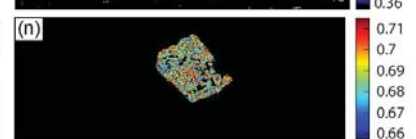
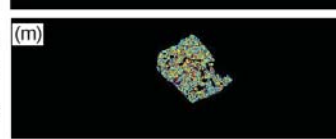
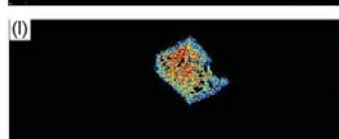
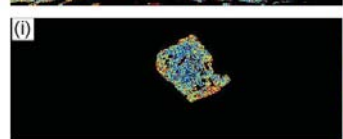
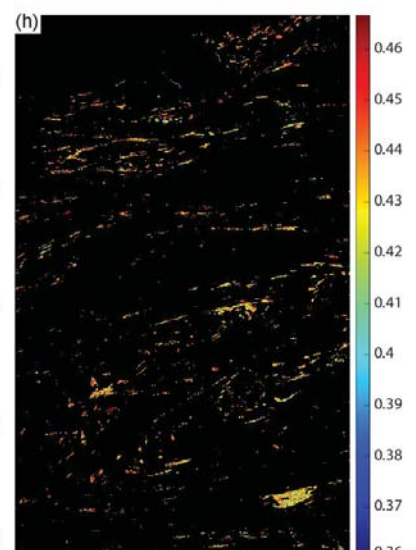
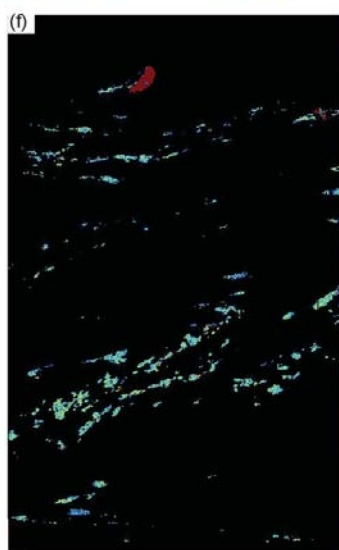
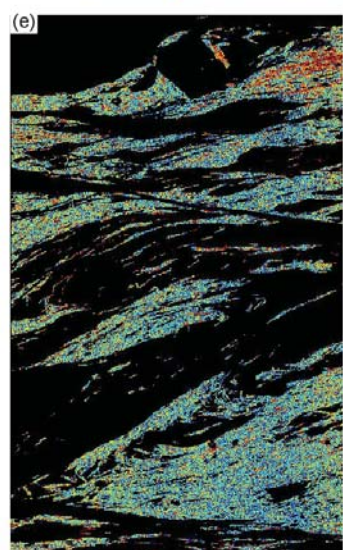
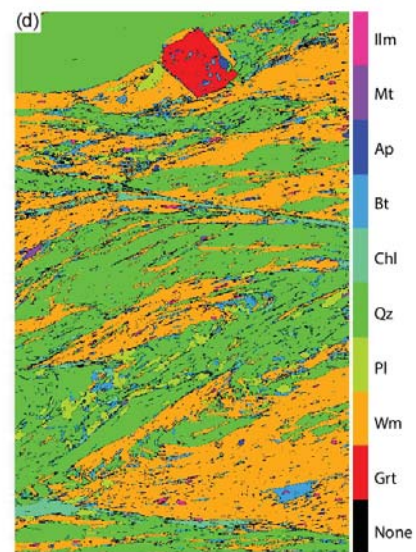
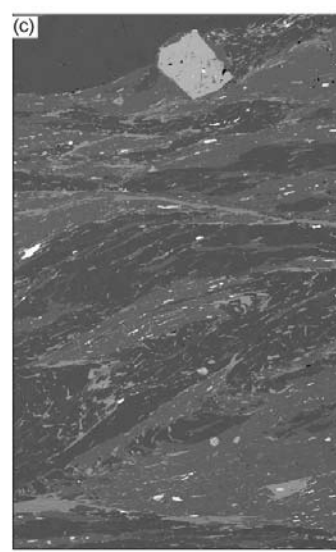
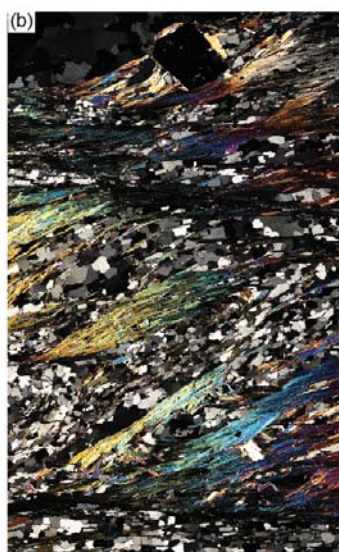
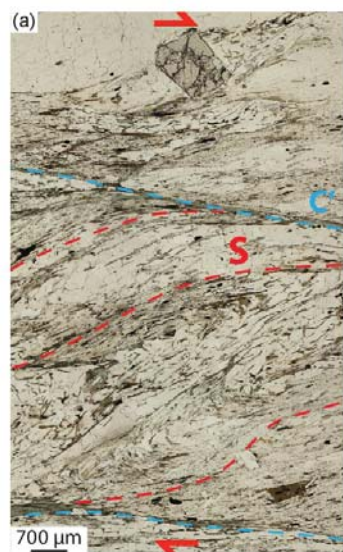


Figure 11.

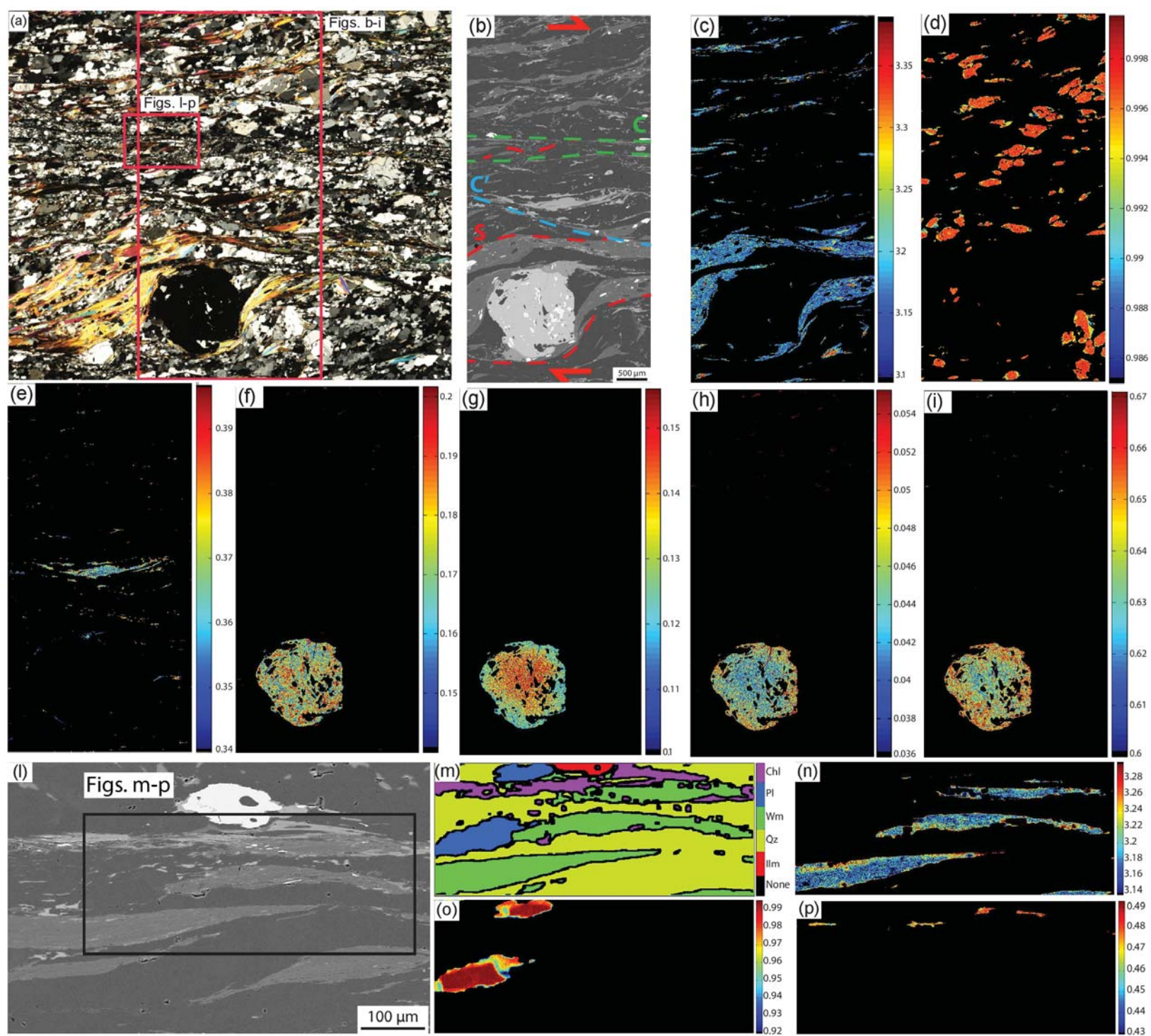
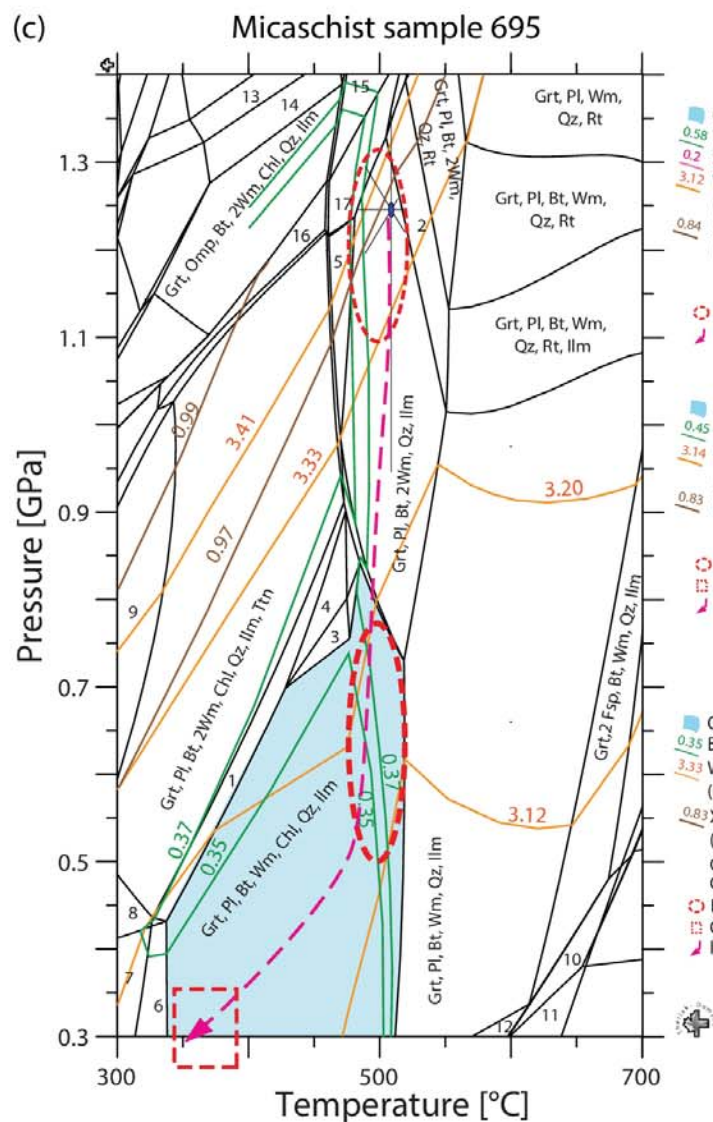
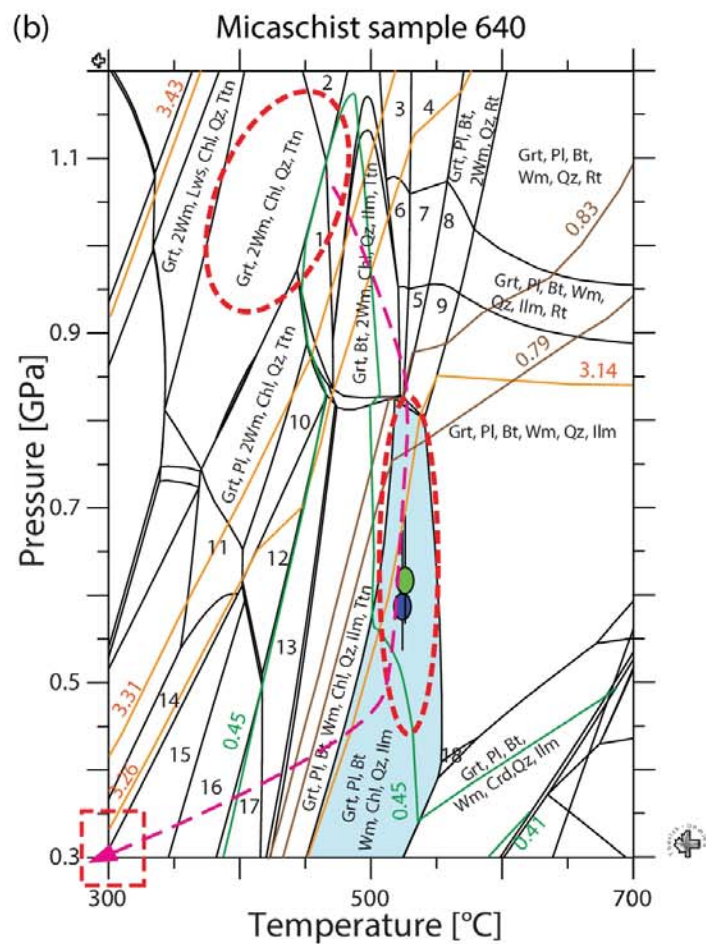
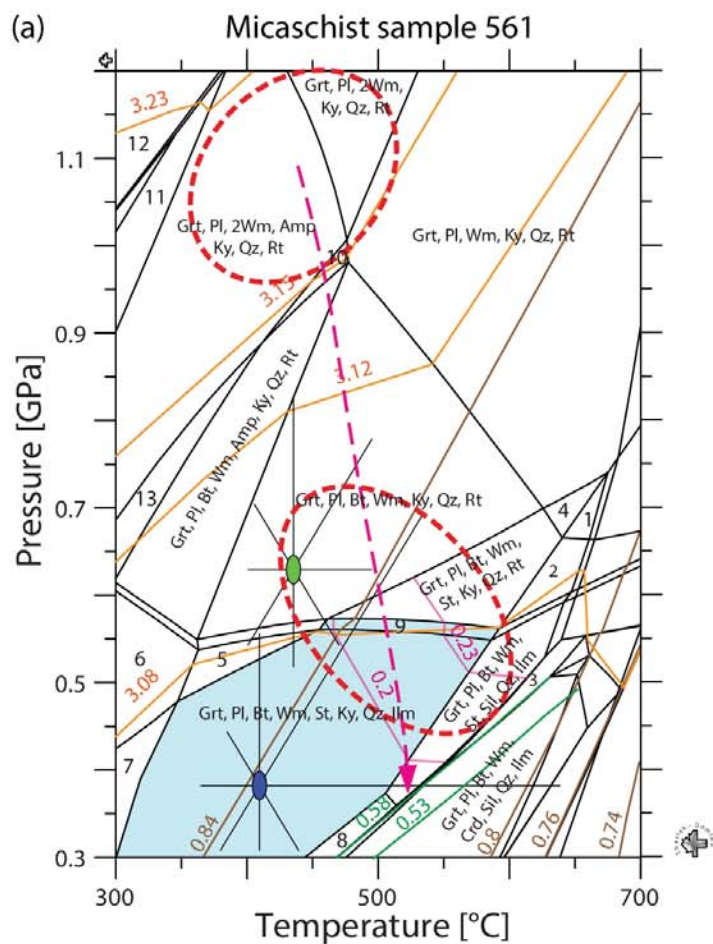


Figure 12.



Legend (a)

- 1: Grt, Pl, Wm, St, Sil, Qz, Rt
- 2: Grt, Pl, Bt, Wm, St, Sil, Qz, Rt
- 3: Grt, Pl, Bt, Wm, Crd, Sil, Qz, Ilm
- 4: Grt, Pl, Wm, St, Ky, Qz, Rt
- 5: Grt, Pl, Bt, Wm, Ky, Qz, Ilm
- 6: Grt, Pl, Bt, Wm, Amp, Ky, Qz, Ilm
- 7: Grt, Pl, Bt, Wm, St, Amp, Ky, Qz, Ilm
- 8: Grt, Pl, Bt, Wm, St, And, Qz, Ilm
- 9: Grt, Pl, Bt, Wm, St, Ky, Qz, Rt, Ilm
- 10: Grt, Pl, Wm, Amp, Ky, Qz, Rt
- 11: Grt, Pl, 2Wm, Amp, Gln Ky, Qz, Rt
- 12: Grt, 2Wm, Omp, Gln Ky, Qz, Rt
- 13: Grt, Pl, 2Wm, Bt, Amp, Ky, Qz, Rt

Legend (b)

- 1: Grt, 2Wm, Bt, Chl, Qz, Ttn
- 2: Grt, 2Wm, Chl, Qz, Rt, Ttn
- 3: Grt, Bt, Chl, 2Wm, Qz, Rt
- 4: Grt, Bt, 2Wm, Qz, Rt
- 5: Grt, Bt, 2Wm, Qz, Ilm
- 6: Grt, Bt, Chl, 2Wm, Qz, Ilm, Rt
- 7: Grt, Bt, 2Wm, Qz, Ilm, Rt
- 8: Grt, Pl, Bt, 2Wm, Qz, Ilm, Rt
- 9: Grt, Pl, Bt, 2Wm, Qz, Ilm
- 10: Grt, Pl, 2Wm, Chl, Qz, Rt, Ttn
- 11: Grt, Pl, 2Wm, Chl, Qz, Ttn
- 12: Grt, Pl, Wm, Chl, Qz, Rt, Ttn
- 13: Grt, Pl, Bt, Wm, Chl, Qz, Rt, Ttn
- 14: Pl, 2Wm, Chl, Qz, Ttn
- 15: Pl, Wm, Chl, Qz, Ttn
- 16: Pl, Wm, Chl, Qz, Ttn, Rt
- 17: Pl, Bt, Wm, Chl, Qz, Ttn, Rt
- 18: Grt, Pl, Bt, Wm, St, Qz, Ilm

Legend (c)

- 1: Grt, Pl, Bt, 2Wm, Chl, Qz, Ilm
- 2: Grt, Pl, Bt, 2Wm, Qz, Ilm, Rt
- 3: Grt, Pl, Wm, Chl, Qz, Ilm
- 4: Grt, Pl, 2Wm, Chl, Qz, Ilm
- 5: Grt, Pl, Bt, 2Wm, Qz, Ilm, Ttn
- 6: Grt, Pl, Bt, Wm, Cld, Chl, Qz, Ilm
- 7: Grt, Pl, Bt, Wm, Cld, Chl, Qz, Ilm, Ttn
- 8: Grt, Pl, Bt, 2Wm, Cld, Chl, Qz, Ilm, Ttn
- 9: Grt, Pl, Bt, 2Wm, Qz, Ilm, Ttn
- 10: Grt, 2Fsp, Wm, Crd, Qz, Ilm
- 11: Grt, 2Fsp, Crd, Qz, Ilm
- 12: Grt, Pl, Bt, Wm, Crd, Qz, Ilm
- 13: Grt, Omp, 2Wm, Chl, Qz, Ilm, Rt
- 14: Grt, Omp, 2Wm, Chl, Qz, Ilm
- 15: Grt, Omp, Bt, 2Wm, Qz, Ilm
- 16: Grt, Omp, Pl, Bt, 2Wm, Chl, Qz, Ilm
- 17: Grt, Omp, Pl, Bt, 2Wm, Qz, Ilm

Figure 13.

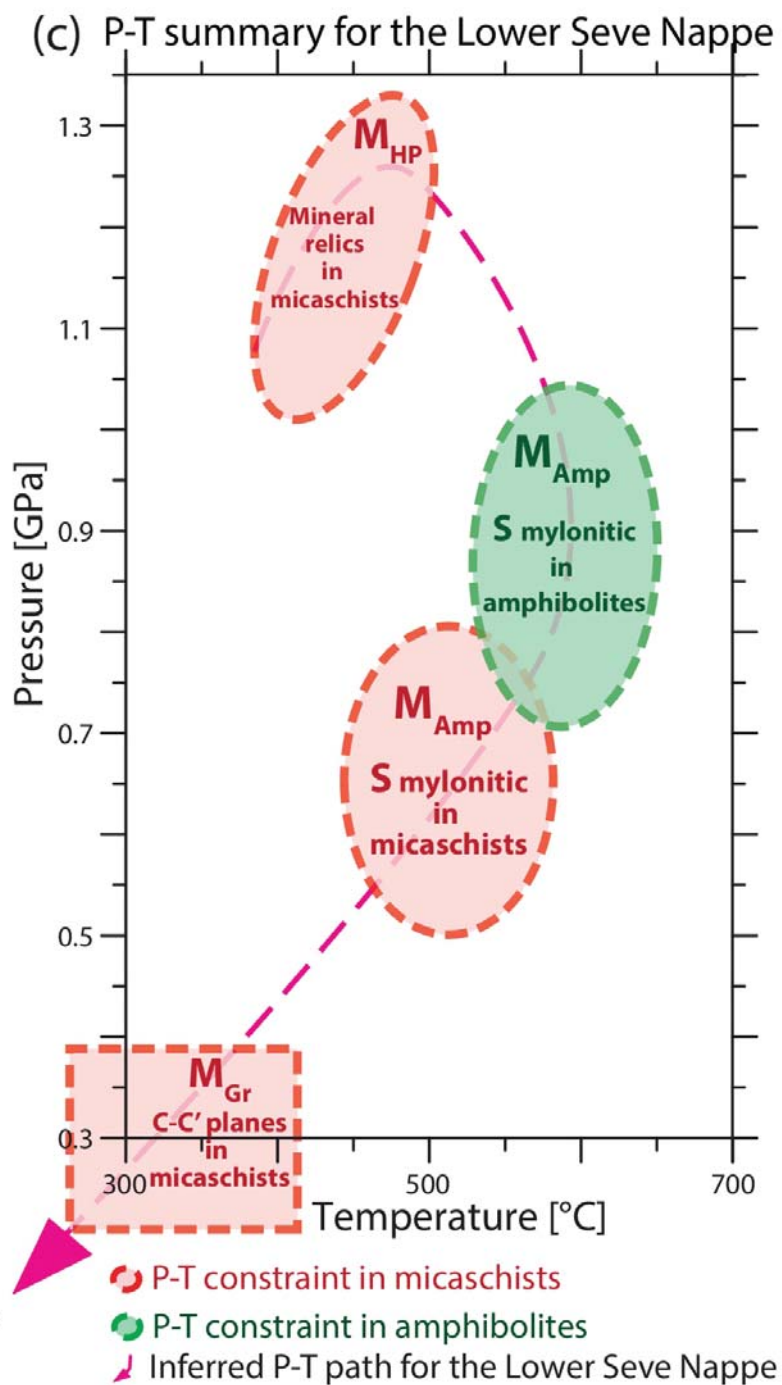
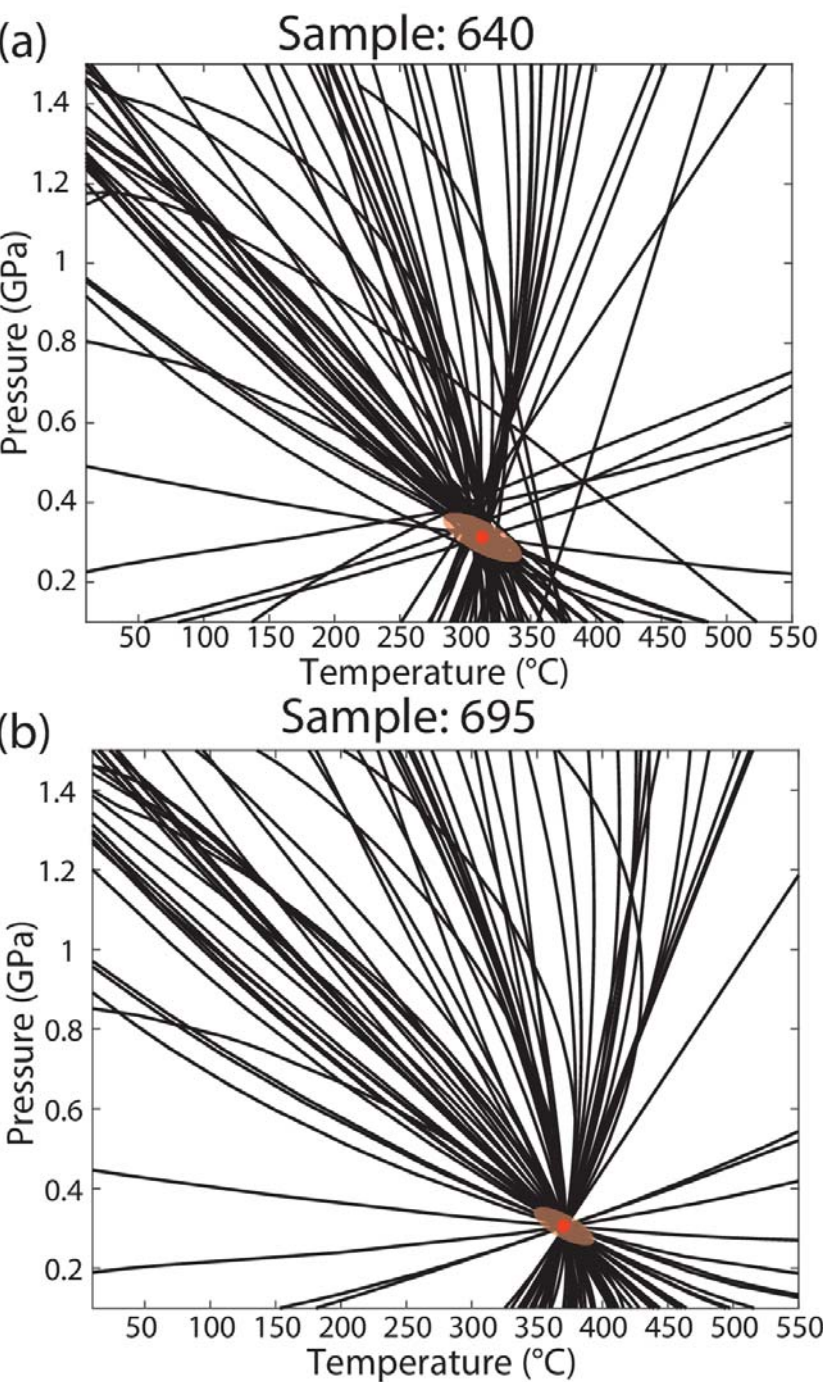


Figure 14.

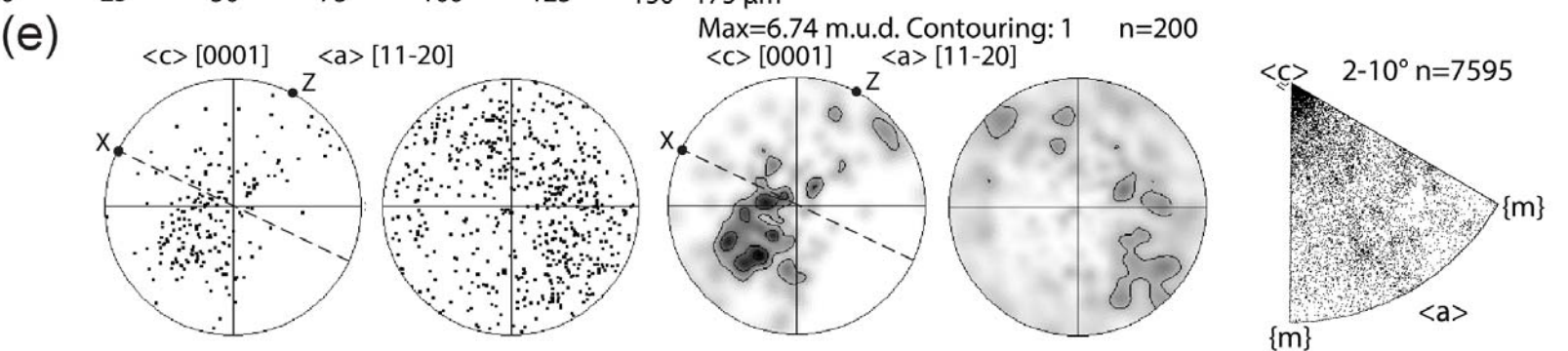
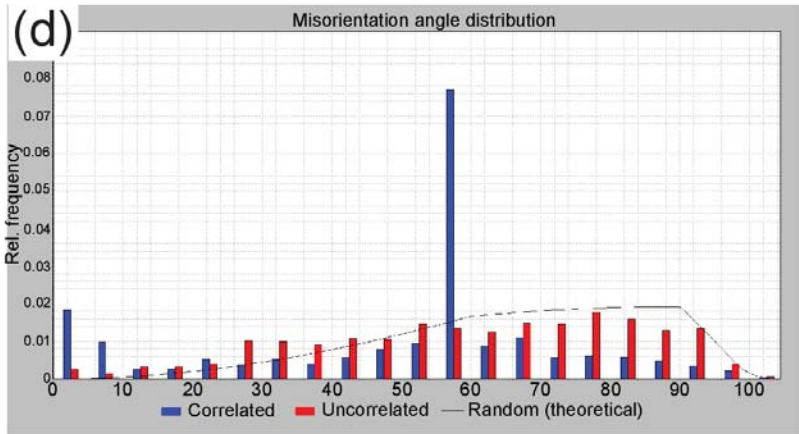
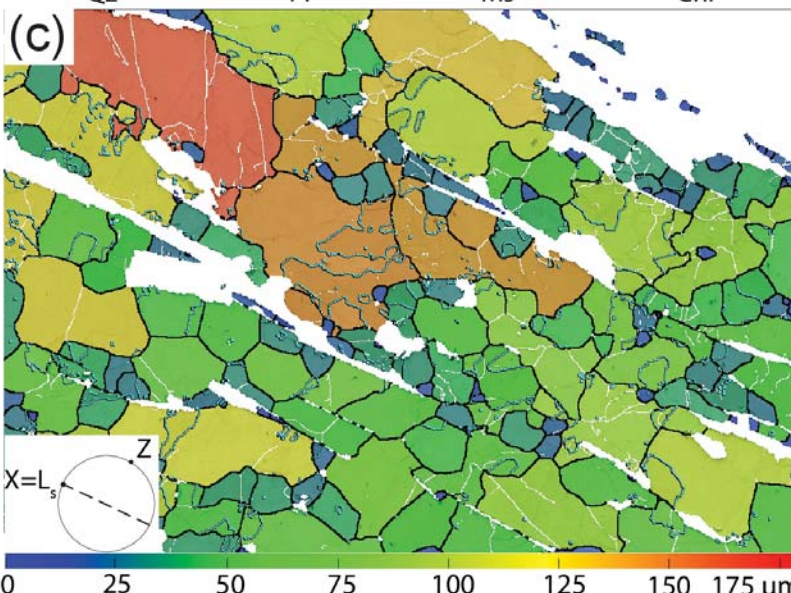
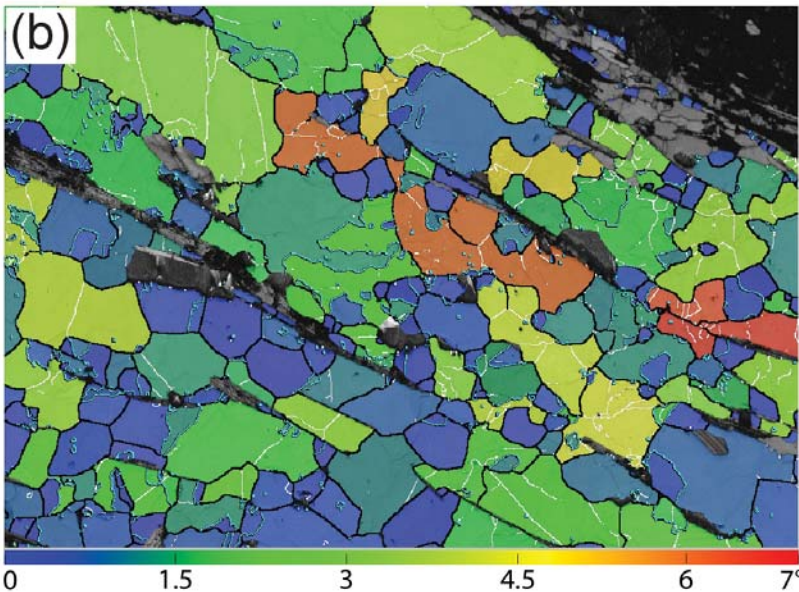
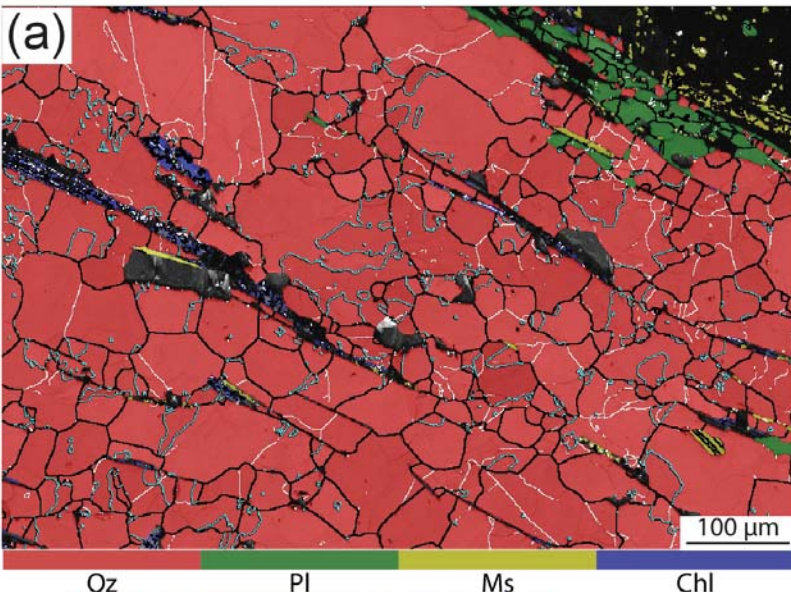


Figure 15.

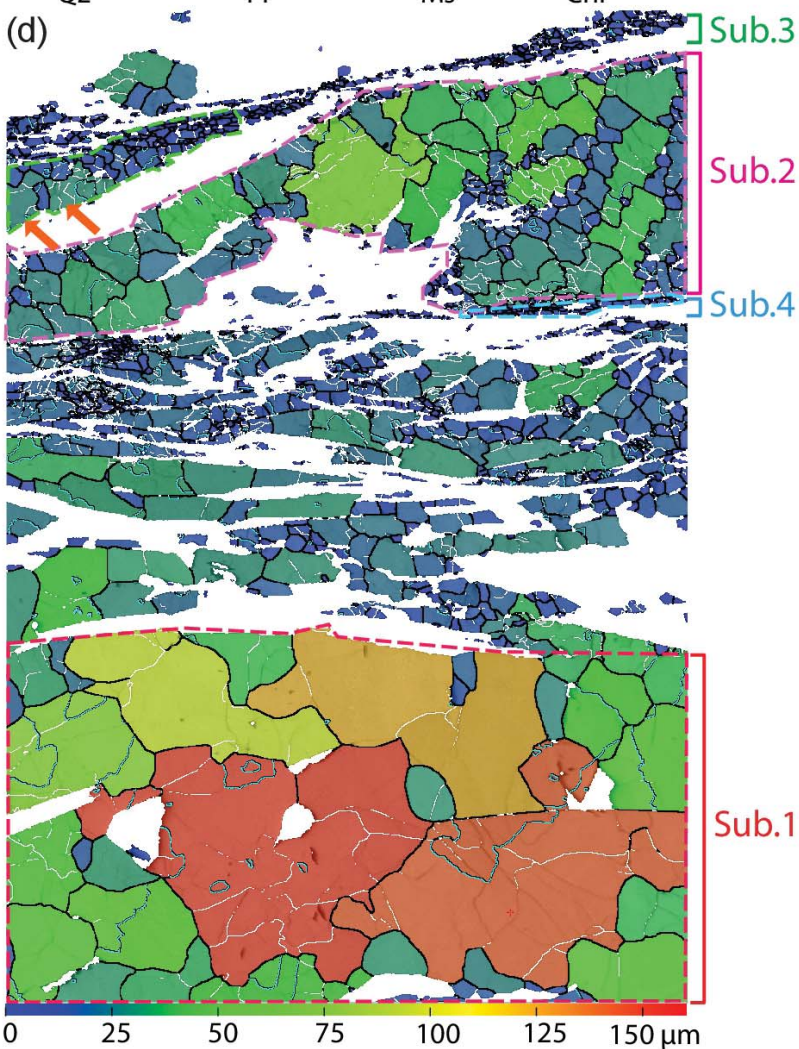
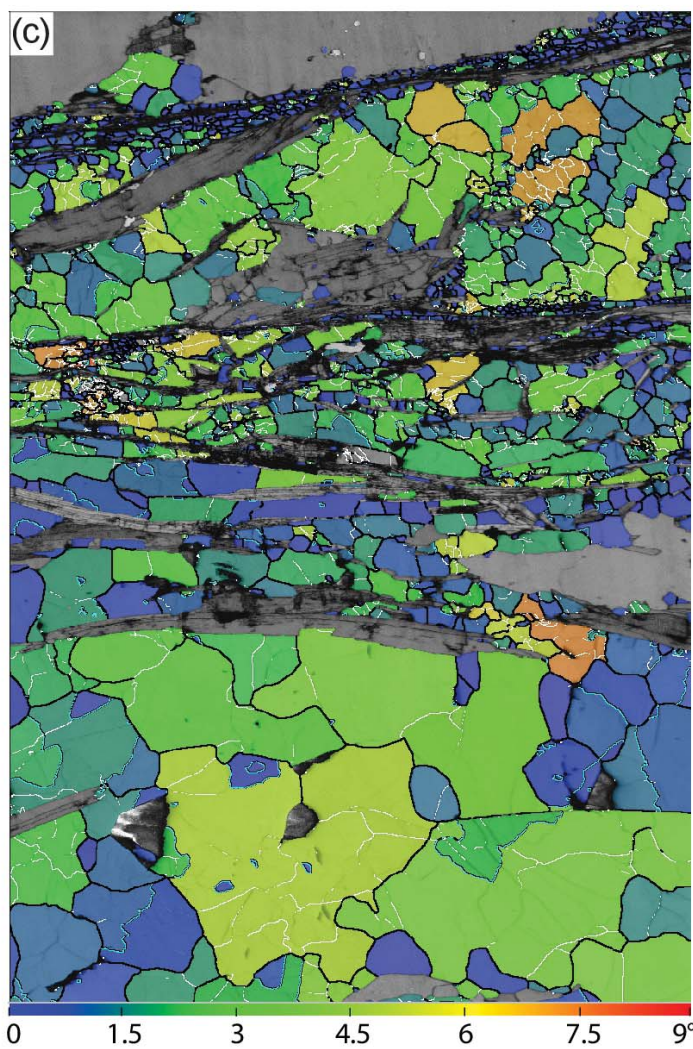
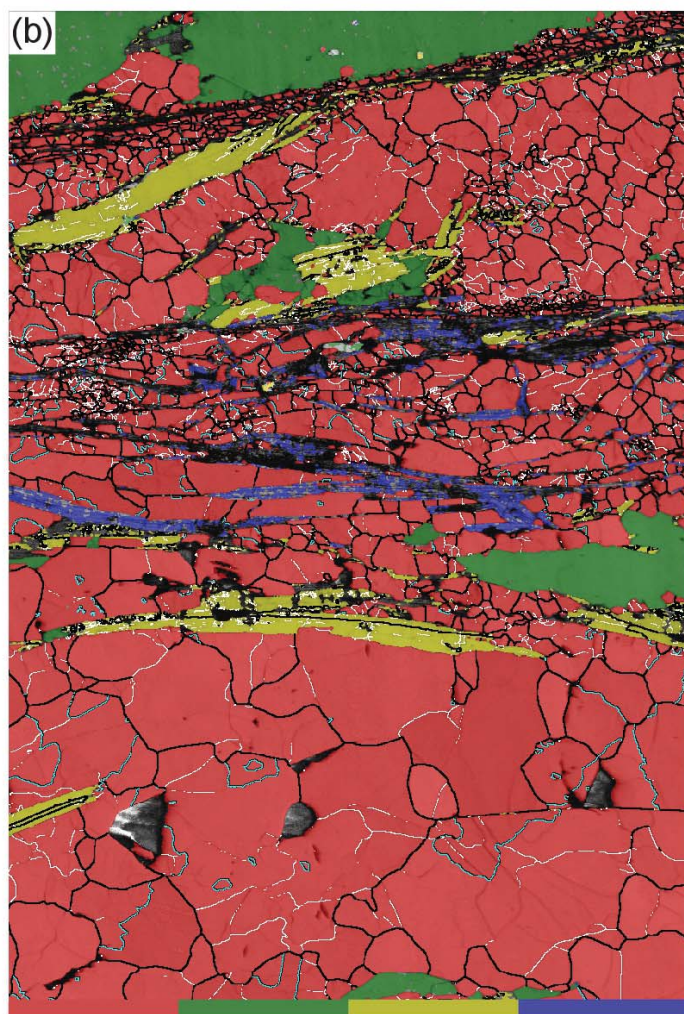
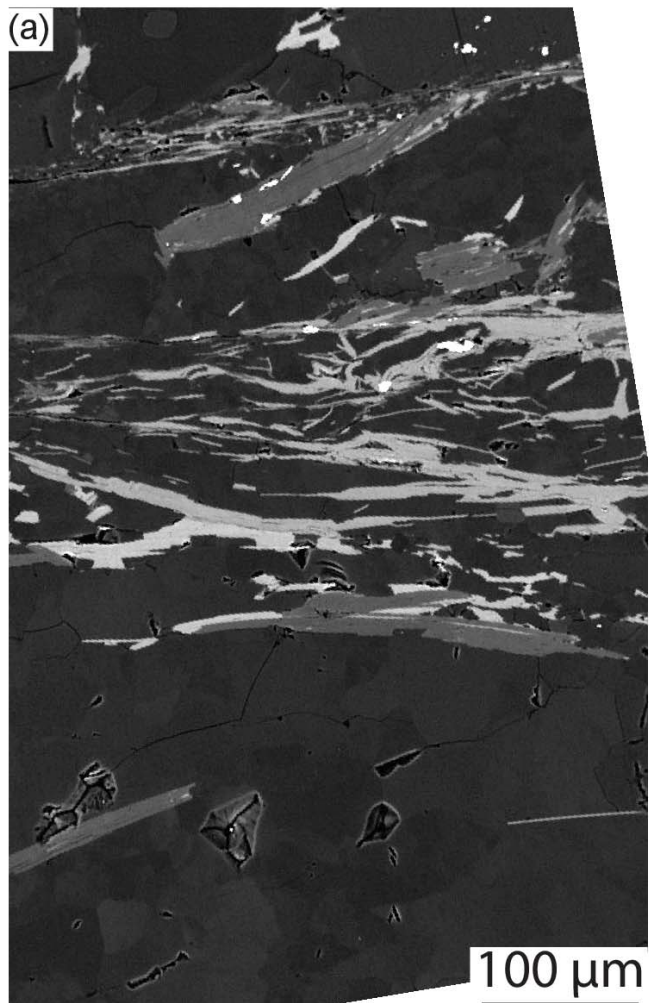


Figure 16.

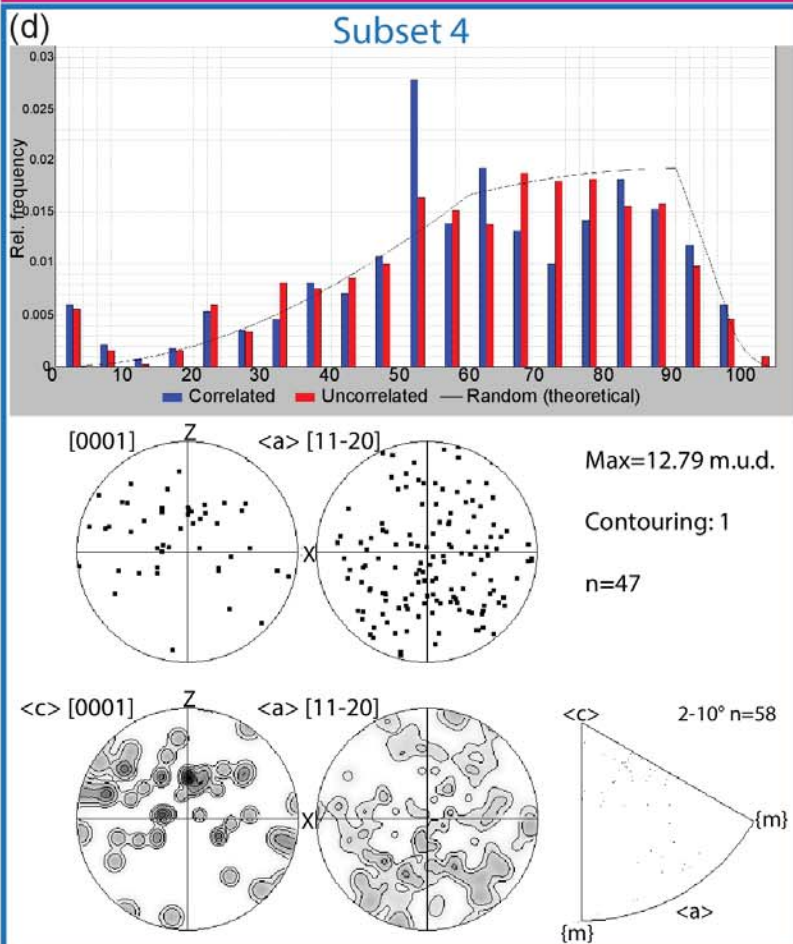
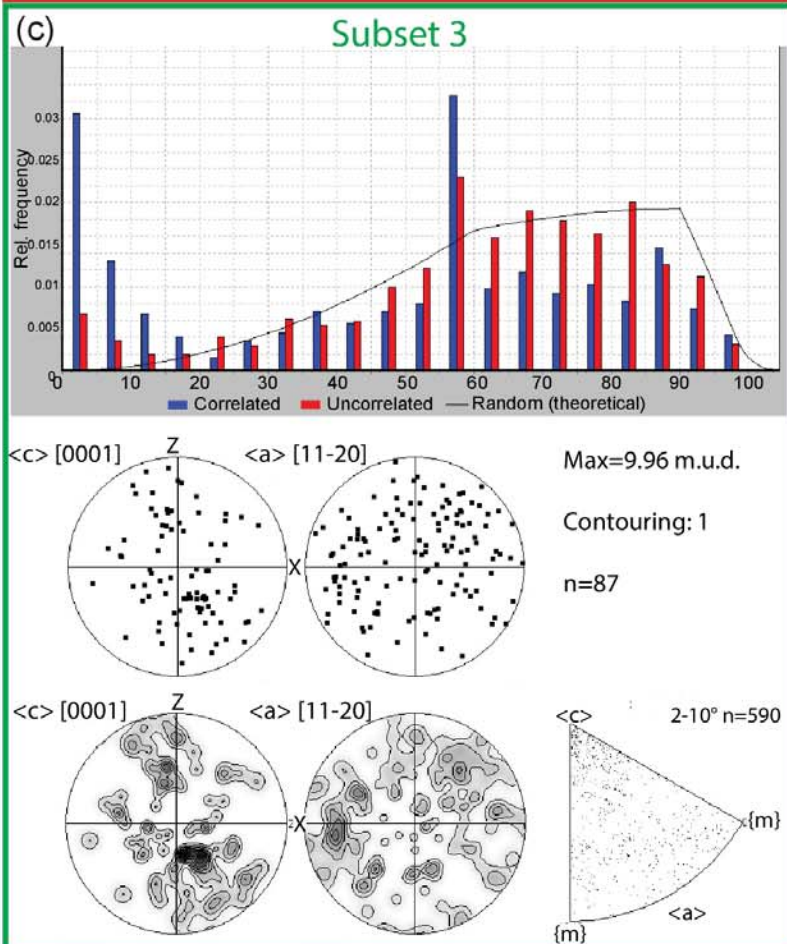
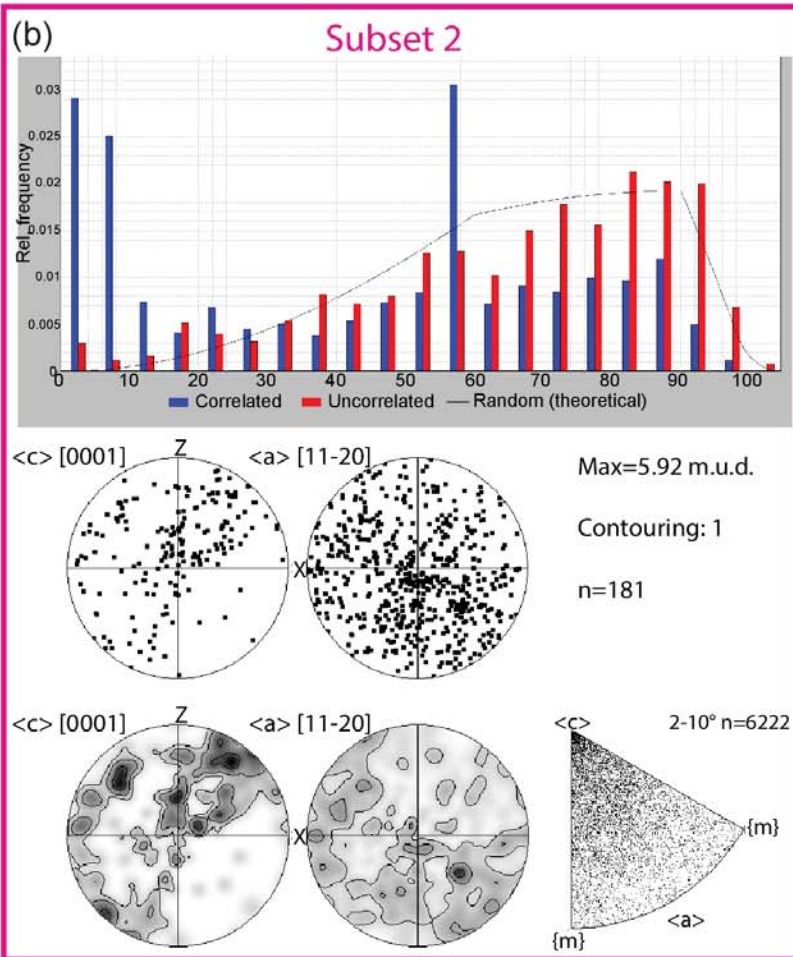
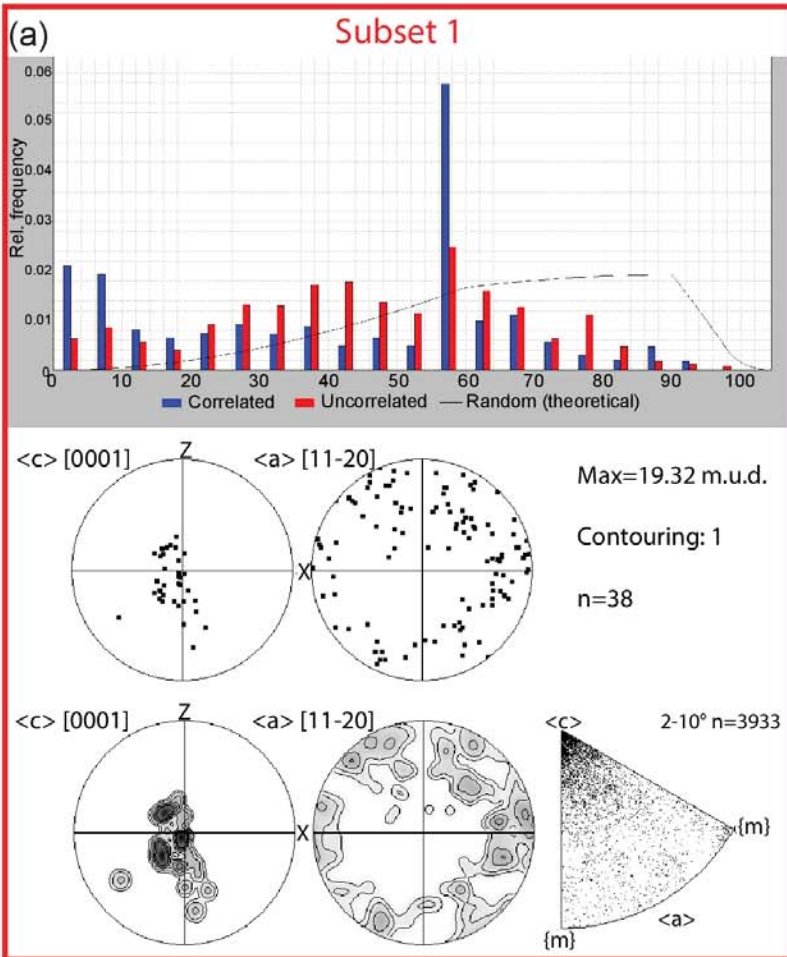


Figure 17.

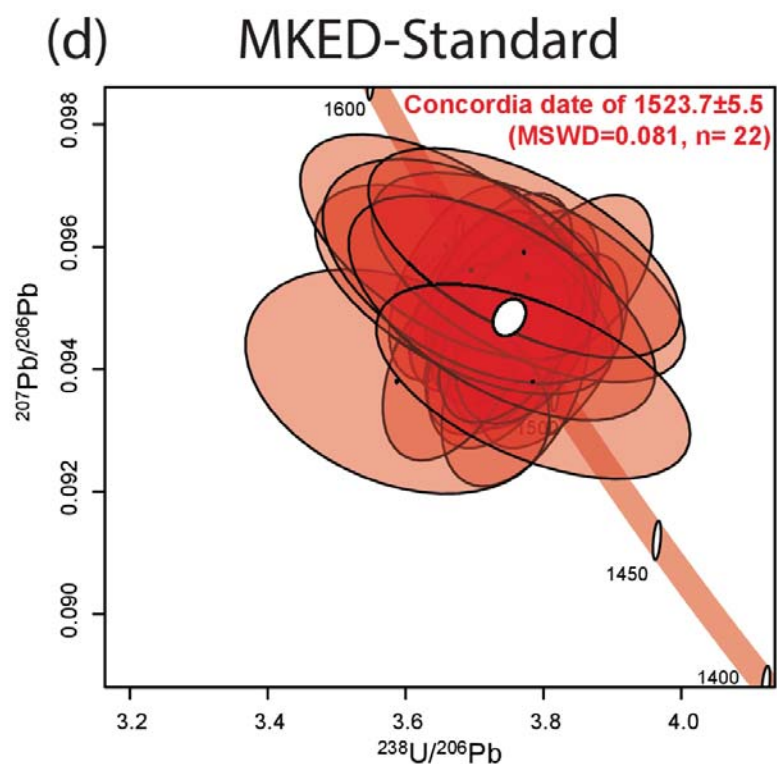
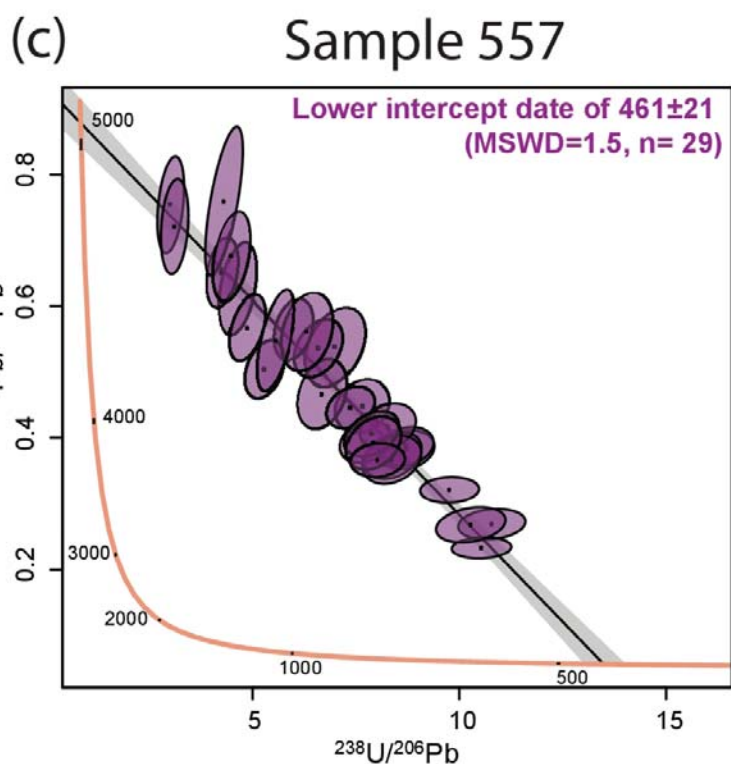
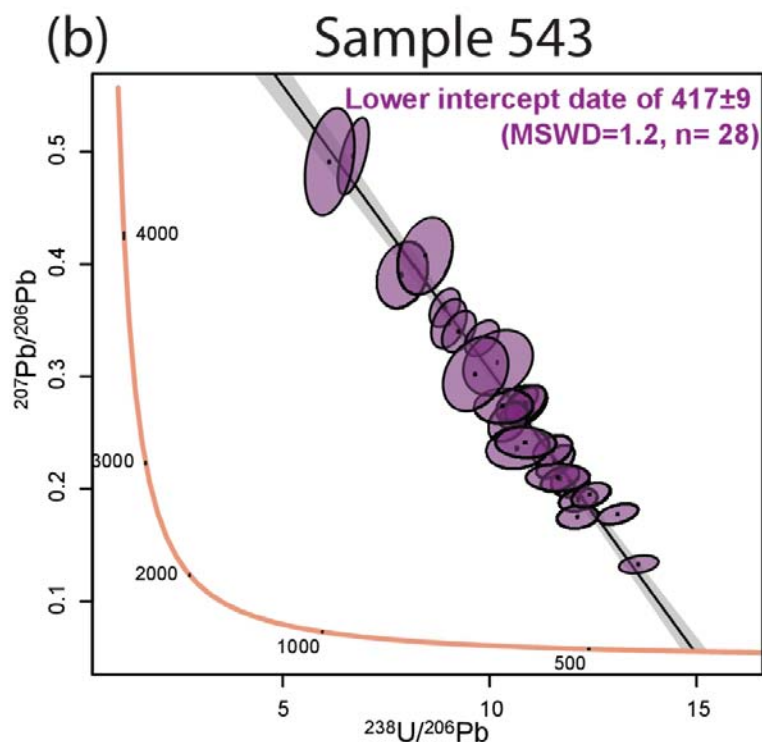
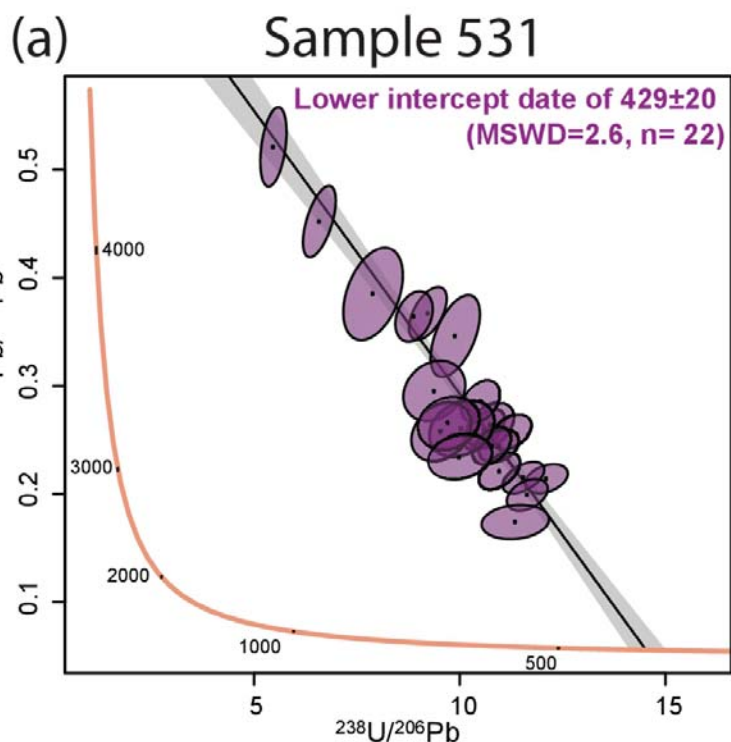
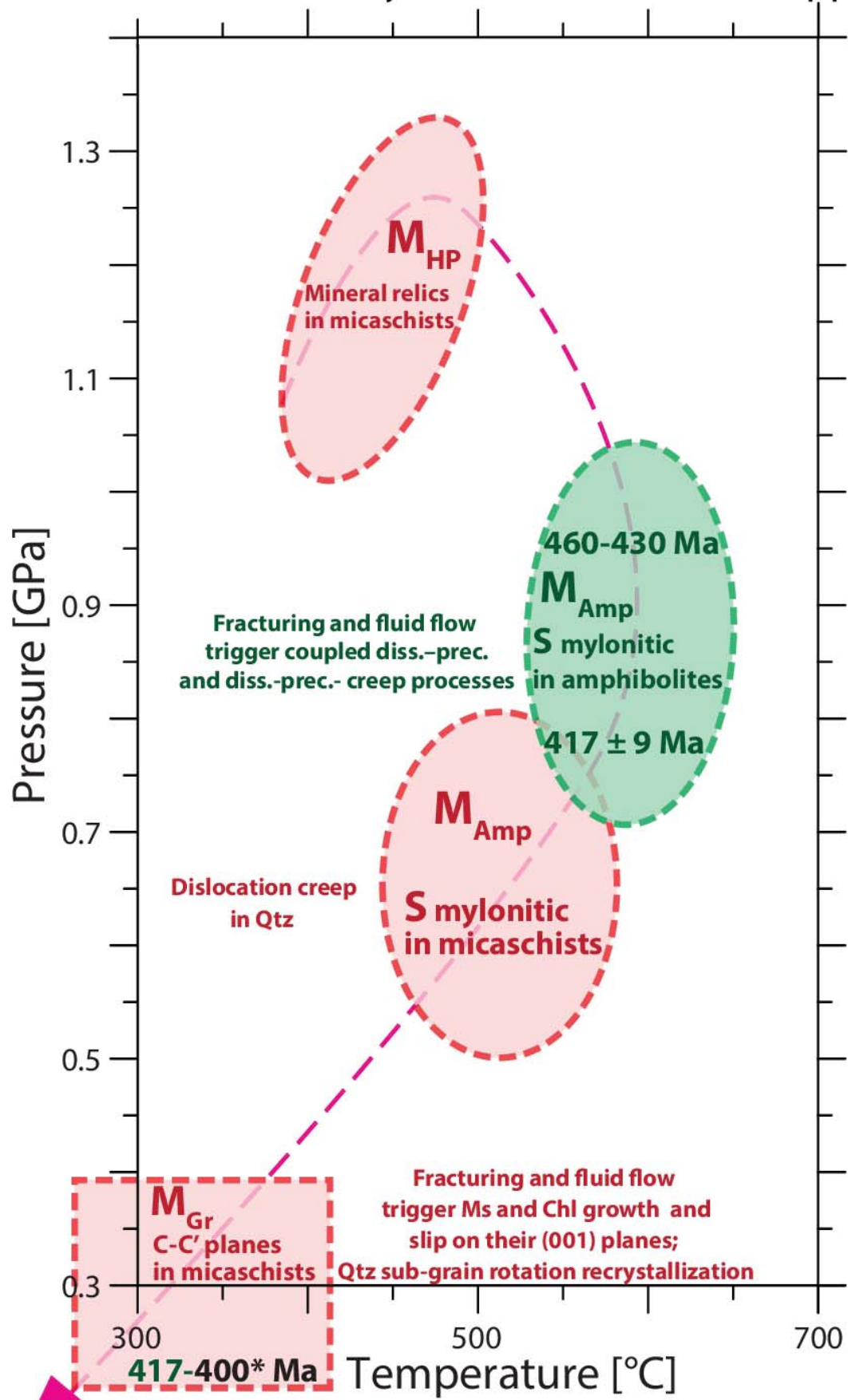


Figure 18.

P-T-t-d summary for the Lower Seve Nappe



P-T constraint in micaschists

P-T constraint in amphibolites

417 Ages of titanite grains in the amphibolites

Inferred P-T path for the Lower Seve Nappe